RAMAN SPECTROSCOPY DETECTION OF MOLECULAR CHANGES ASSOCIATED WITH OSTEOARTHRITIS

by

Karen A. Esmonde-White

A dissertation submitted in partial fulfillment
of the requirements for the degree of
Doctor of Philosophy
(Biomedical Engineering)
in The University of Michigan
2009

Doctoral Committee:
  Professor Michael D. Morris, Chair
  Professor David H. Kohn
  Associate Professor Krishnakumar R. Garikipati
  Associate Professor Blake J. Roessler
  Associate Professor Jan P. Stegemann

Dedication

This thesis is dedicated to my husband Francis for his enthusiasm, technical prowess and boundless emotional support. To my parents Len and Colleen, sister Micki and niece Karen, for their inspiration and encouragement. To my friends Tina and Dan Morris, thank you for your laughter and patience.

“But we go on about
To our jobs and our life
And learn something new
Which helps avoid all the strife”
-Dan Morris

Acknowledgements

The research presented in this thesis was the fruit of working with many talented scientists. It is with great humility and gratitude that I acknowledge the kindness and generosity of so many people who have helped me during my graduate studies. First and foremost, I would like to thank my advisor Michael Morris. Without his encouragement and excellent mentorship, I would not have been able to traverse the long and arduous path of a non-traditional graduate program. His enthusiasm and creativity is matched by his vast scientific knowledge and uncanny ability to find meaning in even the worst-looking data. I have enjoyed each day as his student and will miss his daily visits to the lab where we have discussed everything from fish longevity to politics to microfluidics. And I will carry with me the most important reason for doing science: “because it’s fun”.

I would like to thank my committee members for their suggestions and advice. I appreciate your contributions and the unique perspective that each of you have brought to bear on my research.

Thank you to my lab mates in the Morris group, past and present. I have so many fun memories and have grown as a scientist. I remember my first month in the Morris lab, where Ken Christensen taught me the first rule of optics: “Straight lines are good”. That the same mix of fun and serious work has not changed during my time in the Morris group! I have been truly blessed to have worked with so many gifted scientists and engineers. I would especially like to thank Pat Walker and Nicole Crane with whom I worked on projects, Gurjit Mandair who can run 13.1 miles and still have the energy to talk about research, Angela Carden who continues to find value in using a semicolon,

Jacque Cole for being such a good role model, and Jeremy Shaver for his awesome ability to manipulate matrices.

I would also like to thank members of the Roessler group, Dr. Abigail Smukler and Dr. Farhang Raaii, for their collaboration on many of my projects and useful discussions. I would also like to thank Ken Nicholson, Dan Tobin and Lisa Ponton for their friendship and collaboration. I thank Salwa Poole, Sneha Patel and Heather Workman for encouraging me to continue my studies and making working at Pfizer so fulfilling and fun.

I gratefully acknowledge funding from the National Institutes of Health in the form of a two year training grant and Rackham Graduate School for travel funding assistance.

Table of Contents

List of Figures

List of Tables

Abstract

Vibrational spectroscopic methods are minimally invasive, and are appropriate for use in clinical contexts. Methods were developed in this dissertation for evaluating joint damage and disease using Raman spectroscopy. Subtle changes in the molecular structure of joint tissue and synovial fluid precede morphological changes in the joint. The goal of this research is to develop Raman spectroscopic methods for the examination of joint tissue and biological fluids, for monitoring and detecting molecular alterations associated with osteoarthritis. We identified Raman spectroscopic markers of altered molecular structure in subchondral bone and relevant biological fluids. Using Raman spectroscopy the molecular structure of joint tissues was measured, and the results were compared to the results from micro-computed tomographic and histopathologic analysis. Raman spectra of subchondral bone collected from Del1 (+/-) transgenic mice, a mouse model for early-onset osteoarthritis, indicated lower bone mineralization in transgenic mice (5.73 ± 0.28 vs. 6.87 ± 0.225 in wild-type mice, p=0.003). A fiber-optic Raman probe for arthroscopic measurements was developed to demonstrate the feasibility of measuring the molecular structure of joint tissue with clinically-relevant instrumentation. The carbonate-to-phosphate ratio, a Raman spectroscopic measurement of bone mineral composition, was measured from subchondral bone under an intact layer of cartilage. Our initial work on a human proximal radius specimen indicated that an arthroscope configuration is capable of providing similar carbonate-to-phosphate values as spectra collected on a Raman microscope (0.25 vs. 0.24). In addition to cartilage and subchondral bone, the chemical structure of synovial fluid molecules is a key factor in maintaining healthy joint function. Synovial fluid from normal and diseased joints was examined using a novel drop deposition/Raman spectroscopic method. Raman spectra of synovial fluid from patients with radiographic evidence of osteoarthritis showed evidence of altered protein structure, as shown by increased Raman band intensity ratios at 1080 cm^{-1}/1002 cm^{-1} (0.054 ± 0.07

vs. 0.038 ± 0.003, $p<0.01$) and 1670 cm^{-1}/1655 cm^{-1} (0.68 ± 0.06 vs. 0.51 ± 0.05, $p<0.01$). These studies show that Raman spectroscopic measurements of joint tissue and synovial fluid correlate with established techniques for osteoarthritis detection and Raman spectroscopy may potentially provide early detection of joint damage.

Chapter 1

Introduction

Overview of Thesis Research

The goal of this thesis research is to examine the chemical composition and molecular structure of various components in joint tissues and synovial fluid. Early-stage osteoarthritis is characterized by chemical structure changes to extracellular matrix macromolecules, many of which have not been reliably measured by current histology, imaging or clinical methods. These subtle, inherent changes that occur in joint tissues and/or synovial fluid will provide the markers for diagnosis of knee joint damage. We propose to develop Raman spectroscopy techniques to examine molecular structure and chemical composition of cartilage, subchondral bone or relevant biological fluids. We further propose that Raman spectroscopy will complement current strategies to repair cartilage or subchondral bone by providing insight into the chemistry of joint degeneration.

Chapter 2 provides an overview of the analytical techniques, instrumentation, and data processing techniques used. Chapters 3 and 4 present two studies of Raman spectroscopic examination of tissue specimens from Del1 (+/-) transgenic mice. Eye tissue and femora obtained from wild-type and Del1 (+/-) transgenic mice provided an opportunity to evaluate the ability of Raman spectroscopy to identify chemical structure differences from natural aging and defective type II collagen formation. Type II collagen is a major component of articular cartilage and the vitreous humor of the eye. Known mutations of the type II collagen gene, COL2A1, in humans causes disorders that affect both the eye and skeletal systems.[1-3] Del1 (+/-) mice have defective type II collagen formation. These transgenic mice exhibit altered skeletal development and are a model of early-onset osteoarthritis. Additionally, the Del1 (+/-) mouse can be used to systematically examine the ultrastructure in ocular tissue because of the role of type II collagen in the development of eye tissue and the limited availability of eye tissue from human patients of arthro-ophthalmopathies.[4] Because abnormal type II collagen is also expressed in vitreous, cornea and sclera of Del1 (+/-) mice they exhibit ocular damage including early-onset liquefaction of the vitreous humor and reduction in vitreous fibrils.

Chapter 5 discusses development of an arthroscope coupled with Raman spectroscopy Fiber optic arthroscopy is a technique used by clinicians to visualize areas of eroded cartilage, remove loose cartilage fragments or repair ligament injury. Identification of damaged cartilage during arthroscopy is reliant upon application of visual grading scales that have limited sensitivity and specificity. However, vibrational spectroscopy studies of cartilage surfaces have shown that alterations to cartilage extracellular matrix molecules occur before damage is visually apparent. Instrument response, accuracy and efficiency were tested using cadaveric specimens obtained from the University of Michigan anatomical donations program.

Chapter 6 presents a study of the fluid dynamics of biofluid drop deposition. We explored the effects of fluid viscosity and substrate surface chemistry on drop deposition of plasma and synovial fluid. Simple physical measurements, such as contact angle and viscosity, incorporated into a drop deposition study can aid in interpreting the dried drop and provide insight into the complex drop deposition process. Raman spectra collected from dried plasma drops suggest that the chemistry of the protein-rich outer edge in the dried drop was consistent when dried on different substrates. We concluded that the choice of substrate affects the final deposition pattern and the efficiency of the coarse separation. Dilution had a moderate effect on the optical properties and residual free water in the dried drop. However, Raman markers of protein secondary structure remain unaffected during the evaporation process.

Chapter 7 introduces drop deposition coupled with Raman spectroscopy for characterizing synovial fluid and spectroscopic identification of osteoarthritis biomarkers. For many years, viscosity has been the primary method used by researchers in rheumatology to assess the physiochemical properties of synovial fluid in both normal and osteoarthritic patients. However, progress has been limited by the lack of methods that provide multiple layers of information, use small sample volumes, and are rapid. In this study, Raman spectroscopy was used to assess the biochemical composition of synovial fluid collected from forty patients with clinical evidence of knee osteoarthritis at the time of elective surgical treatment. Severity of knee osteoarthritis was assessed by a radiologist using Kellgren/Lawrence (K/L) scores from knee joint x-rays, while light microscopy and Raman spectroscopy were used to examine synovial fluid aspirates (2-10 μL), deposited on fused silica slides. We showed that Raman bands used to describe protein secondary structure and content can be used to detect changes in synovial fluid from osteoarthritic patients. Several Raman band intensity ratios increased significantly in spectra collected from synovial fluid in patients with radiological evidence of moderate-to-severe osteoarthritis damage. These ratios can be used to provide a “yes/no” damage assessment. These studies provide evidence that Raman spectroscopy would be a suitable candidate in the evaluation of joint damage in knee osteoarthritis patients.

Chapter 8 presents research into developing surface-enhanced Raman spectroscopy (SERS) for *in-vitro* osteoarthritis (OA) biomarker detection. Hyaluronic acid (HA) is a potential OA biomarker and synovial fluid levels of HA have been correlated with progression of joint space narrowing. However, current immunoassay and chromatographic methods used to identify HA in synovial fluid specimens are cumbersome and often require sophisticated instrumentation. Raman spectroscopy may be an alternative to these analytical methods, providing rapid identification of HA using characteristic Raman biomarker bands. Yet, previous reports of normal (unenhanced) Raman spectroscopy for HA are in aqueous solutions exceed 1000X *in-vivo* concentrations because HA is a weakly scattering polysaccharide. In contrast, SERS could improve the detection limits of HA to below the clinical range and we present, to our best knowledge, the first surface-enhanced Raman spectra of HA. The recent commercial availability of gold-coated SERS substrates has enabled rapid the SERS detection of this biomarker at physiological concentrations. Preliminary results showed that HA was observed at low concentrations in aqueous solutions and in synthetic models of biofluids, such as artificial synovial fluid, that contain HA at low concentrations. Complex biofluids, such as synovial fluid or serum, often contain proteins that will compete with HA for the SERS-active sites, and the resulting spectra are dominated by protein Raman bands. To overcome this problem, we used a simple and validated protein precipitation protocol to artificial synovial fluid prior to deposition onto the SERS substrate.

Chapter 9 presents our study of the effects of solution properties on hyaluronic acid drop deposition were also explored. Nanoliter volumes of HA solutions were dried onto a patterned SERS substrate and spectra were collected from the dried hyaluronic acid drops with a near-infrared Raman microscope. Viscosity measurements were incorporated into models of drop deposition of suspended particles to account for the effect of inter-chain attraction on drop formation. Entanglement behavior was described using scaling theory principles. Microscope images were used to evaluate shape of the dried drop. Relative drop thickness was estimated from concentric rings found at drop edges using established models of light interference by thin films. Characteristic hyaluronic acid SERS bands were examined. We found SERS spectra were sensitive not only to polymer conformation, but also to type of deposition (ring versus uniform), and the thickness of the resulting deposition. These data suggest an approach to elucidate the effects of biopolymers on SERS analysis.

Conclusions and future directions are discussed in Chapter 10.

Joint Composition, Chemical Structure and Function

The knee joint is a complex biological system comprised of non-mineralized cartilage, mineralized cartilage, bone, synovial fluid and a synovial membrane (also known as synovium). A schematic of knee joint anatomy is shown in Figure 1.1. Within the synovium, cartilage is attached to the joint surface of the patella, femur and tibia, and the cavity between and around the joint is filled with synovial fluid.[5] Synovium encapsulates the joint. Additional fibrous and ligament layers outside the synovium further contain the entire joint and help to stabilize the joint during motion. The knee joint is avascular and delivery of nutrients is controlled by diffusion through the synovium. Intricate biological, chemical and mechanical properties of cartilage, synovial fluid and subchondral bone within the knee joint underscore its complexity in health and disease.

Cartilage is a connective tissue located throughout the body and varies in physiological function, chemical composition and mechanical properties. There are three types of cartilage: hyaline, elastic and fibrocartilage. Hyaline cartilage is the focus of many studies because it is the cartilage type that covers the ends of bones at joints (as articular cartilage), and comprises epiphyseal plates where bones grow.[6] Articular cartilage provides a lubricated surface for joint movement and resists compressive forces. Chondrocytes, the cells which are responsible for the maintenance and repair of cartilage, are primarily found in the superficial layer near the articular surface and are surrounded by an extracellular matrix consisting primarily of water, type II collagen, proteoglycans, and glycoproteins, Water is a major component in cartilage, comprising between 60-80% of its total weight.

The extracellular matrix of cartilage regulates nutrient diffusion, provides resistance to compressive forces, and adds tensile strength to cartilage. Type II collagen, glycoproteins, and proteoglycans intertwine to form the extracellular matrix. Articular cartilage is heterogeneous in the axial direction in both the relative abundance of chondrocytes and type II collagen orientation. A cross-sectional view of articular cartilage is shown in Figure 1.2. The three zones of articular cartilage are defined primarily by type II collagen orientation. The superficial zone, located at the articular surface, contains the highest density of chondrocytes in cartilage tissue and type II collagen fibers are oriented parallel to the joint surface. In the tangential, or mid, zone collagen fibers are not preferentially oriented. Type II collagen is ubiquitous in the deep zone and is oriented perpendicular to the cartilage surface.

Glycoproteins bound to type II collagen provide structural integrity and influence type II collagen fibrillogenesis.[7] Proteoglycans consist of a hyaluronic acid backbone with core protein side chains. Sulfated glycosaminoglycans, chondroitin sulfate and keratin sulfate, are attached to the core protein. At physiological pH glycosaminoglycans are negatively charged and are highly hydrated. The unique viscoelastic properties of glycosaminoglycans, in addition to the high degree of hydration, renders to proteoglycans a sponge-like quality that provides compression resistance properties to cartilage. Aggrecan is the most abundant proteoglycan in cartilage.

Articular cartilage is unmineralized in the surface layers, but contains a layer of calcified tissue adjacent to subchondral bone. Calcified cartilage intertwines with subchondral bone to form a mineralized plate beneath cartilage and serves as the source of cartilage attachment to bone. Calcified cartilage provides additional structural integrity to the joint and limits diffusion across the bone/cartilage interface. The organic matrix of calcified cartilage is similar to non-mineralized cartilage and the mineral composition of the calcified layer closely resembles hydroxyapatite. The chemical composition of calcified cartilage resembles both cartilage and bone. Because the mineral in calcified cartilage is similar to the carbonated apatite in bone, it exhibits unique mechanical properties.[8, 9] The cortical bone that directly underlies cartilage is called subchondral bone and it is composed primarily of type I collagen and a carbonated apatite mineral.

Synovial fluid, a dialysate of plasma, fills the joint cavity space in diarthrodial joints and is essential to maintaining joint health and function. Synovial fluid is primarily composed of water, proteins, glycosaminoglycans, lipids, small inorganic salts, and metabolites such as amino acids or sugars. Synovial fluid functions include resistance to compression, nutrient diffusion, molecular signaling, and lubrication of cartilage surfaces.[10, 11] Synovial fluid molecules often have multiple functions and exhibit a large degree of interaction with other synovial fluid and cartilage molecules. For example, hyaluronic acid is responsible for the complex viscoelastic properties of synovial fluid but has also recently been found to regulate the biological activity of advanced glycation endproducts and cytokines and enzymes associated with late-stage osteoarthritis.[12-14]

Knee Osteoarthritis

Arthritis is a disease that is marked by the degradation of components in the synovial joint leading to an increase in fluid shear and hydrostatic pressure between two adjacent bones. The main form of arthritis, osteoarthritis (OA), is a degenerative joint disease that is prevalent (rate >30%) among Americans over 65.[15] Primary osteoarthritis occurs without an obvious cause or because of the accumulation of mechanical damage that accompanies aging. Secondary OA occurs as a response to trauma, previous injury, obesity, or metabolic disease. The percentage of adults afflicted with OA increases with age, and causes an important economic burden in lost wages and early retirement.[16] Because of its prevalence in an aging society, OA is one of the most common causes of disability in the elderly.[17] To date, there are no treatments to reverse the cartilage damage characterized by osteoarthritis or induce cartilage regeneration. Identification of osteoarthritis in its early stages is critical to disease management because minimally invasive therapies such as diet, exercise, non-steroidal anti-inflammatory medicines, or intra-articular injections can be effective in delaying disease progression and ameliorating pain. However, by the time patients present with symptoms or when radiographs are able to diagnose OA reliably, then OA is typically in an advanced stage. More challenging to physicians is to estimate OA progression, especially for sub-clinical patients.

The pathogenesis of osteoarthritis (OA) is exceedingly complex, involving genetic and environmental factors as well as local biomechanical factors. Osteoarthritis was historically defined pathologically as focal and progressive loss of hyaline cartilage with concomitant changes in underlying bone. More recent studies have shown that osteoarthritis may be considered a whole joint disease. Biological, chemical and viscoelastic changes affect cartilage, synovium, subchondral bone, synovial fluid, and surrounding muscles and ligaments.[18-21] Degradation of extracellular matrix molecules, such as cleavage of glycosaminoglycans or a loss of collagen cross-linking, is implicated in a complex series of biological, mechanical and chemical events that lead to loss of articular cartilage function. At the level of the articular chondrocyte, an altered composition of matrix, a pathological response to mechanical stress and programmed cell death contribute to the pathologic syndrome, with alterations in cartilage extracellular matrix proteins likely occurring early.

The role of subchondral bone has been examined in current models of osteoarthritis because a common indication of osteoarthritis is thickening of the subchondral bone plate, increased bone mineral density and increased bone stiffness.[22-24] Also, there is a positive correlation between mineral deposits in synovial fluid with advanced stage osteoarthritis. Radiography and other imaging studies have shown alterations in bone architecture and chemistry in addition to plate thickening. [20, 21, 25-28] Material properties in subchondral bone are also compromised, as observed by a less mineralized tissue and altered architecture in the cancellous and cortical bone regions.[23, 29] These studies support the idea that osteoarthritis is a disease that affects the entire joint. Moreover, studies have not been able to show if subchondral bone damage is arthritogenic in nature.

Clinical symptoms, such as pain, swelling or loss of function, are observed in most patients with osteoarthritis. However, these symptoms vary across patient populations, do not adequately correlate with disease stage and are non-specific to osteoarthritis. In 2004, Webb and colleagues reported the results of a population-based cross-sectional survey of knee pain [30]. The survey population included approximately 4,500 people living in the urban area of Manchester, England, divided into eight groups defined by age and gender. Symptomatically, OA is defined as pain with joint use, however, the cause of joint pain in OA has yet to be elucidated.

Assessment of Knee Joint Damage

Identifying osteoarthritis damage, either through clinical observation or laboratory measurements, remains a challenge because of the complex nature of the disease. There is a large body of research in not only identifying suitable biomarkers, but also in developing corresponding analytical methodologies. A variety of clinical imaging, histology, biochemical assay, and analytical chemistry tools have been proposed for diagnosing osteoarthritis. We focus on non-invasive and minimally invasive measurements of joint morphology and synovial fluid biomarkers.

Joint Morphology Measurements

Clinical assessment of osteoarthritis is typically made from a combination of laboratory tests and a patient history for osteoarthritis symptoms such as pain, swelling, stiffness, or loss of function. The gold standard in osteoarthritis laboratory tests is to collect an examination of an x-ray of the affected joint for morphological features that indicate osteoarthritis. The most commonly-used grading system of x-ray features is based on the work of Kellgren and Lawrence.[31, 32] Table 1.1 shows the Kellgren/Lawrence (K/L) grade system for interpreting radiological images of joints. A diagnosis is made based on features in the radiograph, such as osteophytes, narrowing of joint space, and subchondral bone sclerosis. X-ray images representative of K/L scores 1-4 are shown in Figure 1.3. Patients with K/L grades 0-1 are typically considered negative for radiological evidence of osteoarthritis. Patients with K/L grades 2-4 are considered positive for radiological evidence of osteoarthritis. Other imaging modalities, such as magnetic resonance imaging (MRI), are sensitive to morphological alterations in cartilage and may be a promising technique for non-invasive joint tissue imaging of early-stage osteoarthritis damage.[33-35] Ultrasound and computer tomography imaging are also promising techniques for non-invasive visualization of cartilage damage.[36]

Synovial Fluid Biomarkers

Current literature in the field of osteoarthritis biomarkers has largely focused on studying synovial fluid because it is the primary location for secretion of chemical markers related to cartilage damage.[37-44] One approach is to examine the entire chemical profile of synovial fluid. Proteomic analysis, using 2-D electrophoresis or mass spectrometry, has been demonstrated for synovial fluid.[45] A recent SF proteomic analysis found changes in abundant proteins in synovial fluid from arthritic joints, but these changes in protein profile were not dependent on the stage of OA.[46]

Another approach is to examine biomarkers, expressed in the synovial fluid, cartilage matrix, or surrounding bone.[38] However, there is no clear consensus on suitable biomarkers to estimate OA progression or a standardized method to examine synovial fluid. Several bone and cartilage biomarkers only correlate strongly with severe degradation (Outerbridge classification 4 or Noyes classification 0-20%).[47] Other markers, such as proteoglycan fragments, white blood cells, calcium phosphate crystals and collagen fibrils, are correlated with disease progression.[37, 39, 42] Recent studies of cartilage oligomeric matrix protein (COMP) levels in synovial fluid are promising.[48] Arthritic SF may contain higher levels of cartilage fragments, low molecular weight hyaluronic acid molecules, and basic calcium phosphate crystals.[47, 49, 50]

The most prevalent glycosaminoglycan, hyaluronic acid (also called hyaluronan), has been shown to be a critical macromolecule in both healthy and pathological joints, and is currently used to treat pain associated with osteoarthritis. As the primary molecule in intra-articular viscoelastic supplements, hyaluronic acid has been shown to alleviate pain associated with osteoarthritis and may also reduce cartilage damage.[51-53] The secretion of glycosaminoglycans into serum as a response to cartilage damage is an active field of research and the detection of glycosaminoglycan molecules in both serum and synovial fluid has potential to serve as a marker for osteoarthritis diagnosis. Serum levels of hyaluronic acid (HA) have been shown to be a predictor of a positive osteoarthritis diagnosis within 2 years.[54]

Vibrational Spectroscopy of Joint Tissues

The addition of vibrational spectroscopy as a method for analyzing bone tissue has been instrumental in advancing the understanding of bone structure/function relations.[55] Infrared or Raman spectra can reflect perturbations to bone tissue that result from chemical damage, mechanical stress, or genetic defects. The high spatial resolution (1-20 μm) of infrared and Raman spectroscopies facilitates the collection of information on chemical processes, such as re-mineralization of bone or collagen matrix degeneration that would otherwise go unnoticed if using other spectroscopic and biochemical analyses. Vibrational spectroscopy, Fourier-transform infrared (FT-IR) and Raman, are used to complement current histological and biochemical methods of bone (and, by extension, cartilage) analysis. Vibrational spectroscopy and imaging for the analysis of bone serves as a basis for analysis of cartilage. As indicated by increasing number of reports in literature since 2000, using FT-IR and Raman to study articular cartilage is an exciting and valuable field of research, and either method has potential as a diagnostic tool. Raman and FT-IR studies to characterize components such as collagen or hyaluronic acid provide a framework for assessing pathological changes in articular cartilage or the surrounding synovial fluid. Vibrational spectra of cartilage, subchondral bone, extracellular matrix molecules, and cartilage matrix vesicles provided detailed chemical composition which can be used to complement histological or optical microscopy findings. Raman spectroscopy has been used to examine subchondral bone and monitor mineralization of cartilage in-vitro, but has not yet been used to examine articular cartilage. FT-IR images and spectra of damaged cartilage correlated to standard histological measures of cartilage tissue quality.

To date, infrared spectroscopy (commonly used in the Fourier-transform mode) has been the predominant vibrational spectroscopy method for studying cartilage.[56-59] FT-IR has proven useful in applications ranging from tissue engineering to articular cartilage damage assessment. Detailed analysis of collagen and proteoglycan content in bovine cartilage using a variety of FT-IR microscopy and imaging techniques indicate that FT-IR is a feasible method for *in-vivo* identification of cartilage components and collagen fiber orientation. Yet, there is a major impediment to using FT-IR. FT-IR spectra are obscured by water, cartilage specimens need to be dehydrated prior to examination by FT-IR or the FT-IR probe needs to directly contact the tissue of analysis. Due to the high water content (60-80% of the total weight of cartilage), spectroscopic methods that require specimen dehydration and/or direct contact of the probe alters the chemical structure of cartilage or cause artifacts to arise in the spectra.

Raman spectra provide similar information as FT-IR spectra, but Raman spectroscopy may be better suited to tissue spectroscopy. Raman spectra are not obscured by water and measurement does not require direct contact with tissue. The visible or near-infrared optics that are used by Raman instruments are compatible with fiber-optic probes used in clinical instruments such as arthroscopes. A Raman spectroscopic probe for alterations in protein structure is especially useful to distinguish normal and pathological tissues since subtle molecular changes often cause detectable vibrational changes. Properties of Raman that make it an attractive method for direct analysis of biological tissues include high spatial resolution (0.25-0.5 μm for a 532 nm system, 0.5 -1.0 μm for a 785 nm system) and limited spectral interference from water. Because of these advantages, the use of Raman for tissue analysis has been widely reported.[60, 61] Yet examination of cartilage by Raman has not been widely published, possibly due to the focus throughout both the FT-IR and Raman communities on identifying cancerous cells and quantifying glucose. Cartilage Raman spectra have an inherently low signal and require either long integration times or high laser power to obtain spectra that can be used as a diagnostic. Historically, these requirements may have restricted Raman spectroscopy from rapidly studying cartilage *in-situ* because it does not contain a strongly scattering mineral moiety, such as hydroxyapatite, that is ubiquitous throughout hard tissues.

Cartilage Extracellular Matrix Molecules

Early vibrational spectroscopy studies of cartilage extracellular matrix molecules focused on assigning bands and determining factors that affect secondary structure. These early studies provided a foundation for studying cartilage tissue. Glycosaminoglycans, sodium hyaluronate, chondroitin 6-sulfate, and chondroitin 4-sulfate, have been studied using infrared and Raman spectroscopy.[62-67] Table 1.2 shows Raman band assignments for type II collagen and glycosaminoglycans hyaluronic acid and chondroitin-6-sulfate based on our Raman spectra of these molecules and literature reports.[62-64, 68, 69] Polarized infrared spectroscopy was used to characterize dichroic properties of hyaluronic acid functional groups and assign bands using deuterium exchange. [65, 66, 70] Hydration properties of hyaluronic acid and chondroitin sulfate, were studied by infrared spectroscopy. [71-74] Enzymatically-digested hyaluronic acid was examined by nuclear magnetic resonance, infrared, Raman, and visible spectroscopy.[75] Examination of proteoglycans and glycosaminoglycans extracted from cartilage in a case of Langer-Saldino achondrogenesis by infrared spectroscopy revealed low sulfation of proteoglycan and reduced chondroitin 4-sulfate relative to chondroitin 6-sulfate.[76] Vibrational spectroscopy methods to examine collagen structure in tissue, identify pathologic tissue, and monitor fiber tension can be applied to either type I or type II collagen. [69, 77-83]

Type I collagen has been studied extensively, and these studies can also be applied to the examination of type II collagen.[68, 84-88]

Normal Unmineralized Cartilage

Although Raman spectroscopy of non-mineralized articular cartilage has not yet been reported, FT-IR spectroscopy of cartilage was first reported in 2001.[89, 90] The first reports discussed the impact of spectral standards on quantitative spectroscopic measurements, and proposed spectroscopic markers useful for identifying cartilage tissue damage. Camacho reported FT-IR microscopy and imaging on bovine articular cartilage using polarized and unpolarized light.[90] FT-IR images showed agreement with histological data for the distribution of type II collagen and aggrecan, which indicate that FT-IR is a feasible method for identification of cartilage components and determining collagen fiber orientation. Full-depth cartilage sections were dehydrated and embedded. 6 μm thick cross-sections were examined for collagen and proteoglycan content using an FT-IR microscope. FT-IR spectra of aggrecan and type II collagen mixtures were used as a reference for relative amounts of proteoglycan and type II collagen. Differences of proteoglycan and type II collagen content in each of the three layers of the cartilage (superficial, middle and deep zones) were reflected in relative intensity variations. Spectral markers for collagen orientation, proteoglycan content and type II collagen content were reported. Polarized images showed varying type II collagen orientation in each layer of cartilage, as expected. Average fiber orientation, observed as changes in the peak area ratio of collagen amide I: amide II peaks, showed that the collagen orientation became more parallel to the adjacent bone surface in zones closer to the bone. These polarized images were especially indicative of collagen orientation in the superficial zone, and collagen defibrillation in the superficial zone may be an early indication of osteoarthritis. As noted by the authors, cartilage tissue was dehydrated prior to examination by FT-IR. Moreover, spectra were not very specific between type I or type II collagen or between different glycosaminoglycans.

Imaging of type II collagen and proteoglycan in cartilage sections using FT-IR microscopy was reported by Potter et al in 2001.[89] FT-IR images normal bovine nasal cartilage, trypsin-treated bovine nasal cartilage and engineered cartilage in a hollow fiber bioreactor (HFBR) were compared to histological staining of cartilage for sulfated glycosaminoglycan content. FT-IR spectra of type II collagen and chondroitin sulfate were used as pure-component references in least-squares estimations of protein and glycosaminoglycan content. Spectral bands of cartilage were assigned to either type II collagen or chondroitin sulfate using difference spectra between normal and trypsin-digested cartilage. This study found the pure-component spectra do not adequately describe cartilage matrix, because interactions between cartilage matrix molecules were not reflected in the pure component spectra. FT-IR images showed spatial heterogeneity in chondroitin sulfate distribution and confirmed the loss of chondroitin sulfate in trypsin-digested cartilage. FT-IR spectra of engineered cartilage showed penetration of type II collagen into the hollow fiber bioreactor. Least-square estimations of chondroitin sulfate and type II collagen content from FT-IR data showed that the collagen content was overestimated but properly estimated chondroitin sulfate content. The authors found that FT-IR protein bands were not specific to type II collagen and may contain contributions from noncollagenous proteins.

Collagen orientation was quantified in histology sections of equine and human articular cartilage by Bi et al using polarized FT-IR imaging spectroscopy (FT-IRIS).[91] Cartilage specimens were collected from: normal equine articular cartilage, repair equine articular cartilage after a microfracture procedure, human articular cartilage from a normal patient and articular cartilage from a late-stage osteoarthritis patient. Polarized FT-IR images were compared to histological damage scoring and polarized light microscopy of cartilage. FT-IRIS spectra of equine tendon were used as a reference for collagen orientation. Intensity changes in the amide I, amide II and amide III envelopes were observed in FT-IRIS spectra collected from tendon using light polarized parallel or perpendicular to collagen fibers. The ratio of amide I/II areas was sensitive to collagen orientation, confirming the previous study by Camacho. FT-IRIS imaging quantified collagen orientation in each cartilage zone using the ratio of amide I/II areas. FT-IRIS images improved visualization of subtle differences in collagen orientation that were not observed using polarized light microscopy. Because collagen defibrillation in the superficial zone often precedes osteoarthritis onset, the studies by Bi and Camacho demonstrated that vibrational spectroscopy is a useful tool for potentially identifying early-stage articular cartilage damage.

Damaged Unmineralized Cartilage

Use of a fiber-optic based probe for examination of cartilage by FT-IR was demonstrated in 2004 by West et al.[92] Spectral results from IFOP were validated against FT-IR microscopy of the cartilage specimens and Collins visual grading of cartilage damage. There were subtle but significant differences in established infrared markers of collagen damage between mildly and severely degraded cartilages. In another study, FT-IRIS was used to measure collagen structure after exposure to high levels of collagenase to verify the IFOP method. Collagenase breaks down type II collagen, and high levels of this enzyme in the synovial fluid were related to cartilage damage.[43] FT-IRIS, with polarized or unpolarized light, was used to examine full-depth sections of bovine articular cartilage.[58] Exposure time of cartilage to collagenase varied to model mild and severe cartilage damage. Staining of collagenase-treated cartilage showed that damage to type II collagen remained in the superficial zone and the stained specimens were used to verify results from FT-IRIS. Polarized FT-IRIS was used to measure collagen orientation using the AmideI/AmideII area ratio. FT-IRIS using unpolarized light was used to measure chemical structure of collagen using the Amide II/1338^{-1} band area ratio and the 1238 cm^{-1}/1227 cm^{-1} band intensity ratio. Models for mild and severe cartilage damage had shown significant differences in collagen damage. Damage was localized to the superficial zone. FT-IRIS showed that type II collagen had lost parallel alignment normal to the cartilage surface, and the collagen helix had lost structural integrity. This study confirmed the utility of FT-IRIS as a method to examine collagen orientation changes in histology samples. A review of FT-IR imaging and spectroscopy of cartilage reiterates the utility of the method for assessing collagen orientation and proteoglycan content in normal and pathological cartilage.[93]

Least-squares estimations of collagen or proteoglycan content did not adequately account for the extensive interaction between cartilage matrix molecules. A chemometric model was developed by Li et al to optimize the spectral region for diagnosis of cartilage damage.[94] Tibia plateau cartilage specimens collected from 61 arthritic human patients and 3 normal human patients were examined with the fiber-optic FT-IR probe. Tibiae were also examined using the Collins scale to visually identify surface damage. Selected cartilage sections were stained for modified Mankin histological scoring of cartilage damage. A 15-factor partial least-square (PLS) model with leave-one-out validation of spectra data was optimized for spectra region and preprocessing steps. The spectral region of 984-1733 cm^{-1}, with a straight-line subtraction preprocessing step, was found to correlate with early stages of cartilage damage. Prediction of cartilage damage based on IFOP spectra was achieved for over 90% of the specimens, and was within ± 0.5 of the actual Collins grade. When IFOP results were compared with Mankin scoring, the PLS model slightly improved.

FT-IR imaging of chondroitin sulfate and type II collagen content in arthritis focal lesions was shown by David-Vaudey et al.[95] Knee and hip cartilage sections from human patients exhibiting severe osteoarthritis, as evidenced by pre-operative Kellgren/Lawrence score, was examined by FT-IR imaging and Mankin histological scoring. FT-IR images were collected in the superficial, intermediate and deep cartilage zones. Distribution of chondroitin sulfate was calculated using the partial least squares and Euclidean distance method also used by Potter et al in their study. [89] FT-IR images revealed heterogeneous chondroitin sulfate distribution not only between cartilage zones but also within the territorial and inter-territorial matrices. FT-IR images suggest a significant decrease in superficial layer chondroitin sulfate content for severely osteoarthritic cartilage, and variability in intermediate zone collagen content. At arthritic focal lesions, there was significantly less chondroitin sulfate. These FT-IR results were well correlated with Mankin scoring.

Collagen-induced arthritis (CIA) is an experimental model of rheumatoid arthritis where an autoimmune response occurs after administering type II collagen to cartilage tissue. Expression of type II collagen antibodies in serum and synovial fluid is common to collagen-induced arthritis and rheumatoid arthritis. Type II collagen antibodies may contribute to RA pathology or may be expressed as a reaction to cartilage degradation. Crombie et al used histology, FT-IR imaging, and immunofluorescence to determine if monoclonal antibodies (mAbs) to type II collagen penetrate into cartilage and are arthritogenic in nature.[96] Cartilage explants were cultured in two separate arthritogenic mAbs or two control mAbs. Thin sections of cartilage were collected after 14 days and examined using FT-IR imaging, immunofluorescence, and histomorphometry. FT-IR cartilage spectra of treated cartilage sections were compared against a composite spectrum of type II collagen, hyaluronan, and proteoglycan. FT-IR images showed significant loss of proteoglycan content and toluidine blue-stained cartilage samples showed a loss of chondrocytes associated with penetration of arthritogenic mAbs into cartilage. FT-IR spectra also showed collagen degradation associated with mAb penetration into cartilage, as indicated by a shift of Amide I band from 1666 cm^{-1} in control mAb samples to ~1639-1655 cm^{-1} in arthritogenic mAb samples. The authors showed that penetration of mAbs into cartilage tissue is associated with loss of proteoglycan content and denaturation of type II collagen observed in a collagenase-induced model of cartilage degradation.[58]

Subchondral Bone and Mineralized Cartilage

Subchondral bone and calcified articular cartilage structure and architecture have been examined using microscopy, staining and mechanical loading models.[8, 20, 22, 24, 29] But these methods do not provide chemical composition information that can be obtained using vibrational spectroscopy. Pathological mineralization of subchondral bone, cartilage matrix vesicles and cartilage has also been examined using Raman and synchrotron infrared spectroscopy. These studies support current research into the role of subchondral bone and pathological mineralization in the development of osteoarthritis.

Infrared microscopy of subchondral bone was first reported in 1998 by Miller et al.[97] Use of a synchrotron light source improved spatial resolution to 5 μm. Chemical composition from sections of cancellous, cortical and subchondral bone harvested from monkey was measured by two spectra collection methods. In one approach, several line scans (also called transects) were collected radially from an osteon. In another approach, five line scans were collected in a single line from the cartilage to cancellous bone. Band area ratios used to describe bone chemistry, such as carbonate to phosphate ratio and mineral to matrix ratio, were applied. Infrared spectra collected closer to an osteon showed a greater protein content reflecting newly formed bone. Spectra collected further from an osteon with an increased mineral content reflected more mature and mineralized bone tissue. The carbonate to phosphate band area ratio increased in thicker subchondral bone, and these results suggest a potential spectroscopic marker of osteoarthritis in subchondral bone.

Altered mineralization in sclerotic bone and osteophytes were found in an osteoarthritic tibia plateau.[98] Specimens were taken from sclerotic areas of subchondral bone, attached osteophyte, detached osteophyte and cancellous bone underlying subchondral bone of an osteoarthritis patient. Specimens from normal cortical and cancellous bone were also collected. FT-IR spectra were collected from KBr pellets of dried and pulverized bone and compared to hydroxyapatite and type I collagen. The mineral to matrix ratio (MTMR) was calculated using the amide I intensity at ~1650 cm^{-1} and hydroxyapatite intensity at ~1030 cm^{-1}. Generally, pathologic bone specimens were less mineralized than normal cortical or cancellous bone. Sclerotic areas were more mineralized than detached or attached osteophytes. The authors proposed two mechanisms to account for the observed differences in mineralization: 1) subchondral bone remineralization was induced by an acidic synovial fluid environment or 2) remineralization as based on deposition of mineral ions by the vascular system. To date, these interesting hypotheses have not yet been confirmed.

Mineralization in cartilage occurs under a variety of biological, chemical and mechanical environments. Mechanisms of pathologic mineral deposits in osteoarthritis matrix vesicles of articular cartilage were examined *in-vitro* using enzyme assays, radiometric assay of ^{45}Ca, FT-IR spectroscopy and polarized light microscopy by Derfus et al.[99] FT-IR spectra identified calcium pyrophosphate dihydrate (CPPD) and apatite mineral crystals that were being produced in osteoarthritis matrix vesicles, which are relevant in osteoarthritis progression.

Heger et al proposed a mechanism that laser-induced mineralization of treated cartilage is responsible for long-term structural stability and the mechanism may be extrapolated to biological mineralization. [100] Intracellular and extracellular laser-induced cartilage mineralization was monitored using Raman spectroscopy of laser reshaped rabbit auricular (ear) cartilage. Calcium sulfate and calcium carbonate crystals were found intracellularly and calcium phosphate crystals were found in extracellular spaces. The authors proposed that, in addition to a stress relaxation of cartilage tissue, laser treatment caused apoptotic cells to release matrix vesicles and the released matrix vesicles mediated mineralization.

Cartilage and Bone Tissue Engineering

Spectroscopy and data handling techniques used to examine cartilage in health or disease can be applied toward engineered bone and cartilage. Boskey and Camacho reviewed FT-IR imaging and microspectroscopy methods used to analyze bone and cartilage.[101] To date, all of the reports to examine tissue engineered cartilage have been using FT-IR. Camacho et al studied genetically modified bovine chondrocytes using FT-IR imaging.[56] Previously identified markers for collagen orientation and proteoglycan content in cartilage were used to examine integration of engineered cartilage-like tissue into defect sites and evaluate the native cartilage's organization. Chondrocytes were treated with an adenovirus vector encoding bone morphogenetic protein-7 (AdBMP-7) to stimulate matrix production. FT-IR images showed an increase in proteoglycan production and a decrease in collagen II output. FT-IR images could distinguish between neo-tissue and host tissue. Results showed an incomplete integration of neo-tissue and could not conclusively indicate an active role of surrounding tissues in neo-tissue integration. Based on FT-IR images, the authors suggested that cell-based repairs could not be achieved by simply placing engineered tissue atop of defective tissue.

FT-IR images to obtain quantitative proteoglycan content of nasal cartilage grown in a hollow fiber bioreactor (HFBR) was shown by Potter et al in 2001.[89] In that study, the authors demonstrated that immature cartilage had grown after a 3 week incubation period, and incorporation of type II collagen into the HFBR. Lower chondroitin sulfate content was found in bioengineered cartilage, relative to native cartilage. In a separate study, FT-IR imaging spectroscopy (FT-IRIS) was used by Kim et al to monitor the growth of articular cartilage in a HFBR. [102] The authors used the integrated area of the amide I envelope (1590-1720 cm^{-1}) to measure type II collagen distribution and conformation and the integrated area of 985-1140 cm^{-1} to measure proteoglycan content of cartilage at the inflow and outflow sections of the HFBR. Results from FT-IRIS showed a significant increase of proteoglycan content at the center area and surface area of inflow tissue. However, FT-IRIS estimation of proteoglycan content was not well-correlated with biochemical assays of sulfated glycosaminoglycans because of the small number of samples.

Synovial Fluid

Near-infrared (NIR) and Fourier-transform infrared spectroscopy have both been used to analyze the chemical composition of SF from osteoarthritis, rheumatoid arthritis, or spondyloarthropathy patients.[103-106] NIR or FTIR spectra of dried SF films allowed automated identification of arthritis with a classification rate greater than 95%. Individual components in SF could not be identified using NIR or FTIR spectra. However, the overall chemical composition did correlate with spectral patterns. These early studies provided evidence that vibrational spectra of SF could be used to discriminate between different types of arthritis.

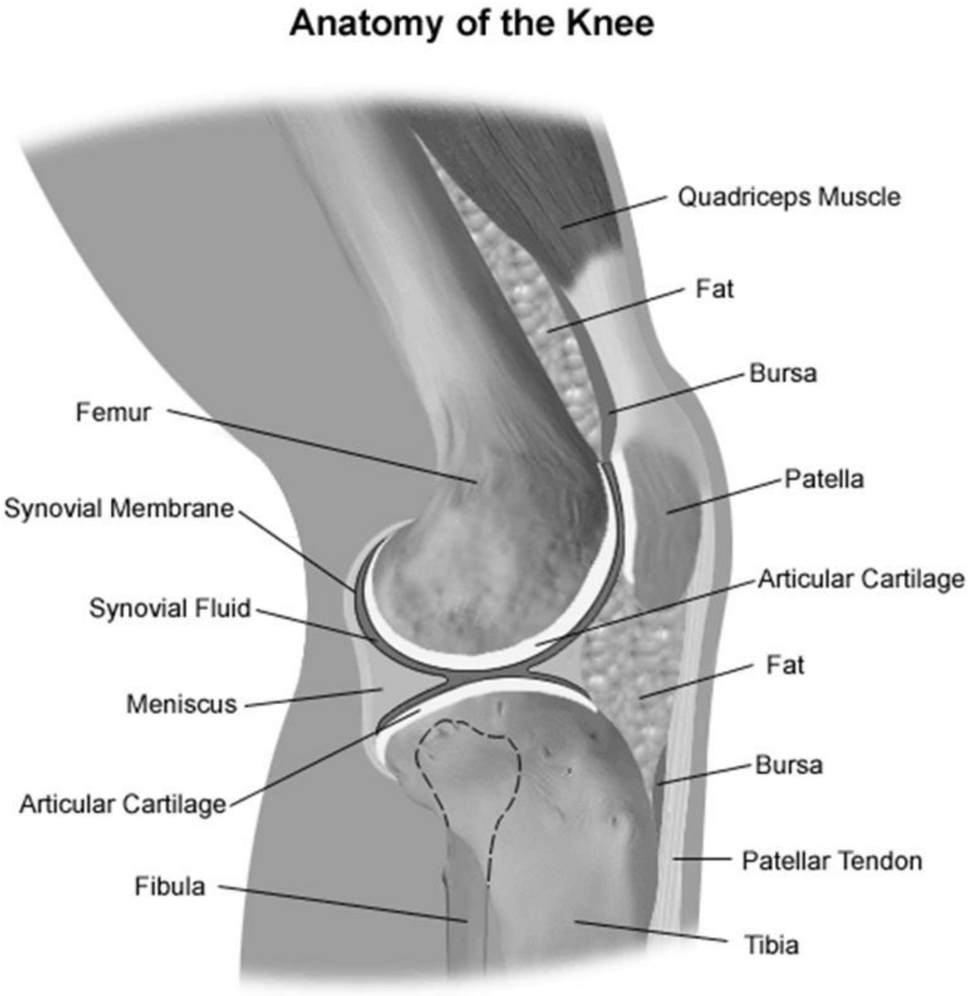

Figure 1.1: Schematic of knee joint

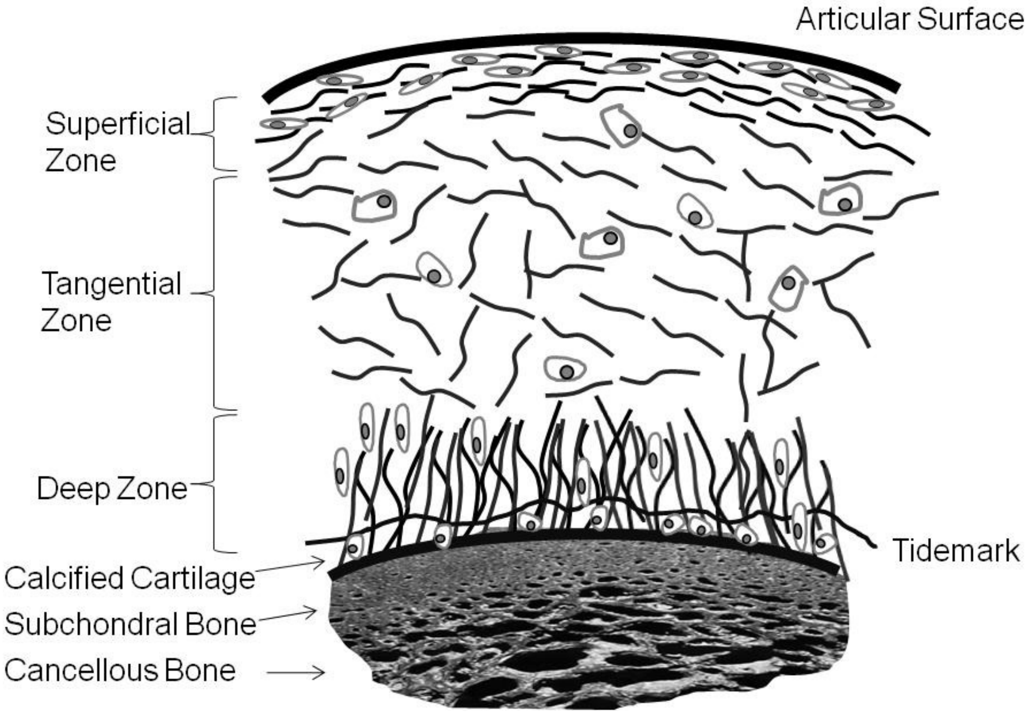

Figure 1.2: Collagen orientation and chondrocytes distribution in cartilage zones

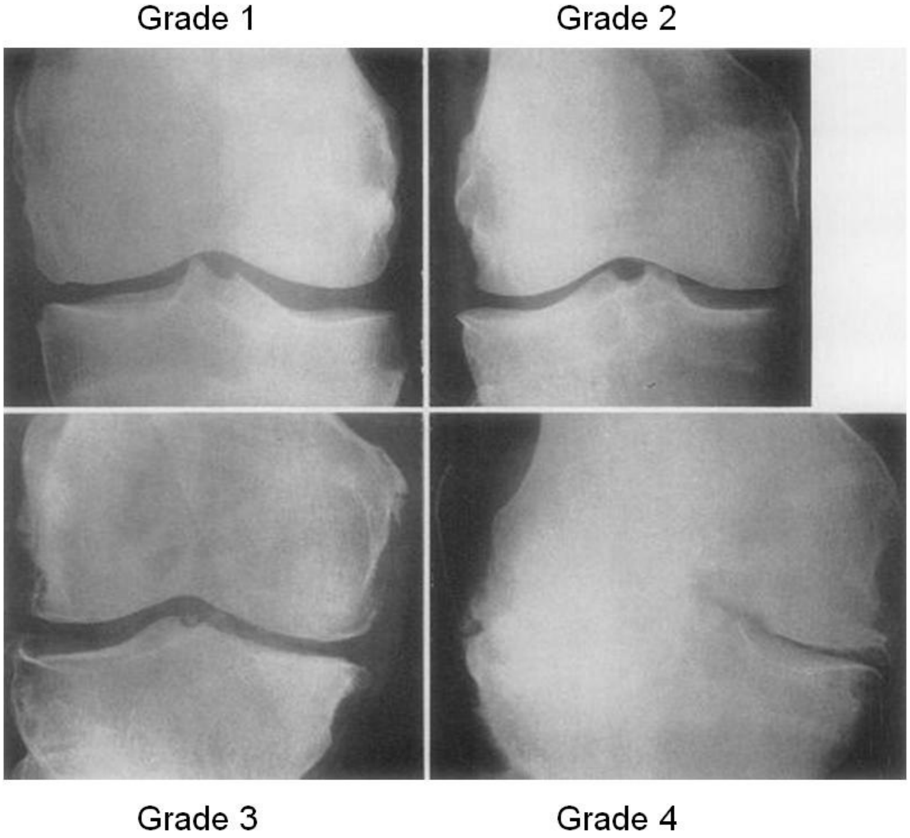

Figure 1.3: X-rays of knees from patients with various Kellgren/Lawrence scores. Reproduced from original article, Ann.Rheum.Dis, 1957, 16(4) 494-502, with permission by the publisher, BMJ Publishing Group Ltd.

Kellgren/Lawrence Grade	Description
Grade 0	Normal, no radiological evidence of osteoarthritis
Grade 1	Doubtful; possible osteophytes and joint space narrowing
Grade 2	Mild; definite osteophytes and joint space narrowing, possible sclerosis
Grade 3	Moderate; slight osteophytes, pronounced joint space narrowing, some sclerosis, and deformation to condyle shape
Grade 4	Severe; joint space is extensively narrowed, sclerosis and cysts, deformed condyle shape, large osteophytes

Table 1.1: Kellgren/Lawrence grading of radiography features in knee joint x-rays

Band Position (cm^{-1})	Assignment	Extracellular Matrix Molecule
850 (s)	Proline	Type II collagen
899 (ms-s)	C_1-H deformation, β-linkage	Glycosaminoglycans
920 (s)	Proline	Type II collagen
937-945 (ms-s)	C-O-C linkage	Glycosaminoglycans
937 (sh)	C-C stretch, α-helix	Type II collagen
995 (s)		Chondroitin-6-sulfate
1002 (s)	Phenylalanine ring breathing	Type II collagen
~1045 (s)	C-O, C-C stretch	Hyaluronic acid
1065 (s)	SO_3^- symmetric stretch	Chondroitin-6-sulfate
~1090 (ms)	C-OH bend, acetyl group	Hyaluronic acid
~1130 (s)	C_4-OH bend and C_4-H bend	Hyaluronic acid
~1150 (sh)	C-O, C-C, oxygen bridge	Hyaluronic acid
1205 (m)	CH_2 twist Hypro, Tyr, Phe	Hyaluronic acid Type II collagen
1220-1280 (ms)	Amide III envelope	Type II collagen
1330-1340 (s)	C-H bend, Amide III	Glycosaminoglycans
1375 (s)	COO^- symmetric stretch CH_3 deformation	Glycosaminoglycans
1410 (m)	COO^- symmetric stretch CH_3 bend	Glycosaminoglycans
1458 (s)	CH_2/CH_3 scissoring	Type II collagen
1458 (w)	CH_2/CH_3 scissoring	Glycosaminoglycans
1640-1700 (ms)	Amide I envelope	Type II collagen

Table 1.2: Raman band assignments for extracellular matrix molecules. Letters next to the band position indicate relative intensity (s=strong, ms=moderately strong, m=moderate, w=weak, sh=shoulder).

References

1. Donoso LA, Edwards AO, Frost AT, Ritter IIIR, Ahmad N, Vrabec T, Rogers J, Meyer D, Parma S: **Clinical Variability of Stickler Syndrome: Role of Exon 2 of the Collagen COL2A1 Gene**. *Survey of Ophthalmology* 2003, **48**(2):191-203.
2. McLeod D, Black GC, Bishop PN: **Vitreous phenotype:genotype correlation in Stickler syndrome**. *Graefe's Archive for Clinical and Experimental Ophthalmology* 2002, **241**(1):63-65.
3. Poulson AV, Hooymans JMM, Richards AJ, Bearcroft P, Murthy R, Baguley DM, Scott JD, Snead MP: **Clinical Features of Type 2 Stickler Syndrome**. *Journal of Medical Genetics* 2004, **41**(8):e107-e113.
4. Ihanamaki T, Salminen H, Saamanen A-M, Sandberg-Lall M, Vuorio E, Pelliniemi LJ: **Ultrastructure characterization of developmental and degenerative vitreo-retinal changes in the eyes of transgenic mice with a deletion mutation in type II collagen gene**. *Current Eye Research* 2002, **24**(6):439-450.
5. Cohen NP, Foster RJ, Mow VC: **Composition and Dynamics of Articular Cartilage: Structure, Function, and Maintaining Heathly State**. *Journal of Orthopaedic and Sports Physical Therapy* 1998, **28**(4):203-212.
6. Marieb EN: **Human Anatomy and Physiology**, 4th edn. Menlo Park, CA: Benjamin/Cummings Science Publishers; 1998.
7. Kucharz EJ: **The Collagens: Biochemistry and Pathophysiology**. Berlin: Springer-Verlag; 1992.
8. Ferguson VL, Bushby AJ, Boyde A: **Nanomechanical properties and mineral concentration in articular calcified cartilage and subchondral bone**. *Journal of Anatomy* 2003, **203**:191-202.
9. Kim HM, Rey C, Glimcher MJ: **X-Ray Diffraction, Electron Microscopy, and Fourier Transform Infrared Spectroscopy of Apatite Crystals Isolated From Chicken and Bovine Calcified Cartilage**. *Calcified Tissue International* 1996, **59**(1):58-63.
10. Fam H, Bryant JT, Kontopoulou M: **Rheological properties of synovial fluids**. *Biorheology* 2007, **44**(2):59-74.
11. Jay GD, Torres JR, Rhee DK, Helminen HJ, Hytinnen MM, Cha C-J, Elsaid K, Kim K-S, Cui Y, Warman ML: **Association between friction and wear in diarthrodial joints lacking lubricin**. *Arthritis & Rheumatism* 2007, **56**(11):3662-3669.
12. Cowman MK, Matsuoka S: **Experimental approaches to hyaluronan structure**. *Carbohydrate Research* 2005, **340**(5):791-809.
13. Neumann A, Schinzel R, Palm D, Riederer P, Münch G: **High molecular weight hyaluronic acid inhibits advanced glycation endproduct-induced NF-kB activation and cytokine expression**. *FEBS Letters* 1999, **453**(3):283-287.
14. Wang CT, Lin YT, Chiang BL, Lin YH, Hou SM: **High molecular weight hyaluronic acid down-regulates the gene expression of osteoarthritis-associated cytokines and enzymes in fibroblast-like synoviocytes from patients with early osteoarthritis**. *Osteoarthritis and Cartilage* 2006, **14**(12):1237-1247.

15. Gabriel SE: **Epidemiology of Osteoarthritis**. In: *Kelley's Textbook of Rheumatology, 6th ed.* Edited by Ruddy S, Harris Jr. ED, Sledge CB, Sergent JS, Budd RC. Philadelphia: W.B. Saunders; 2001: 324-327.
16. Felson DT, Lawrence RC, Dieppe PA, Hirsch R, Helmick CG, Jordan JM, Kington RS, Lane NE, Nevitt MC, Zhang Y *et al*: **Osteoarthritis: new insights. Part 1: the disease and its risk factors**. *Ann Intern Med* 2000, **133**(8):635-646.
17. Guccione AA, Felson DT, Anderson JJ, Anthony JM, Zhang Y, Wilson PW, Kelly-Hayes M, Wolf PA, Kreger BE, Kannel WB: **The effects of specific medical conditions on the functional limitations of elders in the Framingham Study**. *Am J Public Health* 1994, **84**(3):351-358.
18. Felson DT, Neogi T: **Osteoarthritis: Is it a disease of cartilage or of bone?** *Arthritis & Rheumatism* 2004, **50**(2):341-344.
19. Dieppe PA, Lohmander LS: **Pathogenesis and management of pain in osteoarthritis**. *The Lancet* 2005, **365**(9463):965-973.
20. Burr DB, Schaffler MB: **The involvement of subchondral mineralized tissues in osteoarthrosis: Quantitative microscopic evidence**. *Microscopy Research and Technique* 1997, **37**(4):343-357.
21. Oegema TR, Carpenter RJ, Hofmeister F, Thompson RC: **The interaction of the zone of calcified cartilage and subchondral bone in osteoarthritis**. *Microscopy Research and Technique* 1997, **37**(4):324-332.
22. Li B, Aspden RM: **Composition and Mechanical Properties of Cancellous Bone from the Femoral Head of Patients with Osteoporosis or Osteoarthritis**. *Journal of Bone and Mineral Research* 1997, **12**(4):641-651.
23. Li B, Marshall D, Roe M, Aspden RM: **The electron microscope appearance of the subchondral bone plate in the human femoral head in osteoarthritis and osteoporosis**. *Jounal of Anatomy* 1999, **195**:101-110.
24. Day JS, van der Linden JC, Bank RA, Ding M, Hvid I, Sumner DR, Weinans H: **Adaptation of subchondral bone in osteoarthritis**. *Biorheology* 2004, **41**(3-4):359-368.
25. Matsui H, Shimizu M, Tsuji H: **Cartilage and subchondral bone interaction in osteoarthrosis of human knee joint: A histological and histomorphometric study**. *Microscopy Research and Technique* 1997, **37**(4):333-342.
26. Lahm A, Uhl M, Erggelet C, Haberstroh J, Mrosek E: **Articular cartilage degeneration after acute subchondral bone damage: an experimental study in dogs with histopathological grading**. *Acta Orthop Scand* 2004, **75**(6):762-767.
27. Hunter DJ, Hart D, Snieder H, Bettica P, Swaminathan R, Spector TD: **Evidence of altered bone turnover, vitamin D and calcium regulation with knee osteoarthritis in female twins**. *Rheumatology (Oxford)* 2003, **42**(11):1311-1316.
28. Bruyere O, Dardenne C, Lejeune E, Zegels B, Pahaut A, Richy F, Seidel L, Ethgen O, Henrotin Y, Reginster JY: **Subchondral tibial bone mineral density predicts future joint space narrowing at the medial femoro-tibial compartment in patients with knee osteoarthritis**. *Bone* 2003, **32**(5):541-545.

29. Bailey AJ, Mansell JP, Sims TJ, Banse X: **Biochemical and mechanical properties of subchondral bone in osteoarthritis**. *Biorheology* 2004, **41**(3-4):349-358.
30. Webb R, Brammah T, Lunt M, Urwin M, Allison T, Symmons D: **Opportunities for prevention of 'clinically significant' knee pain: results from a population-based cross sectional survey**. *J Public Health (Oxf)* 2004, **26**(3):277-284.
31. Kellgren JH, Lawrence JS: **Radiological Assessment of Osteo-Arthrosis**. *Ann Rheum Dis* 1957, **16**(4):494-502.
32. Kellgren JH, Lawrence JS (eds.): **Atlas of Standard Radiographs**. Oxford, UK: Blackwell Scientific; 1963.
33. Libicher M, Ivancic M, Hoffmann V, Wenz W: **Early changes in experimental osteoarthritis using the Pond-Nuki dog model: technical procedure and initial results of in vivo MRI imaging**. *European Radiology* 2005, **15**:390-394.
34. Burstein D, Gray ML: **Is MRI fulfilling its promise for molecular imaging of cartilage in arthritis?** *Osteoarthritis and Cartilage* 2006, **14**(11):1087-1090.
35. Eckstein F, Cicuttini F, Raynauld JP, Waterton JC, Peterfy C: **Magnetic resonance imaging (MRI) of articular cartilage in knee osteoarthritis (OA): morphological assessment**. *Osteoarthritis and Cartilage* 2006, **14**(Supplement 1):46-75.
36. Moskowitz RW, Altman RD, Hochberg MC, Buckwalter JA, Goldberg VM: **Osteoarthritis: diagnosis and medical/surgical management**, 4 edn. Philadelphia: Wolters Kluwer/Lippincott Williams & Wilkins; 2007.
37. Hegemann N, Kohn B, Brunnberg L, Schmidt MF: **Biomarkers of joint tissue metabolism in canine osteoarthritis and arthritic joint disorders**. *Osteoarthritis and Cartilage* 2002, **10**:714-721.
38. Heinegard D: **Extracellular matrix molecules of cartilage and their use as markers of cartilage alteration in joint disease**. *Zeitschrift fur Rheumatologie* 1998, **57**(3):174.
39. Herrero-Beaumont G, Guerrero R, Sanchez-Pernaute O, Acebes C, Palacios I, Mas S, Rodriguez I, Egido J, Vivanco F: **Cartilage and bone biological markers in the synovial fluid of osteoarthritic patients after hyaluronan injections in the knee**. *Clinica Chimica Acta* 2001, **308**:107-115.
40. Kindt E, Rossi DT, Gueneva-Boucheva K, Hallak H: **Quantitative Method for Biomarkers of Collagen Degradation Using Liquid Chromatography Tandem Mass Spectrometry**. *Analytical Biochemistry* 2000, **283**:71-76.
41. Marini S, Francesco Fasciglione G, Monteleone G, Maiotti M, Tarantino U, Coletta M: **A correlation between knee cartilage degradation observed by arthroscopy and synovial proteinases activities**. *Clinical Biochemistry* 2003, **36**(4):295-304.
42. Nalbant S, Martinez JAM, Kitumnuaypong T, Clayburne G, Sieck M, Schumacher JHR: **Synovial fluid features and their relations to osteoarthritis severity: new findings from sequential studies**. *Osteoarthritis and Cartilage* 2003, **11**(1):50-54.

43. Otterness IG, Bliven ML, Eskra JD, te Koppele JM, Stukenbrok HA, Milici AJ: **Cartilage damage after intraarticular exposure to collagenase 3**. *Osteoarthritis and Cartilage* 2000, **8**(5):366-373.
44. Poortmans JR, S'Jongers J-J, Bidon G: **Distribution of Plasma Proteins and Hyaluronic Acid in Synovial Fluid and Serum of Human Subjects in Hydarthrosis**. *Clinica Chimica Acta* 1974, **55**:205-209.
45. Wilson R, Bateman JF: **Cartilage proteomics: Challenges, solutions and recent advances**. *PROTEOMICS - CLINICAL APPLICATIONS* 2008, **2**(2):251-263.
46. Gobezie R, Kho A, Krastins B, Sarracino DA, Thornhill TS, Chase M, Millett PJ, Lee DM: **High Abundance Synovial Fluid Proteome: Distinct Profiles in Health and Osteoarthritis**. *Arthritis Research and Therapy* 2007, **9**(2):R36.
47. Schmidt-Rohlfing B, Thomsen M, Niedhart C, Wirtz DC, Schneider U: **Correlation of bone and cartilage markers in the synovial fluid with the degree of osteoarthritis**. *Rheumatology International* 2002, **21**:193-199.
48. Williams F, Spector T: **Biomarkers in osteoarthritis**. *Arthritis Research & Therapy* 2008, **10**(1):101.
49. Yavorskyy A, Hernandez-Santana A, McCarthy G, McMahon G: **Detection of calcium phosphate crystals in the joint fluid of patients with osteoarthritis - analytical approaches and challenges**. *The Analyst* 2008, **133**(3):302-318.
50. Praest BM, Greiling H, Kock R: **Assay of synovial fluid parameters: hyaluronan concentration as a potential marker for joint diseases**. *Clinica Chimica Acta* 2003, **266**:117-128.
51. Dausse Y, Grossin L, Miralles G, Pelletier S, Mainard D, Hubert P, Baptiste D, Gillet P, Dellacherie E, Netter P *et al*: **Cartilage repair using new polysaccharidic biomaterials: macroscopic, histological and biochemical approaches in a rat model of cartilage defect**. *Osteoarthritis and Cartilage* 2003, **11**(1):16-28.
52. Goldberg VM, Buckwalter JA: **Hyaluronans in the treatment of osteoarthritis of the knee: evidence for disease-modifying activity**. *Osteoarthritis and Cartilage* 2005, **13**(3):216-224.
53. Pagnano M, Westrich G: **Successful nonoperative management of chronic osteoarthritis pain of the knee: safety and efficacy of retreatment with intra-articular hyaluronans**. *Osteoarthritis and Cartilage* 2005, **13**(9):751-761.
54. Pavelka K, Forejtova S, Olejarova M, Gatterova J, Senolt L, Spacek P, Braun M, Hulejova M, Stovickova J, Pavelkova A: **Hyaluronic acid levels may have predictive value for the progression of knee osteoarthritis**. *Osteoarthritis and Cartilage* 2004, **12**(4):277-283.
55. Carden A, Morris MD: **Application of vibrational spectroscopy to the study of mineralized tissues (review)**. *Journal of Biomedical Optics* 2000, **5**(3):259-268.
56. Camacho NP, West P, Griffith MH, Warren RF, Hidaka C: **FT-IR imaging spectroscopy of genetically modified bovine chondrocytes**. *Materials Science and Engineering* 2001, **C17**:3-9.
57. Camacho NP, West P, Torzilli PA, Mendelsohn R: **FTIR Microscopic Imaging of Collagen and Proteoglycan in Bovine Cartilage**. *Biopolymers* 2001, **62**:1-8.

58. West PA, Torzilli PA, Chen C, Lin P, Camacho NP: **Fourier transform infrared imaging spectroscopy analysis of collagenase induced cartilage degradation**. *Journal of Biomedical Optics* 2005, **10**(1):014015-014011-014016
59. Ramakrishnan N, Xia Y, Bidthanapally A: **Polarized IR microscopic imaging of articular cartilage**. *Physics in Medicine and Biology* 2007, **52**(15):4601-4614.
60. Mahadevan-Jansen A: **Raman Spectroscopy: From Benchtop to Bedside**. In: *Biomedical Photonics Handbook.* Edited by Vo-Dinh T. Boca Raton: CRC Press; 2003.
61. Puppels GJ: **In Vivo Raman Spectroscopy**. In: *Handbook of Raman Spectroscopy: From the Research Laboratory to the Process Line.* Edited by Lewis IR, Edwards HGM. New York: Marcel Dekker; 2001.
62. Bansil R, Yannas IV, Stanley HE: **Raman Spectroscopy: A Structural Review of Glycosaminoglycans**. *Biochimica et Biophysica Acta* 1978, **541**:535-542.
63. Barrett TW, Peticolas WL: **Laser Raman Inelastic Light Scattering Investigations of Hyaluronic Acid Primary and Secondary Structure**. *Journal Of Raman Spectroscopy* 1979, **8**(1):35-38.
64. Cabassi F, Casu B, Perlin AS: **Infrared absorption and Raman scattering of sulfate groups of heparin and related glycosaminoglycans in aqueous solution**. *Carbohydrate Research* 1978, **63**:1-11.
65. Cael JJ, Isaac DH, Blackwell J, Koenig JL, Atkins EDT, Sheehan JK: **Polarized infrared spectra of crystalline glycosaminoglycans**. *Carbohydrate Research* 1976, **50**:169-179.
66. Cael JJ, Koenig JL, Blackwell J: **Infrared and Raman spectroscopy of carbohydrates : Part IV. Identification of configuration- and conformation-sensitive modes for -glucose by normal coordinate analysis**. *Carbohydrate Research* 1974, **32**(1):79-91.
67. Gilli R, Kacurakova M, Mathlouthi M, Navarini L, Paoletti S: **FTIR studies of sodium hyaluronate and its oligomers in the amorphous solid phase and in aqueous solution**. *Carbohydrate Research* 1994, **263**(2):315-326.
68. Frushour BG, Koenig JL: **Raman scattering of collagen, gelatin, and elastin**. *Biopolymers* 1975, **14**(2):379-391.
69. Wang YN, Galiotis C, Bader DL: **Determination of molecular changes in soft tissues under strain using laser Raman microscopy**. *Journal of Biomechanics* 2000, **33**(4):483-486.
70. Quinn FR, Bettelheim FA: **Infrared dichroism of sodium hyaluronate**. *Biochimica et Biophysica Acta* 1963, **69**:544-551.
71. Servaty R, Schiller J, Binder H, Arnold K: **Hydration of polymeric components of cartilage -- an infrared spectroscopic study on hyaluronic acid and chondroitin sulfate**. *International Journal of Biological Macromolecules* 2001, **28**(2):121-127.
72. Haxaire K, Maréchal Y, Milas M, Rinaudo M: **Hydration of polysaccharide hyaluronan observed by IR spectrometry. I. Preliminary experiments and band assignments**. *Biopolymers* 2003, **72**(1):10-20.
73. Haxaire K, Maréchal Y, Milas M, Rinaudo M: **Hydration of hyaluronan polysaccharide observed by IR spectrometry. II. Definition and quantitative**

analysis of elementary hydration spectra and water uptake. *Biopolymers* 2003, **72**(3):149-161.

74. Maréchal Y, Milas M, Rinaudo M: **Hydration of hyaluronan polysaccharide observed by IR spectrometry. III. Structure and mechanism of hydration**. *Biopolymers* 2003, **72**(3):162-173.
75. Alkrad JA, Mrestani Y, Stroehl D, Wartewig S, Neubert R: **Characterization of enzymatically digested hyaluronic acid using NMR, Raman, IR, and UV-Vis spectroscopies**. *Journal of Pharmaceutical and Biomedical Analysis* 2003, **31**:545-550.
76. Feshchenko SP, Rebrin IA, Sokolnik VP, Sher BM, Sokolov BP, Kalinin VN, Lazjuk GI: **The absence of type II collagen and changes in proteoglycan structure of hyaline cartilage in a case of Langer-Saldino achondrogenesis**. *Human Genetics* 1989, **82**(1):49-54.
77. Goheen SC, Lis LJ, Kauffman JW: **Raman Spectroscopy of Intact Feline Corneal Collagen**. *Biochimica et Biophysica Acta* 1978, **536**:197-204.
78. Mizuno A, Tsuji M, Fujii K, Kawauchi K, Ozaki Y: **Near-infrared Fourier transform Raman spectroscopic study of cornea and sclera**. *Japanese Journal of Ophthalmology* 1994, **38**:44-48.
79. Dehring KA, Smukler AR, Roessler BJ, Morris MD: **Correlating Changes in Collagen Secondary Structure with Ageing and Defective Type II Collagen by Raman Spectroscopy**. *Applied Spectroscopy* 2006, **60**(4):366-372.
80. Jackson M, Choo L-P, Watson PH, Halliday WC, Mantsch HH: **Beware of connective tissue proteins: Assignment and implications of collagen absorptions in infrared spectra of human tissues**. *Biochimica et Biophysica Acta (BBA) - Molecular Basis of Disease* 1995, **1270**(1):1-6.
81. Frank CJ, McCreery RL, Redd DCB: **Raman Spectroscopy of Normal and Diseased Human Breast Tissues**. *Anal Chem* 1995, **67**(5):777-783.
82. Koljenovic S, Schut TCB, van Meerbeeck JP, Maat APWM, Burgers SA, Zondervan PE, Kros JM, Puppels GJ: **Raman microspectroscopic mapping studies of human bronchial tissue**. *Journal of Biomedical Optics* 2004, **9**(6):1187-1197.
83. Krafft C, Sobottka SB, Schackert G, Salzer R: **Raman and infrared spectroscopic mapping of human primary intracranial tumors: a comparative study**. *Journal of Raman Spectroscopy* 2006, **37**(1-3):367-375.
84. Edwards HGM, Carter EA: **Biological Applications of Raman Spectroscopy**, vol. 24. New York: Marcel Dekker Inc.; 2001.
85. Pelton JT, McLean LR: **Spectroscopic Methods for Analysis of Protein Secondary Structure**. *Analytical Biochemistry* 2000, **277**:167-176.
86. Leikin S, Parsegian VA, Yang W-H, Walrafen GE: **Raman spectral evidence for hydration forces between collagen triple helices**. *Proceedings of National Academy of Sciences* 1997, **94**:11312-11317.
87. Walrafen GE, Chu Y-C: **Nature of collagen-water hydration forces: a problem in water structure**. *Chemical Physics* 2000, **258**:427-446.
88. Khajehpour M, Dashnau JL, Vanderkooi JM: **Infrared spectroscopy used to evaluate glycosylation of proteins**. *Analytical Biochemistry* 2006, **348**(1):40-48.

89. Potter K, Kidder LH, Levin IW, Lewis EN, Spencer RG: **Imaging of collagen and proteoglycan in cartilage sections using Fourier transform infrared spectral imaging**. *Arthritis & Rheumatism* 2001, **44**(4):846-855.
90. Camacho NP, West P, Torzilli PA, Mendelsohn R: **FTIR microscopic imaging of collagen and proteoglycan in bovine cartilage**. *Biopolymers* 2001, **62**(1):1-8.
91. Bi X, Li G, Doty SB, Camacho NP: **A novel method for determination of collagen orientation in cartilage by Fourier transform infrared imaging spectroscopy (FT-IRIS)**. *Osteoarthritis and Cartilage* 2005, **13**(12):1050-1058.
92. West PA, Bostrom MPG, Torzilli PA, Camacho NP: **Fourier Transform Infrared Spectral Analysis of Degenerative Cartilage: An Infrared Fiber Optic Probe and Imaging Study**. *Applied Spectroscopy* 2004, **58**(4).
93. Bi X, Yang X, Bostrom MPG, Camacho NP: **Fourier transform infrared imaging spectroscopy investigations in the pathogenesis and repair of cartilage**. *Biochimica et Biophysica Acta (BBA) - Biomembranes* 2006, **1758**(7):934-941.
94. Li G, Thomson M, Dicarlo E, Yang X, Nestor B, Bostrom MPG, Camacho NP: **A Chemometric Analysis for Evaluation of Early-Stage Cartilage Degradation by Infrared Fiber-Optic Probe Spectroscopy**. *Applied Spectroscopy* 2005, **59**(1527-1533).
95. David-Vaudey E, Burghardt A, Keshari K, Brouchet A, Ries M, Majumdar S: **Fourier-transform infrared imaging of focal lesions in human osteoarthritic cartilage**. *European Cells and Materials* 2005, **10**:51-60.
96. Crombie DE, Turer M, Zuasti BB, Wood B, McNaughton D, Nandakumar KS, Holmdahl R, Damme M-PV, Rowley MJ: **Destructive effects of murine arthritogenic antibodies to type II collagen on cartilage explants in vitro**. *Arthritis Res Ther* 2005, **7**(5):R927-R937.
97. Miller LM, Carlson CS, Carr GL, Chance MR: **A method for examining the chemical basis for bone disease: synchrotron infrared microspectroscopy**. *Cellular and Molecular Biology (Noisy le Grand)* 1998, **44**(1):117-127.
98. Ueno M, Shibata A, Yasui S, Yasuda K, Ohsaki K: **A proposal on the hard tissue remineralization in osteoarthritis of the knee joint investigated by FT-IR spectrometry**. *Cellular and Molecular Biology* 2003, **49**(4):613-619.
99. Derfus B, Kranendonk S, Camacho N, Mandel N, Kushnaryov V, Lynch K, Ryan L: **Human Osteoarthritic Cartilage Matrix Vesicles Generate Both Calcium Pyrophosphate Dihydrate and Apatite In Vitro**. *Calcified Tissue International* 1998, **63**(3):258-262.
100. Heger M, Mordon S, Leroy G, Fleurisse L, Creusy C: **Raman microspectrometry of laser-reshaped rabbit auricular cartilage: preliminary study on laser-induced cartilage mineralization**. *Journal of Biomedical Optics* 2006, **11**(2):024003-024008.
101. Boskey A, Pleshko Camacho N: **FT-IR imaging of native and tissue-engineered bone and cartilage**. *Biomaterials* 2007, **28**(15):2465-2478.
102. Minwook K, Xiaohong B, Walter E. Horton, Jr., Richard GS, Nancy PC: **Fourier transform infrared imaging spectroscopic analysis of tissue engineered cartilage: histologic and biochemical correlations**. *Journal of Biomedical Optics* 2005, **10**(3):031105.

103. Shaw RA, Kotowich S, Eysel HH, Jackson M, Thomson GTD, Mantsch HH: **Arthritis diagnosis based upon the near-infrared spectrum of synovial fluid**. *Rheumatology International* 1995, **15**(4):159-165.
104. Eysel HH, Jackson M, Nikulin A, Somorjai RL, Thomson GTD, Mantsch HH: **A Novel Diagnostic Test for Arthritis: Multivariate Analysis of Infrared Spectra of Synovial Fluid**. *Biospectroscopy* 1997, **3**(2):161-167.
105. Ziegler CM, Kircher P, Hassfeld S: **Analysis of Temporomandibular Joint Synovial Fluid Using Fourier-Transform/Infrared Spectroscopy**. *Journal of Oral and Maxillofacial Surgery* 2002, **60**(11):1302-1306.
106. Cui J, Loewy J, Kendall EJ: **Automated search for arthritic patterns in infrared spectra of synovial fluid using adaptive wavelets and fuzzy C-Means analysis**. *IEEE Transactions on Biomedical Engineering* 2006, **53**(5):800-809.

Chapter 2

Review of Analytical Techniques

Raman Spectroscopy

Raman spectroscopy is a vibrational spectroscopic and imaging technique based on the Raman effect. This effect is observed when electromagnetic radiation is inelastically scattered, which is caused by rotational or vibrational transitions in molecules, and is characterized by a change in net energy between the incident beam and scattered beam. Light that is scattered at lower frequency than the incident light is called a Stokes line whereas light scattered at a higher energy yields an anti-Stokes line. Monochromatic light (usually a laser) is scattered by chemical components in a sample. Raman scatter occurs when light is scattered at a slightly longer wavelength than the illuminating laser wavelength. The wavelength differences correspond to molecular vibrations and provide a unique "chemical fingerprint" of the sample.

The classical treatment of the Raman effect focuses on the interaction between a molecule's electron cloud and the electromagnetic radiation that drives inelastic scattering of light. The Raman effect is observed when a change in polarizability occurs, where polarizability is defined as the ability of a molecule's electron cloud to interact with electromagnetic radiation and produce an induced dipole. Normal modes of vibration that are accompanied by a change in polarizability are Raman active. While the classical treatment of the Raman effect is effective in describing the basic mechanism for inelastic scattering, it does not explain the intensity differences seen in anti-Stokes and Stokes scattering. Quantum mechanics allows a clearer understanding of these intensity variations in terms of simple energy level diagrams. Molecules in the ground vibrational state ($\nu=0$) will absorb energy, and upon relaxation, scatter light at a loss of energy yielding a Stokes line or return to its original energy state to yield the Rayleigh line.

Molecules in an excited vibrational state (ν=1) will absorb energy, transition to the virtual state, and relax to the ground vibrational state. Intensity variations exist because of relative population differences in the upper and lower states. At thermal equilibrium, populations follow a Boltzman distribution and there is a higher population in the ground (v=0) state, indicating a higher Stokes intensity. Since there are statistically more absorbers able to make the transition to the virtual state from the (v=0) state than there are from the (v=1) state, the Stokes line is examined in Raman spectroscopy.

Raman Spectroscopy Microscope

Although instrumentation to study the Raman effect may vary in the details, components such as the laser, notch filter and low-noise detector are standard in all dispersive Raman instruments. For dispersive Raman systems, a monochromatic light source in the visible or near-infrared (λ=480-1100 nm) wavelength range is focused on to a sample using conventional refractive optics. The most commonly used excitation wavelengths are: 488 nm, 514 nm, 532 nm, 633 nm, 785 nm, and 830 nm. Raman scatter is collected either at a 180° or 90° angle with respect to the incident beam and then directed through a filter to eliminate the Rayleigh line.

Raman microscopy is most often used for high spatial resolution spectroscopy and imaging, typically using low laser power (<20mW) to minimize sample degradation or sample heating. For biological tissue analysis, a Raman microscope coupled to a low noise charge-coupled device detector is an ideal tool for producing highly resolved spectra or images. A microscope adapted for Raman spectroscopy in the near-infrared (λ=785 nm) was used in many of the experiments described in this thesis. Some modifications to the instruments were made, which will be discussed in Chapters 3-9, but the basic apparatus remained consistent.

Near-infrared Laser

Vibrational spectroscopy of biological specimens is typically performed in the “therapeutic window” of the electromagnetic spectrum between 600-1100 nm because water and hemoglobin absorption are at a minimum, enabling the examination of minor tissue or fluid components. Also, optical penetration is relatively efficient (~3-10 mm), and optical sources and detectors are commercially available. For Raman spectroscopy, the use of near-infrared wavelengths also minimizes endogenous fluorescence signal which may otherwise obscure weak Raman signals. The experiments described in this thesis were performed in the near-infrared region at either 785 nm or 830 nm. For experiments on the Raman microscope, presented in Chapters 3, 4, 6-9, a line-shaped beam from a 785 nm Kaiser Invictus laser (Kaiser Optical Systems, Inc., Ann Arbor, MI, USA) was used. Depending on the experiment, neutral density filters (0.3-1.0 ND) were used to maintain laser intensity between 10-100 mW at the objective. For experiments using the Raman arthroscope, as presented in Chapter 5, a 785 nm or 830 nm Kaiser Invictus laser was used. The laser intensity at the end of the arthroscope was 4-20 mW.

Optical Microscope

A schematic of the Raman microscope is shown in Figure 2.1. Briefly, it consists of a standard upright optical microscope with two optical paths (excitation, collection) for Raman spectroscopy. The excitation optical path consists of lenses to sharpen the line-shaped laser beam and a dichroic mirror to direct the laser into the microscope. The laser is focused onto the specimen using an objective optimized for near-infrared wavelengths. The epi-illumination configuration of the microscope system enables collection of Raman scatter from the same objective at 180° from the sample. Raman scatter is passed through the dichroic mirror, focused by a 30 mm lens, and directed through a dispersive HoloSpec *f*/1.8 spectrograph (Kaiser Optical Systems Inc., Ann Arbor, MI, USA). Holographic notch filters are commonly used because they provide high attenuation of the Rayleigh line and also have good transmission for both Stokes and anti-Stokes scatter. The notch filter in the HoloSpec has a narrow rejection band, typically 12 nm, which enables detection of low wavenumber shifts (~50 cm^{-1}). The spectral resolution of the spectrograph was 4 cm^{-1}. A thermoelectrically cooled, back-thinned, charge-coupled device (CCD) was used as the detector. In earlier experiments, a 1024x256 chip was used and in latter experiments, a 1024x128 chip was used. The 1024 pixels corresponded to the wavelength axis and the 128, or 256 pixels, corresponded to the number of spectra recorded on the chip. Raman transects, consisting of 128 or 256 spectra spaced evenly along the line-shaped laser, enabled rapid collection of multiple spectra.

Fiber-Optic Instrumentation

Fused silica fiber-optics for delivering laser light and collecting Raman spectra has generated much interest in process analytical, remote sensing, and biomedical communities as an instrument capable of minimally-invasive or non-invasive measurements.[1-4] Two types of fiber-optic Raman probes were examined as potential add-ons to arthroscopic instrumentation. In the first configuration, a 785 nm laser was coupled into a commercially-available arthroscope and a fiber-optic Raman collection probe. In another configuration, 830 nm laser was focused onto a bundle of optical fibers surrounded by 10 collection fibers. The fiber-optic bundle was coupled through a stainless steel tube with dimensions similar to an arthroscope.

Raman Data Processing

Preprocessing

Raman data were preprocessed in Matlab (The Math Works, Natick MA, USA) using software routines developed in-house. Data were imported into Matlab using software developed in-house where they were corrected for cosmic ray spikes, dark current and variations in the CCD camera efficiency. A new approach to Raman data preprocessing was introduced in October 2008.[5] This new approach corrected for a horizontal offset of the CCD relative to the spectrograph, provided more efficient cosmic ray corrections, and completely automated the generation of a regression curve used to convert the x-axis from pixels to Raman shift measured in wavenumbers (cm^{-1}).

Univariate Analysis

If transects were used, a mean spectrum was calculated. Mean spectra were imported into GRAMS/AI© software (ThermoGalactic, Salem, NH, USA). Spectra were corrected for broadband fluorescence using a user-defined baseline correction routine. Baseline-corrected spectra were intensity normalized to a well-resolved Raman band, either at the phosphate ν_1 at ~ 958 cm^{-1} or the aromatic ring breathing mode at ~ 1002 cm^{-1}. Raman bands in normalized, baseline-corrected spectra were fitted to mixed Lorentzian/Gaussian peaks to obtain band width, height and area parameters. The resulting fit was accepted if the $R^2>0.99$ and no negative bands were generated. Figure 2.2 shows deconvolution of the amide I envelope using the peak fitting function in GRAMS/AI©. Band parameters, height or area, generated by curve fitting were used to calculate ratios that served as markers of chemical content or structure. Band area or band intensity ratios specific to the tissue or fluid are presented in Chapters 3-9.

Multivariate Analysis

Chemometrics has broadened the applicability of Raman spectroscopy for monitoring of complex biological systems. In simple mixtures, univariate methods such as measuring peak height or area are sufficient for qualitative identification based on unique peaks. Multivariate techniques, such as principal components analysis (PCA) or singular value decomposition (SVD), can separate out broadband noise, thus acting as sophisticated signal-to-noise enhancement tools with potential for automated data handling. Exploratory factor analysis and PCA have been successfully applied to Raman spectroscopy and imaging of bone specimens.[6-9] A recently developed method, band-target entropy minimization (BTEM) uses principal components generated by SVD, then examines noisy low order factors for signal associated with a known Raman band such as phosphate ν_1 at ~ 958 cm^{-1}. BTEM was first applied to recovering minor components with low signal in Fourier-transform infrared spectra with overlapping peaks from several components.[10] BTEM has been applied to Raman imaging of musculoskeletal tissue and was an important tool for identifying transient mineral species in mineralizing cranial bone tissue.[11, 12] In this thesis, SVD, PCA and BTEM are used as exploratory techniques or to identify potential contaminants in tissue or fluid specimens.

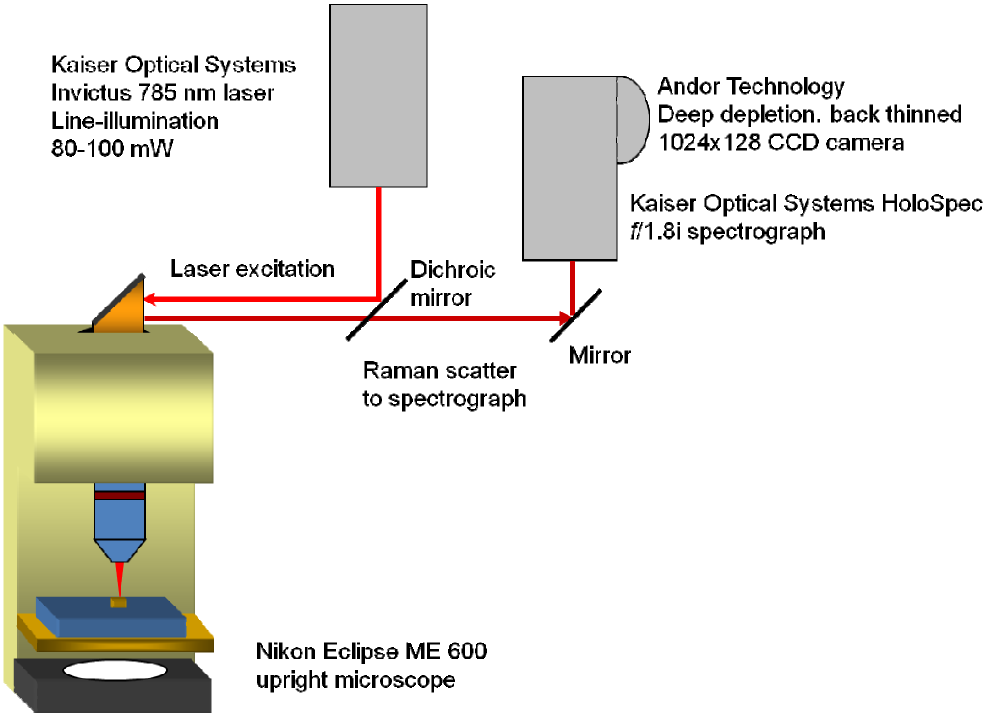

Figure 2.1: Raman microscope instrument

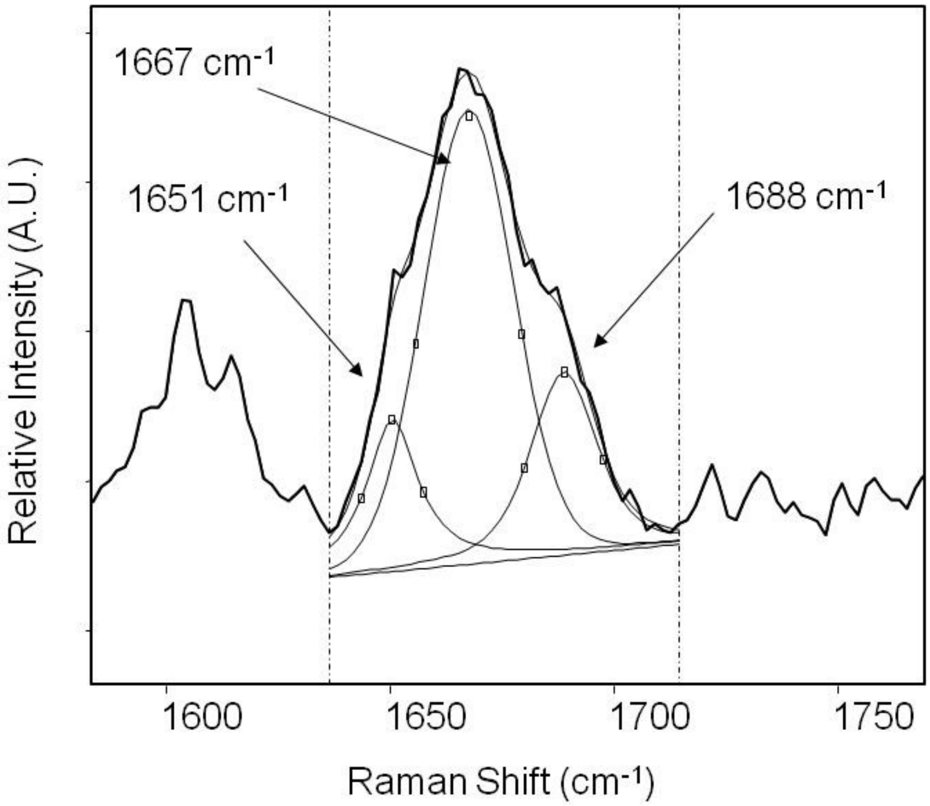

Figure 2.2: Deconvolution of the amide I envelope (1640-1720 cm^{-1}) in a spectrum of mouse ocular tissue

References

1. Hayward IP, Kirkbride TE, Batchelder DN, Lacey RJ: **Use of a Fiber Optic Probe for the Detection and Identification of Explosive Materials by Raman Spectroscopy**. *J Forensic Sci* 1995, **40**(5):883-884.
2. Clegg IM, Everall NJ, King B, Melvin H, Norton C: **On-Line Analysis Using Raman Spectroscopy for Process Control during the Manufacture of Titanium Dioxide**. *Appl Spectrosc* 2001, **55**(9):1138-1150.
3. Matousek P, Clark IP, Draper ERC, Morris MD, Goodship AE, Everall N, Towrie M, Finney WF, Parker AW: **Subsurface Probing in Diffusely Scattering Media Using Spatially Offset Raman Spectroscopy**. *Applied Spectroscopy* 2005, **59**(4):393-400.
4. Schulmerich MV, Dooley KA, Vanasse TM, Goldstein SA, Morris MD: **Subsurface and Transcutaneous Raman Spectroscopy and Mapping Using Concentric Illumination Rings and Collection with a Circular Fiber-Optic Array**. *Applied Spectroscopy* 2007, **61**:671-678.
5. Esmonde-White FWL, Schulmerich MV, Esmonde-White KA, Morris MD: **Automated Raman spectral preprocessing of bone and other musculoskeletal tissues**. In: *Optics in Bone Biology and Diagnostics: 2009; San Jose, CA, USA*: SPIE; 2009.
6. Timlin JA, Carden A, Morris MD, Rajachar RM, Kohn D: **Raman spectroscopic imaging markers for fatigue-related microdamage in bovine bone**. *Anal Chem* 2000, **72**:2229-2236.
7. Goodyear SR, Gibson IR, Skakle JMS, Wells RPK, Aspden RM: **A comparison of cortical and trabecular bone from C57 Black 6 mice using Raman spectroscopy**. *Bone* 2009, **44**(5):899-907.
8. Carden A, Rajachar RM, Morris MD, Kohn D: **Ultrastructural changes accompanying the mechanical deformation of bone tissue: a Raman imaging study**. *Calcified Tissue International* 2003, **72**:166-172.
9. Tarnowski CP, Ignelzi MA, Morris MD: **Mineralization of Developing Mouse Calvaria as Revealed by Raman Microspectroscopy**. *Journal of Bone and Mineral Research* 2002, **17**(6):1118-1126.
10. Widjaja E, Li C, Chew W, Garland M: **Band-Target Entropy Minimization. A Robust Algorithm for Pure Component Spectral Recovery. Application to Complex Randomized Mixtures of Six Components**. *Anal Chem* 2003, **75**:4499-4507.
11. Widjaja E, Crane N, Chen T, Morris MD, Ignelzi Jr. MA, McCreadie B: **Band-Target Entropy Minimization (BTEM) Applied to Hyperspectral Raman Image Data**. *Applied Spectroscopy* 2003, **57**(11):1353-1362.
12. Crane NJ, Popescu V, Morris MD, Steenhuis P, Ignelzi JMA: **Raman spectroscopic evidence for octacalcium phosphate and other transient mineral species deposited during intramembranous mineralization**. *Bone* 2006, **39**(3):434-442.

Chapter 3

Chemical Alterations in Subchondral Bone

Introduction

Vibrational spectroscopy is a proven analytical tool to understand chemical changes that are associated with pathological conditions in tissue.[1, 2] In particular, infrared (IR) and Raman spectroscopy of mineralized tissue can provide detailed chemical information on the mineral and collagen matrix components of these complex tissues. Infrared and Raman spectroscopy have been applied to intact tissue samples, and both are well-established methods for the analysis of bone.[3-6] Both methods can provide insight into the interactions between the mineral and matrix or the chemical properties of a specific component by spectral imaging or point spectroscopy.[7]

Fourier-transform infrared spectroscopy (FT-IR) of cartilage has been described in detail.[8-11] Infrared spectra of non-mineralized cartilage are dominated by protein signatures and do not contain mineral bands. Recent studies using FT-IR have correlated tissue damage with changes in the amide III and amide II envelopes and in the ~ 1340 cm^{-1} band. Spectral features from proteoglycans and collagen have been mapped using infrared imaging with a spatial resolution approaching 10 micrometers.[8, 11] Recently, West and colleagues have demonstrated that infrared (IR) spectroscopy can detect collagen degradation in arthritic human knee explants and that spectra can be obtained through 1 meter of infrared-transmitting optical fiber.[12] Moreover, alterations in the collagen fibril orientation in articular cartilage, the result of collagenase treatment, are evident in polarized FT-IR images.[13]

Raman spectroscopy has been used in transgenic mice to study the effects of genetic defects on the structure-function relationships in bone matrix.[14] There are no reports of

Raman spectroscopy applied through articular cartilage to the underlying intact subchondral bone plate. Currently, there is renewed interest in the role of subchondral bone in the progression of osteoarthritis (OA).[15] In traditional models of osteoarthritis, changes to subchondral bone are secondary to cartilage damage. A current postulate is that the subchondral bone is damaged early and this damage coincides with articular cartilage damage.[16] Moreover, it is unclear if damage to subchondral bone is arthrogenic or occurs as a response to damage in cartilage. As characterization of pathological and normal states in bone shaft specimens has already been demonstrated by Raman spectroscopy, we hypothesized that Raman spectroscopy would identify changes in subchondral bone components at the molecular level.

Using a Raman microprobe, we obtained spectral signatures that are attributed to subchondral bone and protein features that are predominately attributed to type I collagen in bone. Articular cartilage is approximately 250 micrometers thick in healthy murine specimens. As a result of the relative Raman scattering efficiencies, and tissue thicknesses sampled from the cartilage and bone, mineral bands from apatite phosphate at ~958 cm^{-1} and carbonate at ~1070 cm^{-1} are expected to dominate Raman spectra taken from murine femoral or tibial condyles. We demonstrate that the Raman microprobe can be used to obtain spectral data directly from subchondral bone using two sets of mice populations. The experimental methodology established in this study serves as a basis to expand Raman spectroscopic analysis to articular cartilage.

The Del1 (+/-) mouse has an articular phenotype that has been well characterized for early-onset cartilage damage.[17] Heterozygous Del1 (+/-) transgenic mice contain 6 copies of this 39 kb transgene; the type II collagen chain is truncated and affects the articular cartilage. Previous studies have shown Del1 (+/-) mice to develop age-dependent histological features of osteoarthritis, with superficial fibrillation observed as early as 3-4 months of age on tibial cartilage. By age 3 months, Del1 (+/-) mice showed articular cartilage changes similar to 9-month-old wild-type (wt) mice and all male Del1 (+/-) mice showed severe degeneration of femoral articular cartilage by age 9 months.[17] Polarized light microscopy showed greatly reduced birefringence of the uncalcified articular cartilage in Del1 (+/-) mice, indicating decreased and/or disorganized collagen fibers. Other progressive changes included sclerosis of underlying bone, abnormal chondrocytes (pyknotic chondrocyte nuclei with clusters of reactive chondrocytes), and increased matrix staining with Safranin O. We hypothesize that Raman spectra taken from femoral condyles of Del1 (+/-) mice will reflect chemical changes in the mineral of the subchondral bone that result from osteoarthritis-like damage. Raman data obtained were compared to the widely accepted histologic scoring system for OA, the modified Mankin score, by two blinded observers.

Materials and Methods

Raman microprobe

A near-infrared Raman microprobe was constructed in-house. The near-IR excitation laser, 785 nm (Kaiser Optical Systems Invictus), was line-focused through an Olympus BH-2 microscope. A 20×/0.75 NA Zeiss Fluar objective, with a working distance of approximately 0.66 mm, was used throughout the studies. Incident power on the specimen was dimmed to approximately 80 mW with a 0.25 O.D. neutral density filter to minimize the effect of specimen burning. The light was focused to a line approximately 100 micrometers long and 1 micrometer wide. Raman-scattered light was collected through the objective and dispersed by an axial transmissive spectrograph (Kaiser Optical Systems Holospec f/1.8i) operated at 4 cm^{-1} resolution. The scattered light was integrated for 5 minutes on a 1024 x 256 back-illuminated deep depletion CCD camera (Andor Technology DU 420-BR-DD), which is sensitive in the near-infrared. Because line-focusing was used, transects consisting of 254 Raman spectra each, spaced at intervals of 0.5 micrometers along the line, were taken at each sampling area on the femur.

Raman spectroscopic analysis of tissue

Femurs were examined from 46 mouse specimens, 20 Del1 (+/-) transgenic and 26 wild-type mice. One or both femurs from each animal were examined by Raman spectroscopy. The femurs, with the articular cartilage of the knee joints intact, were isolated en bloc and stored in 70% (v/v) ethanol at 4ºC until Raman analysis. Femurs were removed from the ethanol storing solution and Raman spectra were taken under ambient temperature and relative humidity conditions. Prior to spectroscopic examination, the femurs were allowed to sit under an unfocused 785 nm laser for 5 minutes to evaporate surface ethanol and to slightly photobleach the femurs to minimize the risk of burning the specimen. Femoral condyles were examined directly by the Raman microprobe, without pre- processing such as fixation or staining. Three to 10 transects were taken across the entire condyle surface, with a majority of transects taken along the interior edges of the medial and lateral condyles. Transects taken from the posterior or anterior cruciate ligaments, located between the femoral condyles, were easily distinguishable from the condyles in both light microscope images and Raman spectra (data not shown), and were not used in band area calculations.

Raman data processing

From each transect, a normalized mean spectrum was generated to offset the effect of a single spectrum on the arithmetic mean. Three to ten transects were obtained from each femur. Transects were imported in Matlab (v 6, Release 12.1, The Math Works), where spectra were corrected for dark signal and averaged into a normalized spectrum. Background signal from normalized spectra was removed using a user-defined multi-point baseline routine, and Raman bands were fit using the curve-fit routine in GRAMS/AI© (ThermoGalatic) software. Band envelopes in the baseline-corrected spectra were fitted to mixed Gaussian/Lorentzian bands. Results from the curve-fitting routine were used if all band intensities were non-negative and the fit yielded an R^2 value of 0.99 or greater. The curve-fitting procedure generally yielded bands that were readily identified based on Raman band assignments from previous experiments on bone matrix as summarized in Table 3.1.[5] Band areas calculated from the curve-fit routine were used to measure carbonate-to-phosphate ratios (carbonate 1070 cm^{-1}: phosphate 958 cm^{-1} and 945 cm^{-1}), and the mineral-to-matrix ratio using the CH_2 band vibration at ~1450 cm^{-1} as a marker for matrix content. Microcomputed tomography (Micro CT) images were collected from femurs of aged (23-28 months) mice. Bone quality parameters were calculated from micro CT images and are shown in Table 3.2.

Statistical analysis

Three to ten Raman transects were taken on each femur, and a normalized mean spectrum from each transect was used to calculate band areas. Band areas were normalized against the sum of the bands to minimize the effect of varying signal-to-noise ratios. Raman data from mice in the Del1 (+/-) study were grouped into age subcategories (1-3, 4-6, 7-9, 10-12, 12-18 and 23-28 months) for each genotype (wild-type or transgenic). Band area ratios were calculated for each spectrum, and were sorted by age group and genotype. P-values were determined using two-tailed Student's T-test and used to compare band area ratios from wild-type and transgenic mice at each single time point. N-way ANOVA was used to determine longitudinal effects of age, transgenic status, and combined effects on Raman band area rations. A six-by-two experimental design was used in the study of Del1 (+/-) transgenic and wild-type mouse femurs by Raman spectroscopy. The null hypothesis was that Raman band area ratios were independent of age or transgenic status. Raman data were sorted into six age groups (1-3, 4-6, 7-9, 10-12, 12-18, and 23-28 months) and two transgenic status groups (wild-type or Del1(+/-) transgenic). Outcome measures were the mineral-to-matrix ratio and the carbonate-to-phosphate ratio. Results from ANOVA tests are shown in Table 3.3. A post-hoc power analysis was performed to determine the power of an ANOVA, repeated measures, analysis within the main effects and interaction of the main effects. The post-hoc power analysis indicated 93% power to examine the transgenic status effect, 67% power to examine the age effect, and 43% power to examine a combined age and transgenic status effects.

Animal models

Del1 (+/-) transgenic mice were provided by Drs. E.I. Vuorio and A.-M. Säämänen at the University of Turku, Finland. Del1 (+/-) and wild-type mice were kept 1-5 per cage, allowed to ambulate ad lib and were given water and standard chow ad lib. Del1 (+/-) and wild-type mice were housed together under the same conditions. Del1 (+/-) transgenic and wild-type mice were sacrificed at 10 ages: 2, 2.5, 3, 5, 7, 9, 10, 12, 13, 16, 23, 26, and 28 months, using anesthesia overdose. Wild-type mice were sacrificed at additional time points of 4, 6 and 20 months. All ages were represented by at least two pairs of sacrificed mice except for the 16-month group, for which only one pair was sacrificed. Each mouse had at least one femur examined by Raman spectroscopy. The femurs and stifle joints were isolated using an Olympus SZ30 dissecting microscope under 10X power. Genotyping was performed on tail snips using the REDExtract-N-Amp™ Tissue PCR Kit from Sigma. The DNA was then expanded with PCR using the following primers: 5'-GCT CCC TTA CTA TCT TCT TGT CCC TC-3' (labeled exon6) and 5'-CAG ACG GTA GCT TGG GTA GAA GAT-3' (labeled exon8). The PCR products were run on a 1% agarose gel using TAE buffer, and stained with ethidium bromide. A 218 bp band was identified in the transgenic mice, while a 368 bp band was seen in the wild-type mice. The difference in the size of the PCR products was easily resolved using agarose gel electrophoresis and ethidium bromide staining. Genotyping of tail snips from Del1 (+/-) transgenic mice confirmed the presence of the COL1A2 transgene when compared to wild-type mice.

Histology

The whole stifle joints were stored in 10% formalin, decalcified over 1-2 days in a solution containing sodium citrate and formic acid. The samples were then embedded in paraffin, and cut into serial coronal sections 5 μm thick. The sections containing the femur-tibia articulation were stained with both hematoxylin-eosin and safranin-O for determination of a modified Mankin score, as per Turner et al.[18] The samples were not labeled for age or transgene status, and were read by 2 independent observers. Total Mankin scores were compared for 6 different ages (2, 3, 5, 10, 12, and 13 months).

Results

As shown in Figure 3.1, Raman spectra of subchondral bone are comprised primarily of contributions from type I collagen and carbonated apatite mineral. The apatite phosphate ν_1 band at 958 cm^{-1} is strong in the raw spectrum but less intense peaks are difficult to clearly visualize. Raman bands corresponding to phosphate and carbonate groups in the apatite lattice (958 cm^{-1} and 1070 cm^{-1} respectively) were readily observed in baseline corrected spectra. Raman spectra of solid samples of type I collagen, type II collagen, proteoglycan and chondroitin-6-sulfate were obtained in order to understand spectra contributions from polysaccharides and collagen found in cartilage (not shown here). Additionally, we examined articular cartilage surfaces from canine patella and were able to confirm that polysaccharide components do not make a significant contribution to the Raman spectrum of subchondral bone. Because bone mineral is a strong Raman scatterer, and murine cartilage is very thin (~250 μm), we were not surprised to observe that the articular cartilage layer has a minimal spectral contribution.

A previous report had grouped Del1 transgenic and wild-type mice according to progression of damage to articular cartilage [17]. Age intervals, 1-3, 4-6, 7-9, 10-12, 12-18 months, corresponding to maturation, young adult, adult, older adult and aged stages of mouse development were used to group Raman data. An additional age group of 23-28 months was included in this study. We focused primarily on the mineral components of the Raman spectrum because type II collagen found in cartilage has bands in the amide III and amide I envelopes, and CH_2 wag region that are similar to type I collagen found in bone. Thus the Raman spectra obtained during these studies contain matrix bands that arise from the cartilage and bone. The contribution of cartilage to the calculation of band area ratios that describe collagen secondary structure, such as the amide I or amide III band area ratio, is unclear.

Figures 3.2 and 3.3 illustrate longitudinal effects in the mineral component of wild-type and Del1 (+/-) transgenic mice; the y-axis error bars indicate the standard deviation. The mineral-to-matrix ratio (1450 cm^{-1}:958 cm^{-1}) provides an indication of bone mineralization, and the carbonate-to-phosphate (1070 cm^{-1}:958 cm^{-1}) ratio was used to describe the degree of carbonate substitution in the apatite crystal lattice. Table 3.2 shows bone quality parameters obtained from microcomputer tomography of older Del1 (+/-) transgenic and wild-type mice.

The modified Mankin score was used to evaluate histopathologic changes of OA on the femoral articular cartilage of Del1 (+/-) and wild-type mice. Pooled Mankin scores are shown in Figure 3.4. In contrast to other studies using the Del1 (+/-) transgenic model, the scores did not consistently increase as a function of age. The only statistically significant differences over age were an increase in Mankin score between the 5 and 12 month old wild-type mice (p=0.045) and a decrease in Mankin score between the 2 and 3 month old Del1 (+/-) mice (p=0.020). Mankin scores were not consistent between observers.

Discussion

In humans, mutations in COL2A1 gene have been linked to familial OA, as well as mild chondrodysplasia, Stickler and Wagner syndromes, to more lethal syndromes such as type II achondrogenesis (Langer-Saldino syndrome).[19] Similarly, the Del1 (+/-) transgenic mouse exhibits retarded skeletal development and is susceptible to early-onset progressive articular degeneration. Matrix metalloproteinase-13 mRNA and its inhibitor TIMP-1 are also expressed during early cartilage degeneration in this OA model, and are localized in the synovial tissue, deep calcified cartilage, and subchondral bone.[20] These may be involved in tissue remodeling in response to cartilage damage.

Most of the previous characterization of the Del1 (+/-) phenotype has relied on the use of histologic parameters, including the use of the modified Mankin score. Within the Mankin system scores are given for surface integrity, hyper- and hypo-cellularity, and matrix quality using hematoxylin/eosin and Safranin-O staining. The final score ranges from 0 (no osteoarthritis) to 20 (severe osteoarthritis). The modified Mankin score has been validated as an adequate measure of histological damage in at least one animal model of OA.[21] The authors of this validation study examined rabbit articular cartilage, comparing wild-type to experimental OA (either medial meniscectomy or plaster immobilization extension), with each sample being evaluated by two blinded observers. They found that most scores were less than 6, with reasonable intra-observer agreement (standard deviation varying between 1.5 and 2.6 points). Other researchers, however, have questioned the validity of the scoring system and have identified inherent problems associated with both inter- and intra-observer variation.[22] In our study we observed significant inter-observer variation and the mean score did not consistently increase as a function of age or transgenic status. Statistical analyses showed no significant differences between Del1 (+/-) and wild-type mice in total scores at ages 2, 3, 10, or 13 months of age. While the data are not statistically significant, histology data suggests that the phenotype expression for OA damage is maximized by the time the Del1 (+/-) transgenic mice reach age 5 months instead of demonstrating a progressive degeneration of cartilage that is expected in OA. It is possible that, after 5 months of age, other joint tissues in Del1 (+/-) transgenic mice compensate for loss of cartilage integrity. An experiment to further test this hypothesis would include examination of a non-load bearing joint in the Del1 (+/-) transgenic mice to test for possible mechanical-induced compensation.

By contrast to variability observed in histology scoring, Raman spectral features were consistent across femur specimens. A comparison of the femur tissue spectra with reference collagen spectra indicated that mineral components and the collagen protein make the major contributions in spectra taken from subchondral bone. However, due to the similarities seen in reference collagen spectra, it is unclear if the collagen spectral contributions are from type I collagen, type II collagen, or a mixture of both collagen types. Because our microscope system operates in a non-confocal configuration, it is likely that spectra collected from the mouse femur specimens arose primarily from subchondral bone with minor contributions from articular cartilage.

Common spectral features from hydroxyproline, aromatic ring breathing, amide III and amide I (880 cm^{-1}, 1001 cm^{-1}, 1220-1280 cm^{-1} and 1600-1720 cm^{-1}) were observed from both types I and II collagen. Raman spectra of type II collagen have a low signal-to-noise ratio, even after a 10 minute signal integration time (data not shown). Because the differences in band position between types I and II collagen were generally 2-3 cm^{-1} and were within the spectral resolution of the instrument (4 cm^{-1}). Band positions in the amide I and amide III envelopes could not be used to distinguish between types I and II collagen. The only possible exception is the band maximum in the amide I envelope, for type II collagen it is ~1671 cm^{-1} and for type I collagen it is ~1655 cm^{-1}. However, in spectra collected from subchondral bone, the amide I envelope was sufficiently broad to incorporate the two bands, and band fitting routinely found more than two bands under the amide I envelope.

We found that the changes in Raman band area ratios from Del1 (+/-) transgenic mice were subtle and, in most age groups, the band area ratios were statistically indistinguishable from those of wild-type mice. One possible explanation for these observations is the small number of wild-type and Del1 (+/-) animals that were examined in each age group due to the limited availability of mouse specimens. The effect of a cartilage depth that varies with genotype and age may complicate collection of light scattered from subchondral bone. Calculation of matrix-related band areas, such as the amide III, amide I envelopes and 1450 cm^{-1} band, may have been affected by a variable intra-and inter-specimen cartilage depth. Moreover, the similarities in Raman spectra from types I and II collagen complicate identification of individual contributions from cartilage and bone. Regardless, these preliminary studies are encouraging because of the apparent trends observed in the mineral-to-matrix and carbonate-to-phosphate ratios.

The mineral-to-matrix ratio (MTMR) was used in previous bone Raman studies to examine the extent of mineralization. Markers of organic matrix included the amide I band at ~1667 cm^{-1}, the area under the amide I envelope (1600-1720 cm^{-1}), and the CH_2 wag at 1450 cm^{-1}. [5, 23, 24] In this study, the 1450 cm^{-1} band was used as a marker for the organic matrix because it is less susceptible to conformation changes and thus, a more robust measurement of matrix content. The 1450 cm^{-1} band may include contributions from either the type I collagen in bone, the type II collagen in cartilage or a mixture of both. Despite contributions from both the cartilage and bone matrix in the 1450 cm^{-1} band, we postulate that chemical changes in the mineral, rather than a variable cartilage depth, is the underlying reason why we observe a difference in the MTMR. We hypothesized that, even if the 1450 cm^{-1} band contains contributions from both cartilage and bone, then the MTMR would increase as the cartilage becomes thinner with age or surface erosion. Histopathology scoring of cartilage in wild-type and Del1 (+/-) mice were inconclusive and Mankin scores did not indicate age-related or transgene-related cartilage damage. Thus, we are confident that cartilage erosion was minimal and did not significantly affect mineral-to-matrix calculations.

Figure 3.2 presents MTMR data for wild-type and Del1 (+/-) mice. In both types of mice, this ratio changes to show that the tissue becomes less mineralized as mice age. Raman data shows a trend that bone in Del1 (+/-) transgenic mice is less mineralized than bone from wild-type mice. These results support previous histology findings in Del1 (+/-) transgenic mice which found that Del1 (+/-) transgenic mice exhibit retarded long bone growth, reduced long bone dimensions and reduced mineralization in bone.[25]

Micro CT was used to examine subchondral bone in older Del1 (+/-) transgenic and wild-type mice (23-28 months old) and confirm the underlying reason why Raman studies indicated a lower MTMR in Del1 (+/-) mice. Table 3.2 shows that femurs from Del1 (+/-) transgenic mice have less mineralized bone tissue, as indicated by bone mineral content and bone mineral density. Trabecular architecture in cancellous bone was also affected by the Del1 (+/-) transgene, and we observed fewer trabeculae and increased spacing between trabeculae in the transgenic mice. The micro CT data suggest that cancellous bone tissue in Del1 (+/-) mice is less mineralized resulting in a diminished quality in bone architecture. Similar results have been previously reported.[26] Micro CT data also support Raman spectroscopy results showing that subchondral bone in Del1 (+/-) transgenic mice is less mineralized.

The MTMR was not significantly different in transects from Del1 (+/-) transgenic mice in the aged mice, yet micro CT data suggests large bone mineral density differences between wild-type and Del1 (+/-) transgenic mice (0.74 vs. 0.26). We suspect that the discrepancy arises because of differences in the tissues examined. Raman spectra collected for this study did not contain signatures unique to bone marrow lipids, which indicate that the Raman microscope is sampling primarily subchondral bone with possible contributions from non-calcified and calcified cartilage. By contrast, the micro CT analyzed both cortical and cancellous bone. We hypothesize that the differences observed in the microCT measurements of bone mineral density arose because of differences in the cancellous bone. It is possible that cancellous bone remodeling was also affected by a truncated type II collagen chain. A future study would be to use Raman spectroscopy and micro CT to examine cancellous bone in OA models. Examination of cancellous bone by Raman spectroscopy may reveal pathological alterations in trabeculae architecture or cancellous bone remodeling as response to OA.

As seen in Figure 3.3, the carbonate-to-phosphate ratio in Del1 (+/-) femurs follows the same general trend as the data from age-matched wild-type femurs. But, after 2-4 months, the band area ratio value is consistently higher in Del1 (+/-) transgenic mice. The carbonate (CO_3): phosphate (PO_4) band area ratio, 1070 cm^{-1}: (958 cm^{-1} + 945 cm^{-1}), is an indication of carbonate substitution into the mineral. The carbonate-to-phosphate ratio data indicates that the extent of carbonate ion substitution into the apatite mineral is greater in bone from Del1 (+/-) mice. Previous bone Raman studies have shown that increases in the carbonate-to-phosphate ratio is associated with increased bone stiffness.[27, 28] Previous research showed that osteoarthritic subchondral bone is stiffer than normal subchondral bone, which support our observations in the carbonate-to-phosphate Raman data.[29, 30]

Alterations to the molecular composition of murine subchondral bone as response to age and defective type II collagen formation were observed using Raman spectroscopy. Subchondral bone was less mineralized, concurrent with slightly elevated carbonate content in bone mineral, in Del1 (+/-) transgenic mice. It is possible that the increased carbonate substitution occurred in response to deficient mineralization. Because no statistically significant changes in cartilage morphological or ultrastructural features were observed in histology specimens from wild-type or Del1 (+/-) transgenic mice, we think that chemical composition changes in subchondral bone occurred independent from changes to cartilage tissue. However, we cannot conclude that alterations to subchondral bone chemical composition are arthritogenic in nature.

ANOVA tests revealed that MTMR and carbonate-to-phosphate ratios were dependent on age and transgenic status, as shown in Table 3.3. The carbonate-to-phosphate ratio provided the most compelling results for the effect of the both the Del1 (+/-) transgene and age. Longitudinal trends in the carbonate-to-phosphate ratio was significantly different when comparing wild-type and Del1(+/-) transgenic mice. Other Raman spectroscopy studies of altered bone chemistry showed that the carbonate-to-phosphate ratio is altered at damaged sites.[27, 31] It is possible that future studies will show statistically significant elevated carbonate-to-phosphate ratio values in damaged areas of subchondral bone. The MTMR did not have a significantly different longitudinal trend between wild-type mice and Del1 (+/-) transgenic mice. ANOVA tests suggest a trend toward statistical significance of MTMR in future studies that may be revealed in an expanded test with more mouse specimens, especially when comparing mice in the young adult vs. adult developmental stages (4-6 months vs. 7-9 months).

Conclusions

To date, it is unclear if the primary tissue of origin in osteoarthritis is the articular cartilage or subchondral bone. Raman spectroscopy may provide new insights into the structure-function relationships that determine the properties of the complex bone-cartilage interface. Raman spectra collected from subchondral bone under a layer of intact articular cartilage were used to identify chemical changes to the bone mineral that may result from genetic mutation of extracellular matrix molecules or with aging. Variations in cartilage depth or composition due to natural aging, or disease progression may affect calculation of Raman matrix bands. In our studies, subtle alterations to the chemical composition of subchondral bone are evident at early ages.

Because of the large degree of spectral overlap, we concluded that we could not use Raman bands from collagen to differentiate cartilage from subchondral bone. We propose that a Raman spectrum of normal intact cartilage would be a more suitable pure component spectrum because there are spectral contributions from sulfated glycosaminoglycans which may be used to distinguish cartilage matrix from bone matrix. Normal cartilage specimens as a spectroscopic standard was proposed in a previous infrared study because it is more representative of the interactions that occur between collagen matrix molecules.[32] Sulfated glycosaminoglycans have a strong band at ~ 1061 cm^{-1} that does not overlap with any of the major bands in bone collagen or the carbonate ν_1 stretch at ~ 1070 cm^{-1} of bone mineral. We envision a study of cartilage/subchondral bone cross-section specimens using Raman spectroscopy. Raman spectra would be collected from each unmineralized cartilage zone, calcified cartilage, subchondral bone plate and the cancellous bone. Bands in Raman cartilage spectra from sulfated glycosaminoglycans could then be validated by staining the cross-section specimens for cartilage proteoglycan content using Safranin O.

Finally, it is intriguing to conceptualize the application of Raman spectroscopy as a diagnostic modality. The carbonate-to-phosphate band area ratio is calculated using bands that are not obscured by collagen protein signal. Observation of the strong phosphate ν_1 band at 958 cm^{-1} and the carbonate band at ~1070 cm^{-1} in spectra that have not been baseline corrected indicates that calculation of this ratio would be possible in specimens with a thicker articular cartilage layer. Fiber-optic technology is frequently used through arthroscopes to evaluate knee, hip, shoulder and ankle joints in the clinical setting. Silica fiber optic Raman probes have been used to evaluate coronary artery calcifications in a clinical experimental setting[33], as well as in animal studies to diagnose cellular dysplasia in cancer models.[34] The non-destructive nature and sensitivity of Raman spectra to subtle tissue changes are attractive features in developing clinically relevant platforms such as a fiber-optic insert within an arthroscope. Potentially, Raman spectroscopy could be utilized through a combined arthroscopic imaging/Raman spectroscopic fiber optic system to diagnose early OA, or follow the response of damaged cartilage or subchondral bone to therapeutic intervention. We explore prototype designs of a fiber-optic arthroscope system for Raman spectroscopy in Chapter 5.

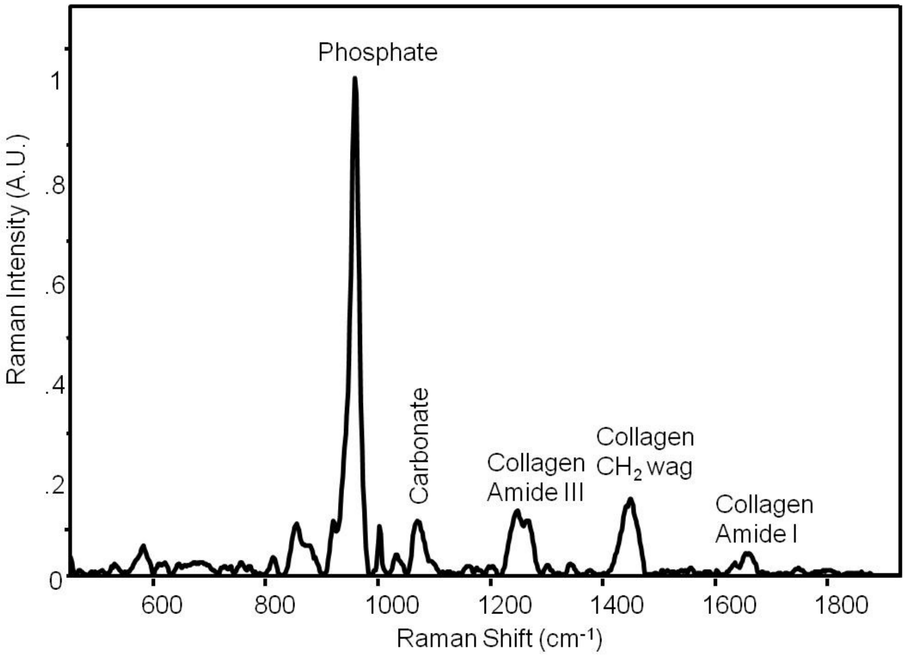

Figure 3.1: Raman spectrum of subchondral bone

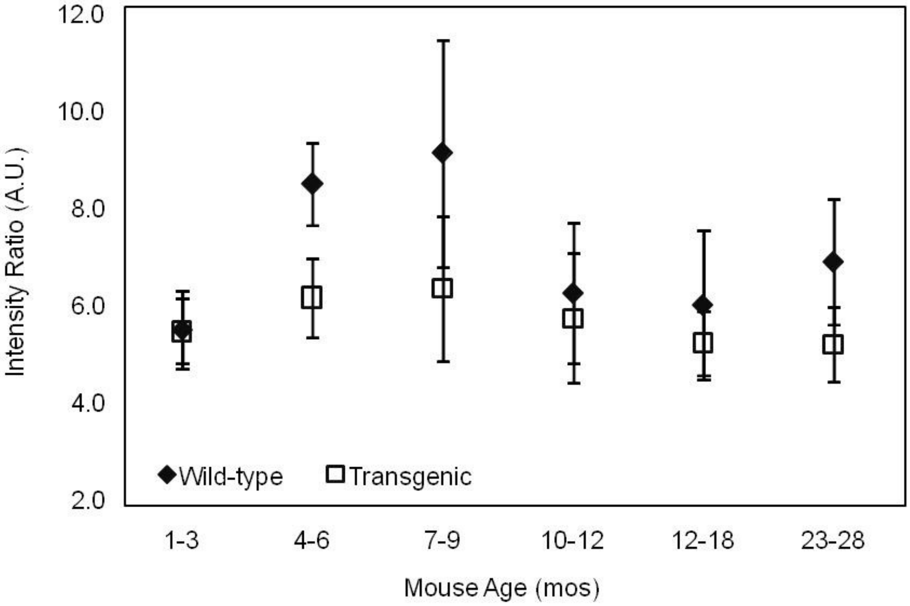

Figure 3.2: Mineral-to-matrix ratio is a spectroscopic marker of mineralization in femoral condyles from Del1 (+/-) transgenic and wild-type mice

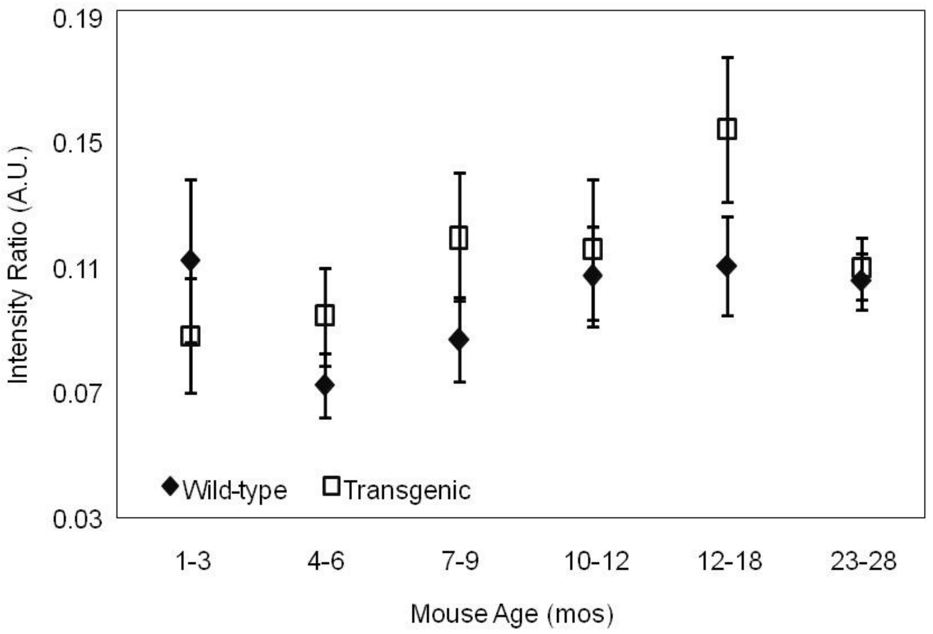

Figure 3.3: Carbonate-to-phosphate ratio is a spectroscopic marker of carbonate substitution into the apatite crystal lattice in femoral condyles from Del1 (+/-) transgenic and wild-type mice

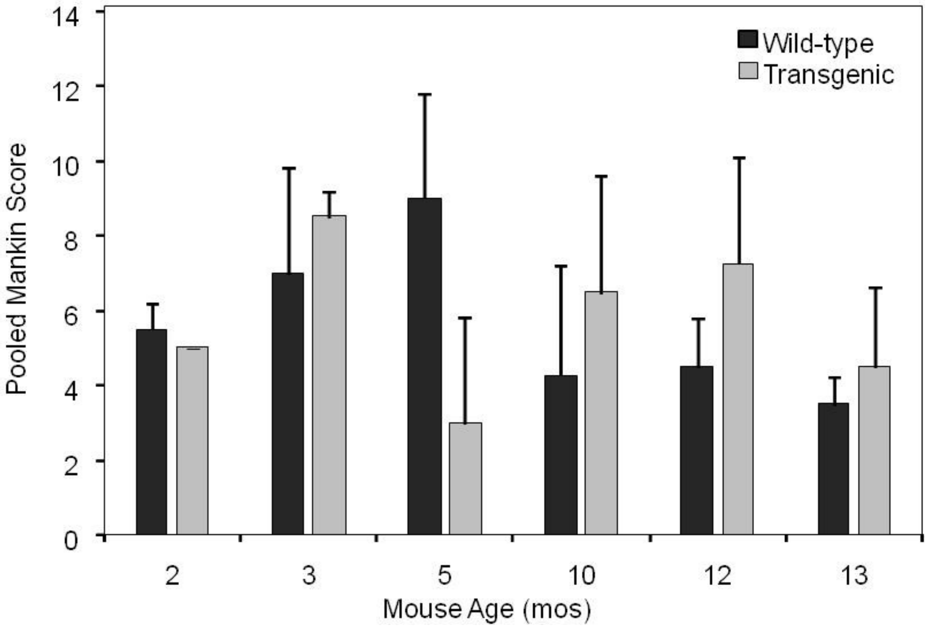

Figure 3.4: Histopathology analysis was performed on femur stifle joints from wild-type and Del1 (+/-) transgenic mice. Modified Mankin scoring was used to grade morphological and ultrastructural cartilage damage.

Raman Shift (cm^{-1})	Band Assignment	Component in Bone
850	ν_{CC} hydroxyproline	Collagen Matrix
876	ν_{CC} hydroxyproline	Collagen Matrix
945	disordered apatite	Apatite Mineral
958	ν_1 PO_4^{3-}	Apatite Mineral
1001	Phenylalanine	Collagen Matrix
1070	ν_2 CO_3^{2-}	Apatite Mineral
1240	Amide III (random coil)	Collagen Matrix
1270	Amide III (α-helix)	Collagen Matrix
1450	CH_2 wag	Collagen Matrix
1667	Amide I	Collagen Matrix

Table 3.1: Raman band assignments for subchondral bone

Bone Parameter	Wild-Type	Del1 (+/-) Transgenic
Bone Mineral Content (mg)	0.74±0.5	0.26 ±0.07
Bone Mineral Density (mg/cc)	116.11 ±45.6	39.22 ±11.5
Bone Volume Fraction	0.09 ± 0.08	0.003 ±0.002
Bone Volume/Tissue Volume	0.1 ± 0.08	0.003 ±0.002
Bone Surface/Tissue Volume	52.91 ± 6.11	94.15 ±30.79
Trabecular Thickness	0.038 ±0.004	0.022 ±0.006
Trabecular Number	2.43 ± 1.89	0.12 ±0.07
Trabecular Spacing	0.78 ± 0.70	13.83 ±14.23

Table 3.2: Bone quality parameters obtained from microcomputed tomography of older (23-28 months) Del1 (+/-) transgenic and wild-type mice. Average values with 95% confidence interval.

Raman Band Area Ratio	Carbonate-to-phosphate	Mineral-to-matrix
Pr>F, age	1.24×10^{-5}	7.83×10^{-5}
Pr>F, transgenic status	0.005	0.003
Interaction?	Yes	No

Table 3.3: ANOVA tests reveal that the mineral-to-matrix ratio (MTMR) and carbonate-to-phosphate ratio are dependent on age and transgenic status.

References

1. Jackson M, Mantsch HH: **Pathology by Infrared and Raman Spectroscopy**. New York: John Wiley and Sons LTD; 2002.
2. Edwards HGM, Carter EA: **Biological Applications of Raman Spectroscopy**, vol. 24. New York: Marcel Dekker Inc.; 2001.
3. Drumm CA, Morris MD: **Microscopic Raman line-imaging with principal component analysis**. *Applied Spectroscopy* 1995, **49**:1331-1337.
4. Christensen KA, Morris MD: **Hyperspectral Raman microscopic imaging using Powell lens line illumination**. *Applied Spectroscopy* 1998, **52**(9):1145-1147.
5. Timlin JA, Carden A, Morris MD: **Chemical Microstructure of Cortical Bone Probed by Raman Transects**. *Applied Spectroscopy* 1999, **53**(11):1429-1435.
6. Timlin JA, Carden A, Morris MD, Rajachar RM, Kohn D: **Raman spectroscopic imaging markers for fatigue-related microdamage in bovine bone**. *Analytical Chemistry* 2000, **72**:2229-2236.
7. Carden A, Morris MD: **Application of vibrational spectroscopy to the study of mineralized tissues (review)**. *Journal of Biomedical Optics* 2000, **5**(3):259-268.
8. Camacho NP, West P, Torzilli PA, Mendelsohn R: **FTIR microscopic imaging of collagen and proteoglycan in bovine cartilage**. *Biopolymers* 2001, **62**(1):1-8.
9. Bi X, Li G, Doty SB, Camacho NP: **A novel method for determination of collagen orientation in cartilage by Fourier transform infrared imaging spectroscopy (FT-IRIS)**. *Osteoarthritis and Cartilage* 2005, **13**(12):1050-1058.
10. Miller LM, Carlson CS, Carr GL, Chance MR: **A method for examining the chemical basis for bone disease: synchrotron infrared microspectroscopy**. *Cellular and Molecular Biology (Noisy le Grand)* 1998, **44**(1):117-127.
11. Potter K, Kidder LH, Levin IW, Lewis EN, Spencer RG: **Imaging of collagen and proteoglycan in cartilage sections using Fourier transform infrared spectral imaging**. *Arthritis & Rheumatism* 2001, **44**(4):846-855.
12. West PA, Bostrom MPG, Torzilli PA, Camacho NP: **Fourier Transform Infrared Spectral Analysis of Degenerative Cartilage: An Infrared Fiber Optic Probe and Imaging Study**. *Applied Spectroscopy* 2004, **58**(4).
13. West PA, Torzilli PA, Chen C, Lin P, Camacho NP: **Fourier transform infrared imaging spectroscopy analysis of collagenase induced cartilage degradation**. *Journal of Biomedical Optics* 2005, **10**(1):014015-014011-014016
14. Kozloff KM, Carden A, Bergwitz C, Forlino A, Uveges TE, Morris MD, Marini JC, Goldstein SA: **Brittle IV mouse model for osteogenesis imperfecta IV demonstrates postpubertal adaptations to improve whole bone strength**. *J Bone Miner Res* 2004, **19**(4):614-622.
15. Li B, Marshall D, Roe M, Aspden RM: **The electron microscope appearance of the subchondral bone plate in the human femoral head in osteoarthritis and osteoporosis**. *Jounal of Anatomy* 1999, **195**:101-110.
16. Petersson IF, Boegard T, Svensson B, Heinegard D, Saxne T: **Changes in cartilage and bone metabolism identified by serum markers in early osteoarthritis of the knee joint**. *British Journal of Rheumatology* 1998, **37**(1):46-50.

17. Saamanen A-MK, Salminen HJ, Dean PB, de Crombrugghe B, Vuorio EI, Metsaranta MPH: **Osteoarthritis-like lesions in transgenic mice harboring a small deletion mutation in type II collagen gene**. *Osteoarthritis and Cartilage* 2000, **8**:248-257.
18. Turner AS, Tippett JW, Powers BE, Dewell RD, Mallinckrodt CH: **Radiofrequency (electrosurgical) ablation of articular cartilage: a study in sheep**. *Arthroscopy* 1998, **14**(6):585-591.
19. Mier RJ, Holderbaum D, Ferguson R, Moskowitz R: **Osteoarthritis in children associated with a mutation in the type II procollagen gene (COL2A1)**. *Mol Genet Metab* 2001, **74**(3):338-341.
20. Salminen HJ, Saamanen AM, Vankemmelbeke MN, Auho PK, Perala MP, Vuorio EI: **Differential expression patterns of matrix metalloproteinases and their inhibitors during development of osteoarthritis in a transgenic mouse model**. *Ann Rheum Dis* 2002, **61**(7):591-597.
21. van der Sluijs JA, Geesink RG, van der Linden AJ, Bulstra SK, Kuyer R, Drukker J: **The reliability of the Mankin score for osteoarthritis**. *J Orthop Res* 1992, **10**(1):58-61.
22. Ostergaard K, Petersen J, Andersen CB, Bendtzen K, Salter DM: **Histologic/histochemical grading system for osteoarthritic articular cartilage: reproducibility and validity**. *Arthritis Rheum* 1997, **40**(10):1766-1771.
23. Carden A, Rajachar RM, Morris MD, Kohn D: **Ultrastructural changes accompanying the mechanical deformation of bone tissue: a Raman imaging study**. *Calcified Tissue International* 2003, **72**:166-172.
24. Tarnowski CP, Ignelzi MA, Morris MD: **Mineralization of Developing Mouse Calvaria as Revealed by Raman Microspectroscopy**. *Journal of Bone and Mineral Research* 2002, **17**(6):1118-1126.
25. Savontaus M, Metsaranta M, Vuorio E: **Retarded Skeletal Development in Transgenic Mice with a Type II Collagen Mutation**. *American Journal of Pathology* 1996, **149**(6):2169-2182.
26. Bailey AJ, Mansell JP, Sims TJ, Banse X: **Biochemical and mechanical properties of subchondral bone in osteoarthritis**. *Biorheology* 2004, **41**(3-4):349-358.
27. Akkus O, Adar F, Schaffler MB: **Age-related changes in physicochemical properties of mineral crystals are related to impaired mechanical function of cortical bone**. *Bone* 2004, **34**(3):443-453.
28. Busa B, Miller L, Rubin C, Qin YX, Judex S: **Rapid Establishment of Chemical and Mechanical Properties during Lamellar Bone Formation**. *Calcified Tissue International* 2005, **77**(6):386-394.
29. Mkukuma LD, Imrie CT, Skakle JMS, Hukins DWL, Aspden RM: **Thermal stability and structure of cancellous bone mineral from the femoral head of patients with osteoarthritis or osteoporosis**. *Ann Rheum Dis* 2005, **64**(2):222-225.
30. Day JS, van der Linden JC, Bank RA, Ding M, Hvid I, Sumner DR, Weinans H: **Adaptation of subchondral bone in osteoarthritis**. *Biorheology* 2004, **41**(3-4):359-368.

31. Timlin JA, Carden A, Morris MD, Rajachar RM, Kohn D: **Raman spectroscopic imaging markers for fatigue-related microdamage in bovine bone**. *Anal Chem* 2000, **72**:2229-2236.
32. David-Vaudey E, Burghardt A, Keshari K, Brouchet A, Ries M, Majumdar S: **Fourier-transform infrared imaging of focal lesions in human osteoarthritic cartilage**. *European Cells and Materials* 2005, **10**:51-60.
33. Brennan JF, Wang Y, Dasari RR, Feld MS: **Near-infrared Raman Spectrometer Systems for Human Tissue Studies**. *Applied Spectroscopy* 1997, **51**(2):201-208.
34. Bakker Schut TC, Witjes MJH, Sterenborg HJCM, Speelman OC, Roodenburg JLN, Marple ET, Bruining HA, Puppels GJ: **In Vivo Detection of Dysplastic Tissue by Raman Spectroscopy**. *Anal Chem* 2000, **72**(24):6010-6018.

Chapter 4

Correlating Changes in Collagen Secondary Structure with Aging and Defective Type II Collagen by Raman Spectroscopy

Introduction

Diagnosis and monitoring of collagen defects poses a challenge, especially for sub-clinical patients, since several inter-related biochemical, environmental and genetic factors may lead to collagen damage. Genetic and acquired abnormalities in types I, II, and IX collagen cause a range of skeletal diseases, such as early-onset osteoarthritis, Stickler's syndrome and osteogenesis imperfecta (OI). Type II collagen is a major component of articular cartilage and the vitreous humor of the eye. Known mutations of the type II collagen gene (COL2A1) in humans cause disorders, such as Stickler syndrome, that affects both the eye and skeletal systems.[1-3]

In addition to symptoms affecting bone or cartilage, patients with collagen diseases exhibit a range of ocular disorders including a discoloration of the sclera and an increased risk for detached retina, glaucoma and myopia.[4-6] Other genetic and acquired collagen disorders causing various eye pathologies are under investigation.[7] Moreover, eye collagen can be damaged as a result of natural aging, or age-related diseases such as macular degeneration affect the eye, likely causing changes in collagen structure.[8, 9]

Autoimmune and inflammatory disease can affect the eye, likely causing changes in collagen structure. Scleritis, for example, is a chronic destructive inflammation of the sclera which can lead to cataracts, glaucoma, and blindness. It is usually associated with systemic inflammatory disorders such as rheumatoid arthritis, Wegener's granulomatosis, polyarteritis nodosa, sarcoidosis, inflammatory bowel disease, or systemic infections such as syphilis or tuberculosis. The sclera is an avascular tissue made of dense fibrils of collagen, primarily types I and III, with smaller amounts of other collagen types, and interfibrillar leucine-rich proteoglycans and glycoproteins.[10] The episclera, which is superficial to the sclera, can also become inflamed, idiopathically or in association with inflammatory disorders such as rheumatoid arthritis, spondyloarthropathies or vasculitis. Sjogren’s syndrome, an inflammatory disorder causing decreased tear production, can occur on its own or in association with other inflammatory disorders such as systemic lupus erythematosis or rheumatoid arthritis. Sjogren’s syndrome can lead to damage and inflammation of the cornea. Anterior uveitis, also known as iritis or iridocyclitis, can be associated with juvenile rheumatoid arthritis or ankylosing spondylitis, both diseases of chronic arthritis. These inflammatory disorders of the eye often require prompt treatment, and can be difficult to diagnose.

In addition to being a model for early-onset OA, the Del1 (+/-) transgenic mouse can be systematically examined for ultrastructure changes in ocular tissue because of the role of type II collagen in the development of eye tissue and the limited availability of eye tissue from human patients of arthro-ophthalmopathies. Type II collagen polypeptide chains in the Del1 (+/-) transgenic mouse are truncated by 15 amino acids, which is a result of a 150 base pair deletion mutation in the COL2A1.[11] Because abnormal type II collagen is also expressed in vitreous, cornea and sclera, Del1 (+/-) transgenic mice exhibit ocular damage including early-onset liquefaction of the vitreous humor and reduction in vitreous fibrils.[12]

The effects of defective type II collagen formation are evident in musculoskeletal tissue from Del1 (+/-) transgenic mice.[13-15] Our previous study demonstrated that defective type II collagen in Del1 (+/-) transgenic mice leads to formation of subchondral bone with an apatite mineral with more carbonate substitution into the crystal lattice.[16] Subchondral bone in Del1 (+/-) transgenic mice is also less mineralized. The material properties of subchondral bone in Del1 (+/-) transgenic mice were altered on a chemical level, even though histopathology analysis did not provide an indication of gross morphological changes to the joint. We hypothesized that we would observe chemical changes in ocular tissue excised from Del1 (+/-) mice and these changes would be primarily observed as alterations in the collagen secondary structure.

Raman spectroscopy has been used to examine a variety of biological tissues.[17, 18] A Raman spectroscopy microprobe for alterations in protein structure is especially useful to distinguish normal and pathological tissues since subtle molecular changes often cause detectable vibrational changes. Properties of the Raman microprobe that make it an attractive method for direct analysis of biological tissues include high spatial resolution (0.25-0.5 μm for a 532 nm system, 0.5 -1.0 μm for a 785 nm system) and limited spectral interference from water. Since Raman spectra are recorded in the visible or near-infrared region, the optics are compatible with current clinical arthroscopy tools. Vibrational spectroscopy methods are used to characterize surface components of tissues or identify damage to tissues. FT-IR fiber optic probe and imaging methods have been used to investigate the contents of mineralized soft tissues.[19, 20] FT-IR studies have shown spectra to indicate collagen damage with prolonged exposure of articular cartilage to collagenase.[21] Raman studies of collagen fibers have identified fiber damage due to mechanical stress.[22]

Raman spectroscopy is an attractive tool to study ocular tissue because of the non-invasive and non-destructive nature of the technique and the accessibility of the eye. A single-channel resonance-enhanced Raman instrument quantifies macular pigments *in-vivo* in less than a minute, and has potential to track the progression of age-related macular degeneration.[23, 24] Identification of biological molecules and characterization of ocular surfaces by Raman spectroscopy have applications ranging from ophthalmologic disease diagnosis, monitoring effectiveness of treatments, to assessing compatibility of donated ocular tissue.[25, 26] Raman bands arising from spectra of the cornea and sclera are primarily due to contributions of type I collagen, and bands in the amide III region can estimate the relative polarity of type I collagen in rabbit and feline eyes.[27]

Eye tissue obtained during the study of wild-type and Del1 (+/-) transgenic mice subchondral bone on femoral condyles provided an opportunity for a preliminary study on the effects of defective type II collagen formation and aging on unmineralized ocular tissue. We used Raman spectroscopy to examine the sclera of eye tissue from Del1 (+/-) transgenic and wild-type mice. We observed changes in the area ratio of amide III bands, and band position of the 1235 cm^{-1} band in Raman spectra taken from the Del1 (+/-) transgenic and aged wild-type mice, reflecting an increase in the relative abundance in random coil secondary structure in eye collagen.

Materials and Methods

Animal Models

Breeding pairs of Del1 (+/-) transgenic mice were provided by Drs. E.I. Vuorio and A.-M. Säämänen at the University of Turku, Finland. Del1 (+/-) and wild-type mice were housed together under the same conditions. Del1 (+/-) transgenic and wild-type littermates mice were kept 1-5 per cage, allowed to ambulate *ad lib* and were given water and standard chow *ad lib*. Mice were sacrificed using anesthesia overdose, and the eye globe was enucleated *en masse*. Eye tissue from three mouse specimens, one 12-14 month old wild-type, one 12-14 month old Del1 (+/-) transgenic, and one 20 month old wild-type, were examined. Both eyes from each specimen were analyzed. Specimens 54 and 55 were 12-14 month Del1 (+/-) transgenic and wild-type mice. Specimen 13 was a 20 month old wild-type mouse. Eyes excised from mice at the time of sacrifice were stored in an ethanol solution at 4°C until time of Raman analysis. The diameter of the eye globes examined ranged from 2-4 mm.

Experimental Apparatus

Prior to spectroscopic examination, an eye was removed from the ethanol storage solution and lightly touched with a clean lab tissue to remove excess ethanol. The eye was allowed to equilibrate in pH 7.4 phosphate buffered saline (PBS) for 10 minutes. The eye mount was constructed in-house. The cap was removed from an unused, disposable 1.5 mL polypropylene micro-centrifuge tube (Fisher Scientific, Pittsburgh, PA), secured onto a microscope slide and filled with pH 7.4 phosphate buffered saline (PBS). A fresh cap was used for each eye globe to minimize cross-contamination, and was cleaned by a PBS rinse prior to use. The eye was then placed into the PBS-filled mount. The globe remained in PBS solution throughout the Raman experiments.

The Raman microprobe was constructed in-house and has been described in detail earlier.[28] Briefly, the Raman microprobe was equipped with a 785 nm Invictus line-focused laser (Kaiser Optical Systems, Ann Arbor MI). The laser was directed to an Olympus microscope, equipped with a 5X/0.25 NA objective. A 5X/0.25 NA objective and a 0.3 neutral density filter (laser intensity at objective ~105 mW) was used to avoid specimen burning and keep the entire specimen in focus, despite the small radius of curvature of the eye. Scattered light was collected by the objective and directed to a HoloSpec *f/1.8i* spectrometer that was equipped with a 25 μm slit for a spectral resolution of 4 cm^{-1} (Kaiser Optical Systems, Ann Arbor MI).The Raman signal was integrated for 10 minutes on a 1024X256 deep-depleted charged-coupled device (CCD) detector (Model DU420-BR-DD, Andor Technologies, Belfast, Ireland) optimized for collection of signal in the near-infrared. Specimens were analyzed with no coverslip over the mount. The volume of PBS in the mount was continually monitored and refreshed as needed. The outer edges of the sclera were examined. Raman transects, 254 point spectra taken at ~0.5 μm intervals along a line, were taken along these outer sclera edges. Spectra from transects with excessive fluorescence interference or specimen movement were discarded.

Analysis of Raman data

Depending on the specimen, spectra from five to twelve Raman transects were used to calculate a band area ratio. Andor MCD software was used as the data collection software. After data collection, transects were pre-processed in Matlab© using locally written or available scripts to remove curvature and spikes, and to remove the dark signal from the spectra. Band target entropy minimization (BTEM) was performed on select transects to confirm the presence of bands in the amide III envelope using locally written scripts in Matlab©.[29] To minimize the effect of sample heterogeneity on band area calculations, a single normalized spectrum (representative of the entire transect) was exported to GRAMS/AI© after the initial processing in Matlab©. Background signal from Raman spectra was removed using the baseline correction application, and bands in amide III envelope were fit using the curvefit application in GRAMS/AI© software. An example of the peak fitting routine, as applied to the amide III (1220-1280 cm^{-1}) and amide I (1640-1700 cm^{-1}) envelopes, is presented in Figure 4.1. Peak areas were recorded if the best-fit curve showed an R^2 greater than 0.990 and had no negative peaks.

Statistical Analysis

Band areas from spectra corresponding to a single specimen were grouped together to calculate a single average value for each band area. Ratios were calculated from averaged band areas. Student t-tests (two-sample, assuming unequal variances) were performed on the area and position of bands in the amide III envelope to determine statistical significance ($p<0.05$). Amide III band area ratio and band position comparisons were made between a) 12-14 month transgenic and wild-type mice, b) 12-14 month wild-type and 20 month wild-type mice, and c) 12-14 month transgenic and 20 month wild-type mice.

Chemicals

Phosphate buffered saline solution (0.01 M, pH 7.4) was prepared by dissolving a single tablet of phosphate buffered saline (Sigma-Aldrich, St. Louis, MO, part P-4417) in purified water according to the manufacturer's directions.

Results

A Raman spectrum of eye tissue is presented in Figure 4.1. A "blank" spectrum of the eye mount filled with PBS (spectrum not shown) confirmed that the spectral features of ocular tissue arose from the eye tissue, with minimal spectral interference from the mount. Minor spectral contributions, which are attributed to the phosphate buffer/polypropylene cap, were observed throughout these studies. An unusual, but consistent, finding was an enhanced band intensity of the amide III envelope. The amide III envelope is ~ 3 times more intense than the ring breathing mode at ~ 1002 cm^{-1}. Moreover, the localized maxima within the amide III envelope are less well-defined as compared to both Raman spectra of eye tissue found in the literature and in spectra taken of solid types I and II collagen in our laboratory (data not shown). We hypothesize that an unidentified fluorescence impurity, presumably from an eye pigment such as melanin, is overlapping with Raman scatter. The source of the fluorescence is not completely elucidated and, to date, we are unable to completely resolve the fluorescence background from the Raman signal using in-house data reduction routines. Band target entropy minimization (BTEM) and singular value decomposition (SVD) analysis of selected transects confirm the presence of a fluorescence impurity. As seen in Figure 4.2, applying singular value decomposition to Raman data reveal factors from eye collagen (Figure 4.2.b) and a fluorescence impurity (Figure 4.2.a). Without the interfering signal from the fluorescence impurity, the eye tissue Raman spectrum is more consistent in both shape and intensity with literature spectra of sclera collagen. However, it was not possible to apply SVD and BTEM to all transects because these routines require over-sampled data sets.

To verify the reliability of the curve-fitting routine, bands in the amide I envelope (1640-1720cm^{-1}) were also fit using the curve-fit application in GRAMS/AI$^{©}$. The relative intensity and band width of the amide I envelope was not affected by the fluorescence impurity that gave rise to the unusual band shape and intensity in the amide III envelope. The amide I band area ratio (area 1685 cm^{-1} band: area 1667 cm^{-1} band) was compared to the amide III ratio for each of the specimens. Due to the lower quantum efficiency of the CCD in the 1600-1720cm^{-1} region, it was not possible to obtain band area ratios in the amide I envelope for all of the transects. At least three transects from each specimen were used to calculate the amide I band area ratio.

Analysis of fitted bands in the amide III envelope was used to estimate the relative content of random coil secondary structure in ocular collagen. The amide III envelope reflects both ordered protein secondary structure such as α-helix or β-sheet, and disordered secondary structure, such as random coil. The amide III envelope is observed as a broad feature in the Raman spectra of proteins and tissues. Two maxima are typically observed within the envelope. The wavenumber maximum at a lower Raman shift (range: 1230-1240 cm^{-1}) is indicative of random coil content in the protein's secondary structure, and the maximum at a higher Raman shift (range: 1260-1270 cm^{-1}) is indicative of α-helix content in the protein secondary structure.[30] For eye tissue, the maxima were 1235 cm^{-1} and 1265 cm^{-1} and we define the amide III ratio as the ratio of the 1235 cm^{-1} and 1265 cm^{-1} band areas. Increases in the amide III ratio indicate an increase in the disorder of the collagen fiber. Band assignments are provided in Table 4.1 and are based on previous assignments of ocular tissue from the literature.[26, 31] Local maxima in the amide III envelope are less defined in ocular tissue than in articular cartilage likely due to several types of collagen structure in the ocular tissue.[32] Figure 4.3 is a comparison of Raman spectra of subchondral bone and eye cartilage taken from the same specimen. Contributions from phosphate and carbonate mineral components showed strong bands at 959 cm^{-1} and 1070 cm^{-1} in spectra from subchondral bone, and these bands were not observed in Raman spectra taken from eye tissue.

Discussion

Raman spectra of eye tissue from the Del1 (+/-) transgenic mouse showed an increase in the relative abundance of disordered secondary structure in the collagen fiber that was also observed in the aged wild-type mouse. As shown in Table 4.2, spectra taken from 12-14 month old transgenic and 20 month old wild-type mice have a higher amide III band area ratio. Increases in the amide III band area ratio reflect more disordered collagen secondary structure in ocular tissue. In the analysis of ocular tissue, there was an observable difference of amide III band area ratios corresponding to the 12-14 month transgenic and age-matched wild-type mice (specimen ID 54 and 55, respectively). The amide III band area ratio of transects taken from the 20 month wild-type mouse is comparable to that of the 12-14 month transgenic mouse, indicating that collagen damage caused by the COL2A1 transgene at age 12-14 months may be comparable to 20 months of the normal aging as seen in the older wild-type mouse. The amide III band area ratio of the aging wild-type mice (12-14 month old versus 20 month old) shows an increase in the amide III band area ratios, indicating that increase to the disorder of the secondary structure of collagen in older wild-type mice occurs as a natural result of aging and the low turnover rate of ocular collagen. An increase in disorder of collagen secondary structure as a function of age in wild-type mice is expected. A slight increase in the amide III band area ratio was also observed in Raman analysis of femurs from aging wild-type mice.

In addition to a higher amide III band area ratio, the average peak position of fitted bands in the amide III envelope provides another indication of collagen damage in the 12-14 month Del1 (+/-) transgenic and 20 month wild-type specimens. We observed a shift to a higher wavenumber for the 1235 cm^{-1} peak for the 20 month wild-type and transgenic mouse and is thus dependent on both the age and transgenic status of the mouse. Spectra from the 12-14 month transgenic and 20 month wild-type mouse have an average peak position of 1234 cm^{-1} (±2) and 1236 cm^{-1} (±2) respectively, while spectra from the 12-14 month wild-type mouse have an average peak position of 1231 cm^{-1} (± 1). The band position seen in both the 12-14 month transgenic and 20 month wild-type is statistically different ($p<0.05$) from the 12-14 month wild-type mouse.

Raman spectroscopy of proteins has shown that changes in the secondary structure, due to environmental, mechanical, or chemical stresses, will be reflected in the amide III and amide I envelopes. These alterations may be observed as changes in band position, band area ratio, or band intensity ratio. Eye collagen is not subject to mechanical loading that occurs in musculoskeletal tissue. We conclude that the observed shifts in amide III band position resulted from chemical modifications. Our results suggest that the COL2A1 gene altered collagen cross-linking which led to an increase in the relative abundance of disordered collagen secondary structure. Shifts in the fitted amide III bands in spectra from 20 month wild-type and 12-14 month Del1 (+/-) transgenic mice to higher wavenumbers, relative to the 12-14 month wild-type, may be interpreted as increased compression of amide groups along the collagen backbone.

Because we observed a fluorescence impurity that overlapped with Raman signal in the amide III envelope, the amide I band area ratio was used to confirm the reliability of the curve-fit routine for amide III bands. We compared the value of the amide I and amide III band area ratios of transects taken from eye tissue with transects taken from articular cartilage from mice of comparable ages (12, 13, and 20 months) and transgenic status.

The value of the amide III band ratio relative to the amide I band area ratio was expected to remain consistent, regardless of the type of tissue examined. In transects taken from both eye tissue and articular cartilage, the amide III band area ratio was ~ 2 times larger than the amide I band area ratio, indicating reliable band-fit for both the amide I and amide III envelopes.

Conclusions

The initial results of applying Raman spectroscopy to the study of ocular tissue from Del1 (+/-) and aging wild-type mice are promising. There is a statistically significant difference in the amide III band ratios between the 12-14 month transgenic and wild-type mice. The transgenic mouse showed a higher collagen disorder, as expected, compared to its age-matched wild-type littermate. Moreover, the increased collagen disorder in the 20 month wild-type mouse indicates that Raman can also identify changes to collagen that are a result of normal aging. Truncation of the collagen fiber caused by the transgene or loss of collagen fiber elasticity from normal aging could be causes of the spectroscopic changes that are observed in both the amide III band area ratio and band position associated with disordered collagen in the amide III region. These data support and extend our earlier observations that Raman spectroscopy is able to identify increased collagen disorder in both transgenic mice and older wild-type mice. Raman bands in the amide III envelope can be used to identify and possibly quantify disorder in the secondary structure of the collagen protein in eye tissue. Despite the spectral interference in the amide III envelope from a fluorescence impurity, the curve-fit routine in GRAMS/AI$^{©}$ provides reliable calculation of band areas within the amide III envelope. A detailed study of transgenic and wild-type mice at several defined time points is necessary to fully evaluate the effect of the transgene and aging. Because it is non-invasively accessible, eye tissue may serve as a good site for study of collagen damage due to acquired or genetic defects, inflammatory disorders, or the natural aging process.

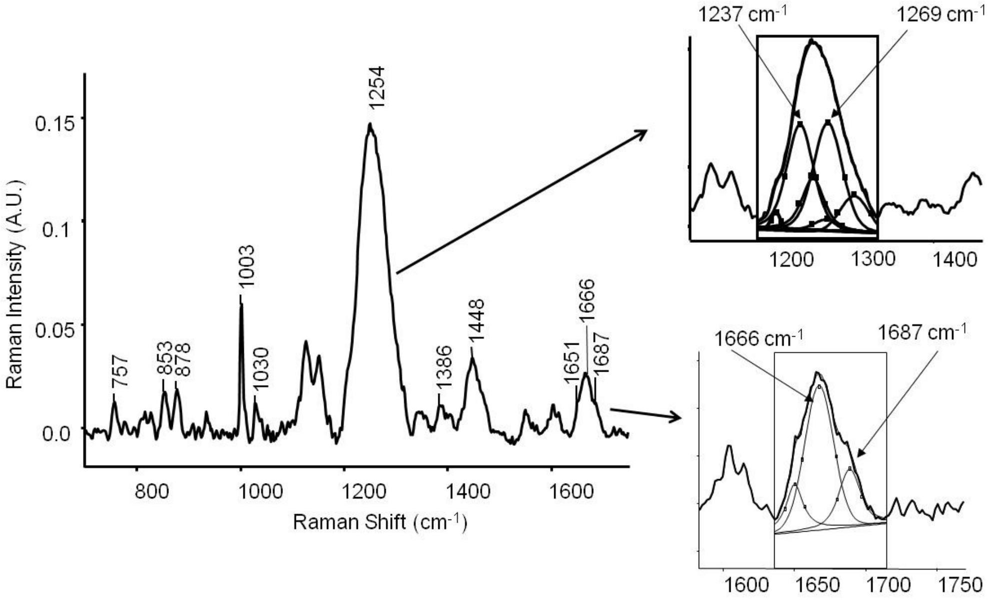

Figure 4.1: Raman spectrum of eye tissue and curve-fit of amide III envelope. A baseline corrected Raman spectrum on the left shows subtle bands more clearly. Panels on the right are examples of the curve-fit routine run in GRAMS/AI© software.

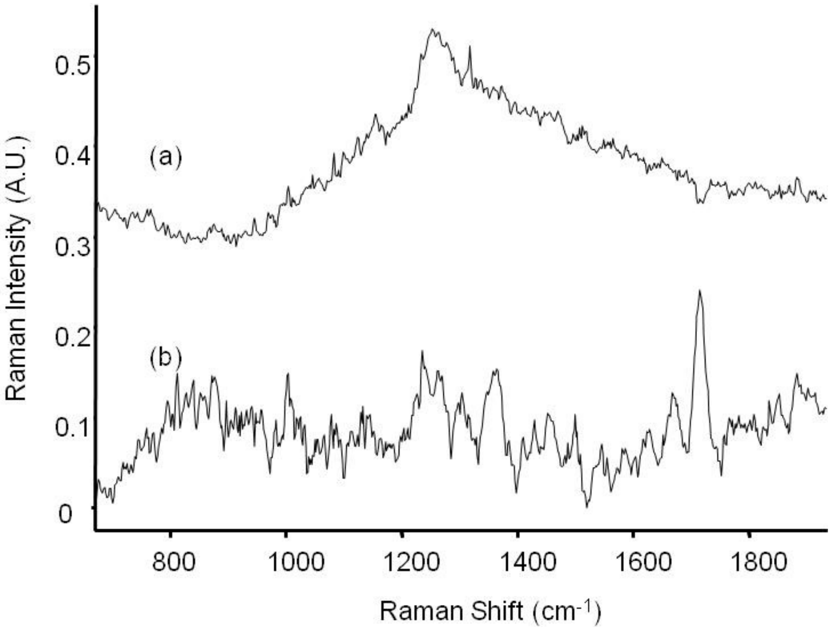

Figure 4.2: Singular value decomposition (SVD) analysis of a Raman transect taken from eye tissue of a 12-14 month Del1 (+/-) transgenic mouse. The same transect that is represented in Figure 4.1 was also analyzed by SVD. There were two main non-noise factors. The fluorescence impurity (a) factor clearly overlaps with the amide III envelope. The eye tissue factor (b) is consistent with Raman literature spectra of eye sclera and dry samples of types I and II collagen.

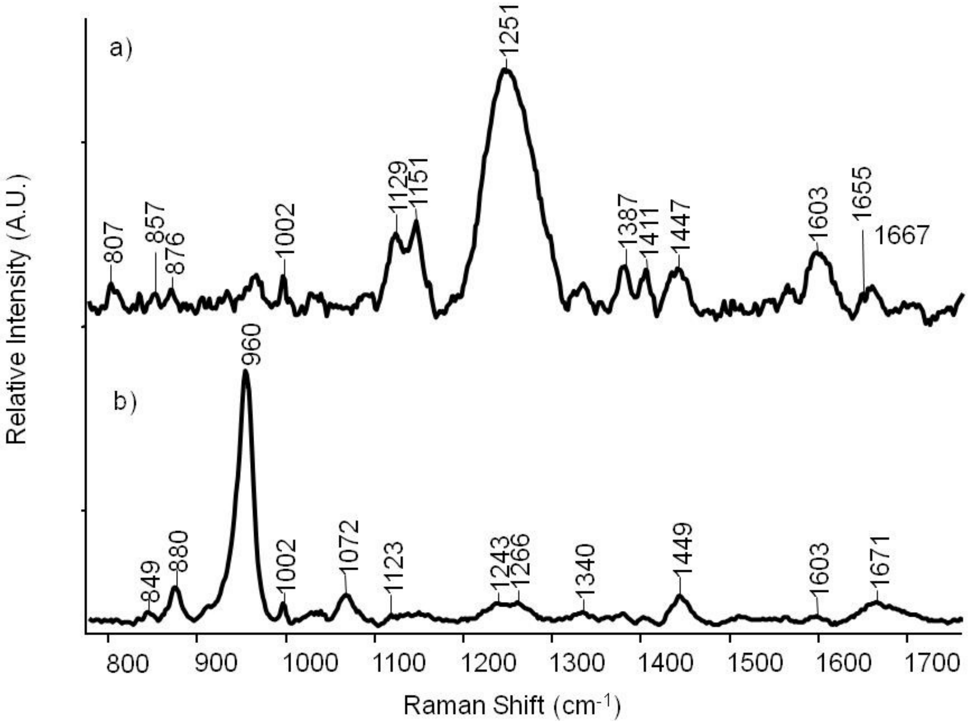

Figure 4.3: A comparison of a spectrum from subchondral bone versus ocular tissue. Raman spectra were taken from the (a) eye and (b) femur of the 20 month wild type mouse and show Raman bands that arise from components characteristic to the tissue.

Raman Band Position (cm^{-1})	Assignment	Component
642, 757, 827, 853, 877	757: ν (C-C-O), 853: ν (C-C-H) aromatic, 877: ν (C-C)	Aromatic protein residues
1003	ν (C-C) aromatic ring	Aromatic ring breathing
1220-1280	1235: δ (NH_2) random coil 1265: δ (NH_2) alpha-helix	Amide III
1450	δ (C-H)	Protein CH_2, CH_3 scissor
1650	O-H bend	Amide I, H_2O
1667	□ (C=O) alpha-helix	Amide I
1685	ν (C=O)	Amide I

Table 4.1: Assignments for observed Raman bands of ocular tissue based on literature reports and our studies of unmineralized articular cartilage.

Mouse transgenic status and age	Band position, random coil collagen (cm^{-1})	Band position, α-helix collagen (cm^{-1})	Amide III band area ratio
Wild-type, 12-14 months	1231 ± 1	1265 ± 4	0.552
Wild-type, 20 months	1234 ± 2	1265 ± 3	0.965
Del1 (+/-) transgenic, 12-14 months	1236 ± 2	1264 ± 2	0.881

Table 4.2: Comparison of band positions in amide III envelope and amide III band area ratios for all specimens. The ± value represents the 95% confidence limit. Increases in the amide III ratio indicate an increase in the disorder of the collagen fiber.

References

1. McLeod D, Black GC, Bishop PN: **Vitreous phenotype:genotype correlation in Stickler syndrome**. *Graefe's Archive for Clinical and Experimental Ophthalmology* 2002, **241**(1):63-65.
2. Donoso LA, Edwards AO, Frost AT, Ritter IIIR, Ahmad N, Vrabec T, Rogers J, Meyer D, Parma S: **Clinical Variability of Stickler Syndrome: Role of Exon 2 of the Collagen COL2A1 Gene**. *Survey of Ophthalmology* 2003, **48**(2):191-203.
3. Poulson AV, Hooymans JMM, Richards AJ, Bearcroft P, Murthy R, Baguley DM, Scott JD, Snead MP: **Clinical Features of Type 2 Stickler Syndrome**. *Journal of Medical Genetics* 2004, **41**(8):e107-e113.
4. Roughley PJ, Rauch F, Glorieux FH: **Osteogenesis Imperfecta-Clinical and Molecular Diversity**. *European Cells and Materials* 2003, **5**:41-47.
5. Sebes JI, Kasthuri S: **Hereditary artho-ophthalmopathy (Stickler syndrome)**. *Skeletal Radiology* 2000, **29**:613-619.
6. Ihanamaki T, Pelliniemi LJLJ, Vuorio E: **Collagens and collagen-related matrix components in the human and mouse eye**. *Progress in Retinal and Eye Research* 2004, **23**(4):403-434.
7. Petrich W: **Mid-Infrared and Raman Spectroscopy for Medical Diagnostics**. *Applied Spectroscopy Reviews* 2001, **36**(2&3):181-237.
8. Bhutto IA, Kim SY, McLeod DS, Merges C, Fukai N, Olsen BR, Lutty GA: **Localization of Collagen XVIII and the Endostatin Portion of Collagen XVIII in Aged Human Control Eyes and Eyes with Age-Related Macular Degeneration**. *Invest Ophthalmol Vis Sci* 2004, **45**(5):1544-1552.
9. Hayward C, Shu X, Cideciyan AV, Lennon A, Barran P, Zareparsi S, Sawyer L, Hendry G, Dhillon B, Milam AH *et al*: **Mutation in a Short-chain Collagen Gene, CTRP5, Results in Extracellular Deposit Formation in Late-onset Retinal Degeneration: A Genetic Model for Age-related Macular Degeneration.** . *Human Molecular Genetics* 2003, **12**(20):2657-2667.
10. Watson PG, Young RD: **Scleral structure, organisation and disease. A review**. *Experimental Eye Research* 2004, **78**(3):609-623.
11. Helminen HJ, Saamanen A-M, Salminen H, Hyttinen MM: **Transgenic mouse models for studying the role of cartilage macromolecules in osteoarthritis**. *Rheumatology* 2002, **41**:848-856.
12. Ihanamaki T, Salminen H, Saamanen A-M, Sandberg-Lall M, Vuorio E, Pelliniemi LJ: **Ultrastructure characterization of developmental and degenerative vitreo-retinal changes in the eyes of transgenic mice with a deletion mutation in type II collagen gene**. *Current Eye Research* 2002, **24**(6):439-450.
13. Hyttinen MM, Toyras J, Lapvetelainen T, Lindblom J, Prockop DJ, Li SW, Arita M, Jurvelin JS, Helminen HJ: **Inactivation of one allele of the type II collagen gene alters the collagen network in murine articular cartilage and makes cartilage softer**. 2001, **60**(3):262.
14. Metsaranta M, Garofalo S, Decker G, Rintala M, de Crombrugghe B, Vuorio E: **Chondrodysplasia in Transgenice Mice Harboring a 15-Amino Acid Deletion**

in the Triple Helical Domain of Proa1(II) Collagen Chain. *The Journal of Cell Biology* 1992, **118**(1):203-212.

15. Savontaus M, Metsaranta M, Vuorio E: **Retarded Skeletal Development in Transgenic Mice with a Type II Collagen Mutation**. *American Journal of Pathology* 1996, **149**(6):2169-2182.
16. Dehring KA, Crane NJ, Smukler AR, McHugh JB, Roessler BJ, Morris MD: **Identifying Chemical Changes in Subchondral Bone Taken from Murine Knee Joints Using Raman Spectroscopy**. *Applied Spectroscopy* 2006, **60**(10):1134-1141.
17. Mahadevan-Jansen A: **Raman Spectroscopy: From Benchtop to Bedside**. In: *Biomedical Photonics Handbook.* Edited by Vo-Dinh T. Boca Raton: CRC Press; 2003.
18. Puppels GJ: **In Vivo Raman Spectroscopy**. In: *Handbook of Raman Spectroscopy: From the Research Laboratory to the Process Line.* Edited by Lewis IR, Edwards HGM. New York: Marcel Dekker; 2001.
19. Camacho NP, West P, Torzilli PA, Mendelsohn R: **FTIR microscopic imaging of collagen and proteoglycan in bovine cartilage**. *Biopolymers* 2001, **62**(1):1-8.
20. West PA, Bostrom MPG, Torzilli PA, Camacho NP: **Fourier Transform Infrared Spectral Analysis of Degenerative Cartilage: An Infrared Fiber Optic Probe and Imaging Study**. *Applied Spectroscopy* 2004, **58**(4).
21. West PA, Torzilli PA, Chen C, Lin P, Camacho NP: **Fourier transform infrared imaging spectroscopy analysis of collagenase induced cartilage degradation**. *Journal of Biomedical Optics* 2005, **10**(1):014015-014011-014016
22. Wang YN, Galiotis C, Bader DL: **Determination of molecular changes in soft tissues under strain using laser Raman microscopy**. *Journal of Biomechanics* 2000, **33**(4):483-486.
23. Ermakov IV, Ermakov MR, Gellermann W: **Simple Raman Instrument for in Vivo Detection of Macular Pigments**. *Applied Spectroscopy* 2005, **59**(7).
24. Ermakov IV, Ermakov MR, Gellermann W, Bernstein PS: **Macular pigment Raman detector for clinical applications**. *Journal of Biomedical Optics* 2004, **9**(1):139-148.
25. Erckens RJ, Motamedi M, March WF, Wicksted JP: **Raman Spectroscopy for Non-Invasive Characterization of Ocular Tissue: Potential for Detection of Biological Molecules**. *Journal Of Raman Spectroscopy* 1997, **28**:293-299.
26. Jongsma FHM, Erckens RJ, Wicksted JP, Bauer NJC, Hendrikse F, March WF, Motamedi M: **Confocal Raman spectroscopy system for noncontact scanning of ocular tissues: an in vitro study**. *Optical Engineering* 1997, **36**(11):3193-3199.
27. Mizuno A, Tsuji M, Fujii K, Kawauchi K, Ozaki Y: **Near-infrared Fourier transform Raman spectroscopic study of cornea and sclera**. *Japanese Journal of Ophthalmology* 1994, **38**:44-48.
28. Timlin JA, Carden A, Morris MD, Rajachar RM, Kohn D: **Raman spectroscopic imaging markers for fatigue-related microdamage in bovine bone**. *Anal Chem* 2000, **72**:2229-2236.

29. Widjaja E, Li C, Chew W, Garland M: **Band-Target Entropy Minimization. A Robust Algorithm for Pure Component Spectral Recovery. Application to Complex Randomized Mixtures of Six Components**. *Anal Chem* 2003, **75**:4499-4507.
30. Chi Z, Chen XG, Holtz JSW, Asher SA: **UV Resonance Raman-Selective Amide Vibrational Enhancement: Quantitative Methodology for Determining Protein Secondary Structure**. *Biochemistry* 1998, **37**:2854-2864.
31. Carter EA, Edwards HGM: **Biological Applications of Raman Spectroscopy**. In: *Infrared and Raman Spectroscopy of Biological Materials.* Edited by Gremlich H-U, B.Yan. New York: Marcel Dekker Inc; 2001.
32. Meek KM, Fullwood NJ: **Corneal and scleral collagens-a microscopist's perspective (review)**. *Micron* 2001, **32**:261-272.

Chapter 5

Arthroscopic Raman Spectroscopy

Introduction

Arthroscopy is a minimally invasive surgical technique that is commonly used to treat or repair joint tissues. Arthroscopic techniques are commonly used in the diagnosis and treatment osteoarthritic joints.[1, 2] Features such as roughened cartilage, focal lesions on the cartilage surface (1-3 mm) or osteophytes can be readily visualized through an arthroscope, and the instrument can be used to guide arthroscopic surgery. An arthroscope is a probe with a long narrow rod-shaped portion ending in an optical port at the tip. The rod portion is typically 2-3 mm diameter, so that the arthroscope can be inserted into a joint space through a small incision. A video camera is attached to the proximal end of the arthroscope and enables visualization of the joint *in situ*. The primary benefit of arthroscopic surgery is the small incision, which reduces infection risk and patient recovery time.

The surgical terms used in the next two paragraphs are defined below.

> Lavage: Lavage is a process in which the joint is rinsed with a buffered solution and has been shown to reduce short-term joint pain because inflammatory proteins are irrigated out of the joint.
>
> Shaving: Shaving of fibrillated cartilage surfaces or smoothing cartilage near focal lesions, using a mechanical cutting instrument, reduces friction in joints affected by osteoarthritis.
>
> Debridément: Debridément is a more intensive form of shaving, where osteophytes are removed in addition to damaged cartilage. Debridément can provide long-term pain relief (12-24 months), especially in patients with mild or moderate osteoarthritis.[2]

Laser reshaping: Using a high intensity excimer laser to reshape cartilage is an alternative to a mechanical cutter. Laser reshaping of cartilage provides better spatial resolution and is less destructive than a mechanical cutter.

Several methods are used in arthroscopic surgery for treating osteoarthritis. Cartilage reshaping and lavage techniques provide short-term pain relief, especially for patients with mild or moderate osteoarthritis. The long-term efficacy of these techniques is still a topic of research, primarily because they do not repair damaged cartilage. Equally important, lavage and cartilage reshaping may potentially induce chondrocytes necrosis or remove healthy chondrocytes in addition to damaged cartilage.

During therapeutic arthroscopic procedures it is critical that healthy and damaged tissue be identified. Current methods rely primarily on visual inspection of joint surfaces to identify damaged cartilage and osteophytes. Visual inspection does not provide complete identification of the tissue health. As a result, healthy cartilage is sometimes removed and lesions can only be identified in the superficial cartilage zone. Improved discrimination between healthy and diseased cartilage, and identification of subsurface focal lesions during arthroscopic joint surgery would improve treatment efficacy because healthy areas could be preserved and damaged sites would be better identified and treated. For this reason, there is interest in both clinical and basic science research to couple arthroscopy with techniques that can rapidly identify damaged cartilage tissue or microfracture sites and identification of appropriate shaving, debridément or laser shaping .[2]

Spectroscopy and hyperspectral imaging of cartilage and subchondral bone during arthroscopy can provide contrast to show molecular signatures of damage, even if it is invisible to the eye. Alterations to the molecular structure of cartilage extracellular matrix and subchondral bone are among the earliest signs of osteoarthritic lesion formation.[3-5] In cartilage the primary molecular alterations include loss of proteoglycan content and disorganization of type II collagen fibrils.[5-8] In addition, there is a decrease in mineralization of subchondral bone which also becomes stiffer as a result of increased carbonate ion substitution into the apatite crystal lattice.[4, 9-12] Decreases in proteoglycan content or increased type II collagen birefringence have been observed in examination of cartilage by Fourier-transform infrared (IR) spectroscopy and optical coherence tomography (OCT).[3, 13-15]

Spectroscopic techniques can be adapted for use with fiber-optic probes, rendering them compatible with the small dimensions of an arthroscopic instrument. Fiber-optic FT-IR and OCT techniques have been used to examine articular cartilage. Use of a fiber-optic probe for examination of cartilage by FT-IR was demonstrated in 2004 by West et al.[16] This study showed proof-of-concept for collection of cartilage spectra in an infrared fiber-optic probe. A meter-long fiber-optic bundle was coupled to an attenuated total reflectance crystal and the probe was put in direct contact with articular cartilage. Spectral results from the FT-IR fiber-optic probe were validated against FT-IR microscopy of the cartilage specimens and Collins visual grading of cartilage damage. Both the fiber-optic probe and microscope measurements detected subtle but significant differences in established infrared markers of collagen damage between mildly and severely degraded cartilages. In another study, fiber-optic polarized OCT was adapted for arthroscopy.[17] OCT measurements on full-depth (~ 2mm) porcine articular cartilage before and after surgical incision revealed incision-induced alterations to type II collagen orientation.

We report the adaptation of Raman spectroscopy for arthroscopic measurements. Two configurations were explored. In the first configuration, a commercially-available arthroscope was coupled to a fiber-optic Raman spectroscopy detector. In the second configuration, a fiber-optic probe was tested where excitation and collection fiber-optics were coupled through a stainless steel tube with arthroscope dimensions. The second probe configuration was used to collect Raman signal of cadaveric human joint tissue at the proximal radius. Tissue optical scattering and absorption determine the optically sampled tissue volume, and thus the Raman spectra collected from cartilage and subsurface tissue. The effects of optical properties on arthroscopic tissue measurements are discussed.

Materials and Methods

Raman Spectroscopy Microscope

A Nikon E600 epi-fluorescence microscope (Nikon Inc., Melville, NY, USA) was modified for NIR Raman spectroscopy in-house. Microscope images were collected in epi-illumination mode with 4x/0.20NA, 10x/0.50NA, and 20x/0.75NA S Fluor objectives (Nikon Inc., Melville, NY, USA). A 785 nm Kaiser Invictus laser was line focused (Kaiser Optical Systems Inc., Ann Arbor, MI, USA) onto the specimen using a 20x/0.75NA S Fluor objective. A neutral density filter of 0.3 reduced the laser intensity at the objective to ~ 10 mW. Raman-scattered light was collected through the same 20x/0.75 NA S Fluor objective and dispersed through a spectrograph (HoloSpec f/1.8, Kaiser Optical Systems Inc., Ann Arbor, MI, USA). Raman signal was collected for 10 minutes on a deep-depletion, back-thinned 1024x128 charge-coupled device (CCD) detector (DU401-BR-DD, Andor Technologies, Belfast, Ireland). Raman transects consisted of 126 Raman spectra arranged at equidistant points along a line through the specimen.

Raman Fiber-optic Probes

Two arthroscopic-compatible Raman fiber-optic probe configurations were tested. In the first configuration a commercially-available arthroscope was coupled to a fiber-optic probe, as shown in Figure 5.1. A 785 nm laser beam (Invictus, Kaiser Optical Systems, Inc., Ann Arbor, MI, USA) was focused into a 62.5 µm core fiber-optic. The beam was collimated and focused into the center optical channel of an arthroscope (Stryker, San Jose, CA, USA). The laser intensity at the end of the arthroscope was 10-15 mW, and the beam size was less than 1 mm. Raman scatter was collected above the side channel of the arthroscope using a fiber-optic probe with 50 collection fibers, arranged in a circle, and fitted with a 75 mm diverging lens (PhAT probe, Kaiser Optical Systems, Inc., Ann Arbor, MI, USA). Raman scatter collected by the PhAT probe was dispersed through a spectrograph (HoloSpec, Kaiser Optical Systems, Inc., Ann Arbor, MI, USA) and imaged onto a 1024x256 back-thinned deep-depletion charge-coupled device (CCD) detector (Andor Technologies, Belfast, N. Ireland). Raman spectra from a bovine bone specimen were collected for 10 minutes.

In the second configuration, Raman fiber-optics were coupled through a stainless steel tube with outer diameter of 2 mm (smaller outer diameter than the commercial arthroscope probe). An 830 nm laser (Invictus, Kaiser Optical Systems, Inc., Ann Arbor, MI, USA) was focused onto an excitation bundle of 15 optical fibers each with a 200 μm core and each enclosed in a Tefzel jacket (FiberTech Optica, Inc., Kitchener, Canada). The excitation bundle was bifurcated into 15 individual branches, each consisting of one coated fiber with a steel hypodermic tubing termination. Two excitation fibers were separated from the rest of the bundle to be used in the arthroscope and the other 13 fibers were covered. The two excitation fiber provided approximately 100mW of excitation laser power. The collection bundle was similar in design to the excitation bundle, with 50 individual fibers of 100 μm core diameter and Tefzel jacketing. On one end of the bundle the fibers were arranged linearly for coupling to the spectrograph, and on the other end the individual fibers were enclosed in hypodermic tubing and the ends polished. Ten collection fibers were placed around the 2 excitation fibers and fed into the stainless steel tube so that they were flush with the end of the tube. Raman scatter was dispersed through a spectrograph and collected onto a 1024x256 CCD detector (RamanRxn1, Kaiser Optical Systems, Ann Arbor, MI, USA).

Raman Data Preprocessing

Raman data were preprocessed in Matlab (v7, The Math Works, Natick MA, USA) using software routines developed in-house. Spectra from a neon discharge source were used to calibrate the wavelength axis, spectra from a quartz-halogen source were used to correct for variations in CCD response and standardized using a NIST-traceable intensity calibration. Dark spectra were used to correct for detector noise. Data were imported into Matlab using software developed in-house where they were corrected for cosmic ray spikes, dark current and variations in the CCD camera efficiency. Corrections for slit image curvature and tilt of the CCD relative to the spectrograph were handled using software routines developed in-house.[18] For the fiber-optic probes, multiple (10) accumulations of short acquisition spectra were collected. A mean image was calculated from the multiple accumulations, however to remove spurious signals from cosmic rays, some pixels were excluded from this mean. To determine which pixels to exclude, the 10 pixels from every x-y point in the 10 accumulation images were examined. A median and standard deviation was calculated, and only pixel intensities within 3 times the standard deviation of the median value were used in calculating the mean image. From the cosmic ray corrected mean image, spectra associated with each individual collection fiber-optic were calculated. The spatial distribution of intensity from each collection fiber on the detector was mapped with broadband illumination and the normalized broadband profiles for the collection fibers were used to calculate the contributions from each individual fiber to the measured spectral image. Silica contributions to the measured spectra are significant with the long and unfiltered fiber-optics. Silica contributions were measured by reflecting the excitation laser from a roughened aluminum surface, and removed from the measured data using a derivative subtraction of the measured silica spectra.

Raman Data Processing

Mean spectra for each transect were calculated and baseline corrected in Matlab. Baseline-corrected mean spectra were imported into GRAMS/AI© software (ThermoGalactic Salem NH, USA). Raman bands in baseline-corrected spectra were fitted to mixed Lorentzian/Gaussian peaks to obtain band width, height and area parameters. The resulting fit was accepted if the $R^2>0.99$ and no negative bands were generated. The bands generated by the curvefit application were identified as carbonated apatite mineral and type I collagen in subchondral bone spectra or carbonated apatite mineral and lipids in cancellous bone spectra. Table 5.1 shows band assignments for cancellous bone based on literature reports.[19-21] Band assignments for subchondral bone are presented in Table 3.1, and band assignments for articular cartilage extracellular matrix molecules are presented in Table 1.2. Raman band intensity ratios were used as markers of bone mineralization, mineral to matrix ratio (MTMR, 958 cm^{-1}/(850 cm^{-1}+876 cm^{-1})), and extent of carbonate substitution into the apatite lattice (carbonate-to-phosphate, 1070 cm^{-1}/958 cm^{-1}) or protein secondary structure (amide III, 1245 cm^{-1}/1268 cm^{-1}).

Human Proximal Radius Tissue Specimen

A human arm specimen was acquired from the University of Michigan anatomical donations program. An approximately 1 cm section of human proximal radius, including the articular cartilage, was removed from a cadaveric arm specimen, for use in another experiment. Immediately after dissection, the proximal radius specimen was stored in phosphate buffered saline (PBS) at 4°C until examination. The specimen was examined within 3 days of dissection. Prior to examination by Raman spectroscopy, the specimen was placed onto a gauze pad, moistened with fresh PBS, and positioned on top of a gold-coated glass slide (EMF Corporation, Ithaca, NY, USA). Cortical bone in the subchondral bone plate was first examined on the Raman microscope under an intact layer of cartilage. Articular cartilage was then removed with a fresh scalpel and spectra were collected from the exposed subchondral bone. After turning the specimen over, cancellous bone underlying the subchondral bone plate was examined. Articular surface with intact cartilage and cancellous bone were examined using the fiber-optic arthroscope.

Results

As a proof-of-concept for coupling Raman measurements through an arthroscope, we examined bovine cortical bone and human ex vivo tissue from the proximal radius. In the first experiment, bovine bone was examined to determine whether it was feasible to measure bone Raman signal through an arthroscope. The Raman spectrum of bovine cortical bone collected in this way is shown in Figure 5.2. In this spectrum the phosphate ν_1 at 958 cm^{-1} and carbonate ν_2 at 1068 cm^{-1} were easily observed. In order to detect bone signal at an appreciable signal to noise level, a single accumulation of 10 minutes was adequate.

In the second experiment, tissue excised from a human proximal radius was examined directly with a prototype arthroscope to determine the feasibility of measuring cartilage, subchondral bone, and cancellous bone spectra. Raman spectra collected through the fiber-optic probe are shown in Figure 5.3. For validation of the fiber-optic measurements, the same tissue regions were examined using a Raman microscope. Spectra collected on the Raman microscope are shown in Figure 5.4. Raman spectra collected from articular surface (with the cartilage intact) were predominately type II collagen protein and sulfated glycosaminoglycan bands with minor spectral contributions from the underlying subchondral bone. Spectra collected from the articular surface after removal of the cartilage layer revealed mineral bands at 959 cm^{-1} and 1073 cm^{-1} in addition to collagen matrix bands. Raman spectra from cancellous bone contain bands from both the carbonated apatite mineral and lipids. Bands at 1300 cm^{-1} and 1744 cm^{-1} are unique to lipids and were attributed to marrow lipids because they were not observed in cartilage or subchondral bone spectra.

Band intensity ratios calculated from proximal radius spectra collected from the fiber-optic arthroscope were compared against ratios calculated from proximal radius spectra collected from the Raman microscope. Mineral to matrix and carbonate to phosphate band intensity ratios calculated from these measurements are listed in Table 5.2.

Discussion

Arthroscopic surgery is widely used to remove damaged cartilage from patients with osteoarthritic joints. Enhanced contrast from Raman spectroscopy has the potential to improve identification of damaged cartilage and guide surgical intervention towards better outcomes. Raman measurements coupled through an arthroscope have been demonstrated using a human cadervic proximal radius specimen. These initial results are promising because we were able to observe Raman bands unique to subchondral bone and cancellous bone. Raman band intensity ratios calculated from spectra collected from the fiber-optic arthroscope compare favorably with microscope measurements of the same tissue.

Differences in the spectra collected with the microscope and fiber-optic probe arise because of the optical volumes sampled. The Raman microscope operates in a quasi-confocal geometry to maximize signal collection. In spectra taken with the Raman microscope of the articular surface, we found only minor spectral contributions from subchondral bone when the cartilage layer was intact. This result was expected, given that the scattering efficiency of bone is higher than cartilage. Spectra collected from the articular surface of the proximal radius using the fiber-optic probe contained strong spectral contributions from subchondral bone and lipid. Lipid signal was not detected in microscopy of the articular surface. Although lipids are present in fresh tissue, lipids are not present on the articular surface in large quantities. However, we expected to observe contributions from lipids in the fiber-optic measurements of the articular surface because the fiber-optic system samples a larger spatial volume, and hence also returns signal from the underlying lipid-containing marrow space. Strong lipid contributions were also found in spectra of cancellous bone measured with both the microscope and fiber-optic probe.

The joint is a complex optical system consisting of the three primary cartilage layers (superficial, intermediate, deep), calcified cartilage, subchondral bone and cancellous bone. Each layer has unique optical scattering and absorption properties which affect collection of Raman signal from articular surfaces. Optical scattering (μ_s), absorption (μ_a) coefficients and anisotropy of cartilage and bone are listed in Table 5.3. Scattering is the dominant optical property of cartilage.[22-25] Scattering is highly forward directed in cartilage, with an anisotropy of 0.94. The forward scattering of light in cartilage leads to penetration of light to great depths. The penetration depth of light through articular cartilage increases with wavelength. At 850 nm, approximately 37% of the light penetrates to 3.4 mm and approximately 13% of light penetrates to 6.8 mm.[24] Thus, the fiber-optic Raman arthroscope excitation light is expected to penetrate to the subchondral bone layer and, to a lesser extent, to cancellous bone. Because cartilage is a forward scattering medium and has a relatively weak Raman signal, the cartilage spectrum measured with a fiber-optic probe is expected to contain appreciable contributions from the underlying tissue layers.

Conclusions

In this study, Raman spectra were collected from the articular surface and cancellous bone of a human proximal radius specimen using a novel arthroscopic Raman spectroscopy instrument. These *ex vivo* experiments demonstrate proof-of-concept that a fiber-optic Raman spectroscopy instrument has potential for providing markers of contrast for cartilage or bone damage based on the molecular composition.

Optical examination techniques during arthroscopic surgery present unique challenges and opportunities. Because joints are avascular no blood interferes with the spectroscopic measurements in joint cavities. However, constrained probe volumes and the optical properties of the tissue layers provide additional challenges for Raman measurements. Furthermore, the relative Raman scattering efficiency of cartilage relative to subchondral bone needs to be further studied.

Our data indicate that the probe configuration can easily detect subsurface spectra, but will require optimization in order to maximize Raman spectra from the cartilage layer. We propose two improvements for future Raman arthroscopy. The first suggested improvement is to use a lower wavelength excitation laser because the penetration depth would decrease to about 2 mm (37% of total excitation), although tissue auto fluorescence will also be more pronounced at lower wavelengths. A second suggested improvement would be to utilize an optical method for reducing the spatial collection volume as a way to improve collection of Raman scatter from the cartilage layers and reduce the contribution from underlying bone tissue.

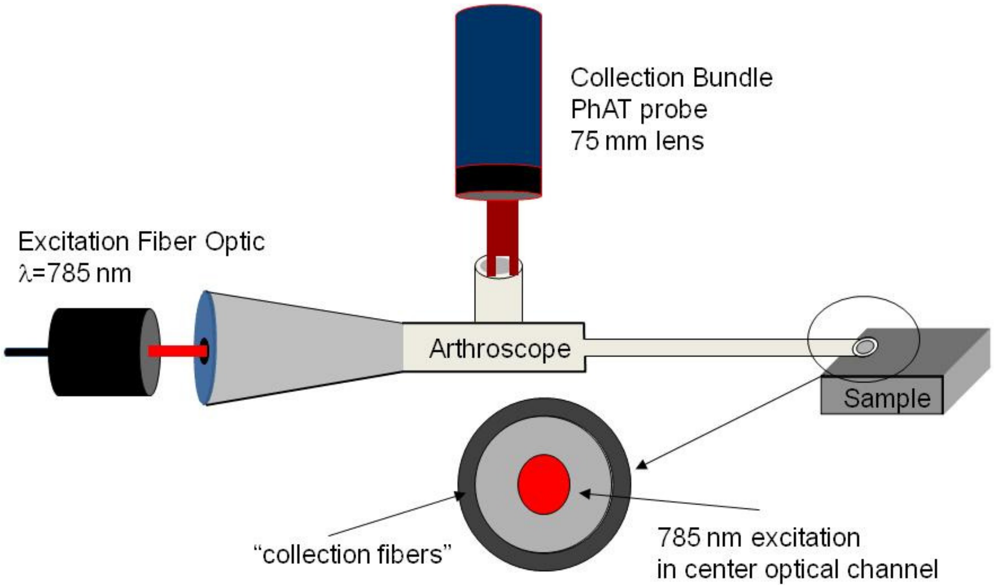

Figure 5.1: Arthroscope coupled to a fiber-optic Raman spectroscopy instrument

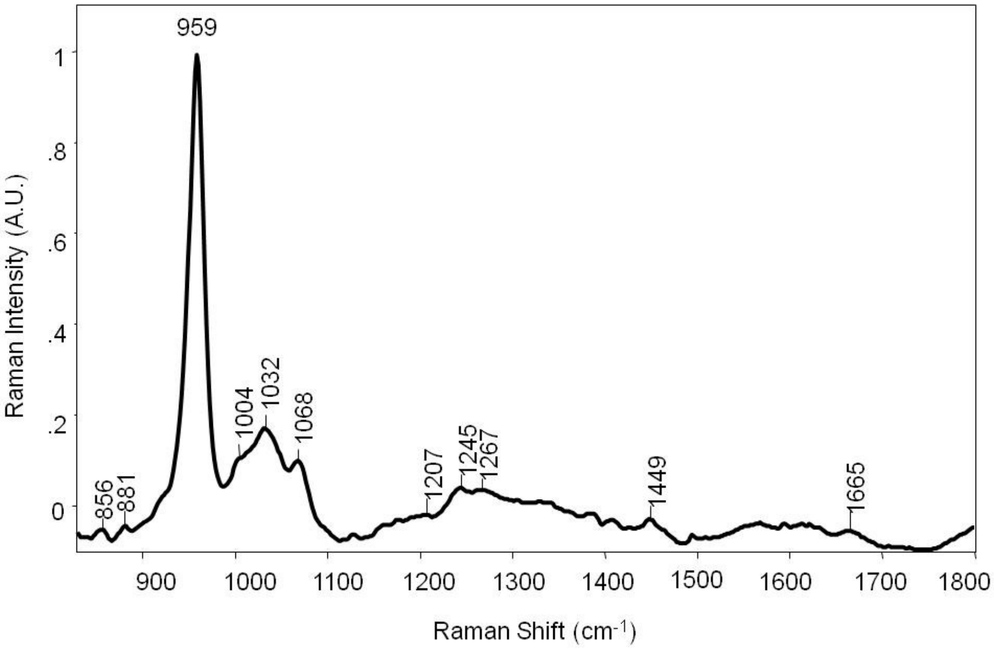

Figure 5.2: Raman spectrum of bovine bone collected from an arthroscope coupled to a fiber-optic Raman spectroscopy instrument

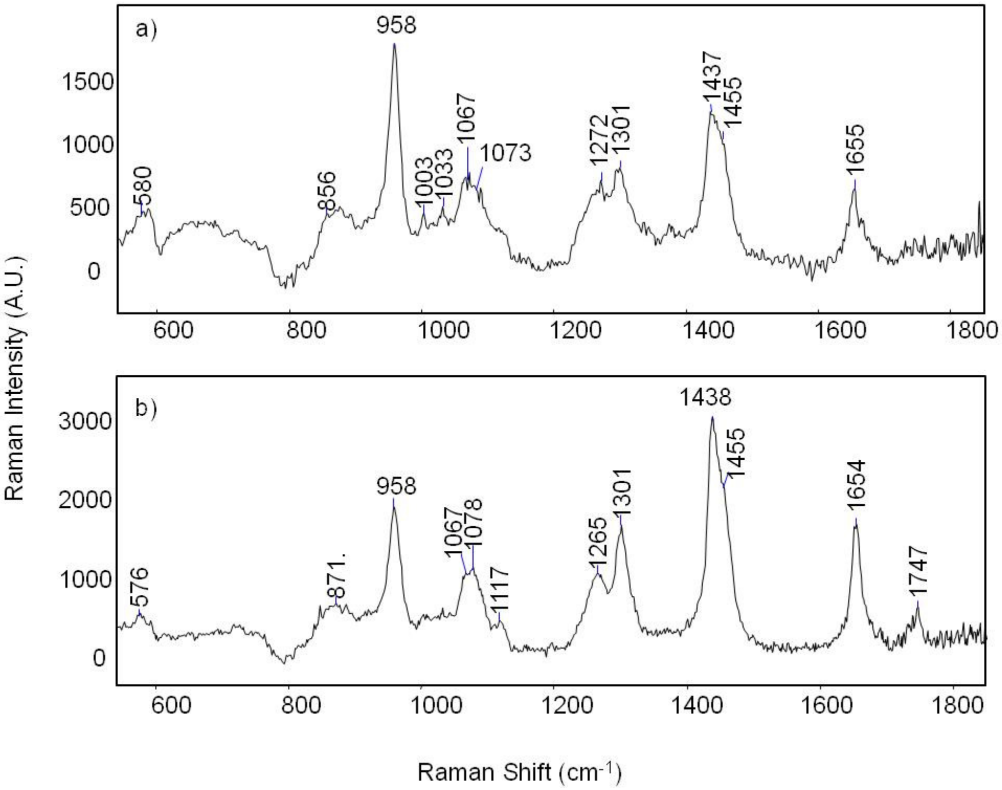

Figure 5.3: Raman spectra of proximal radius at a) articular surface with intact cartilage and b) cancellous bone collected through a fiber-optic Raman arthroscope

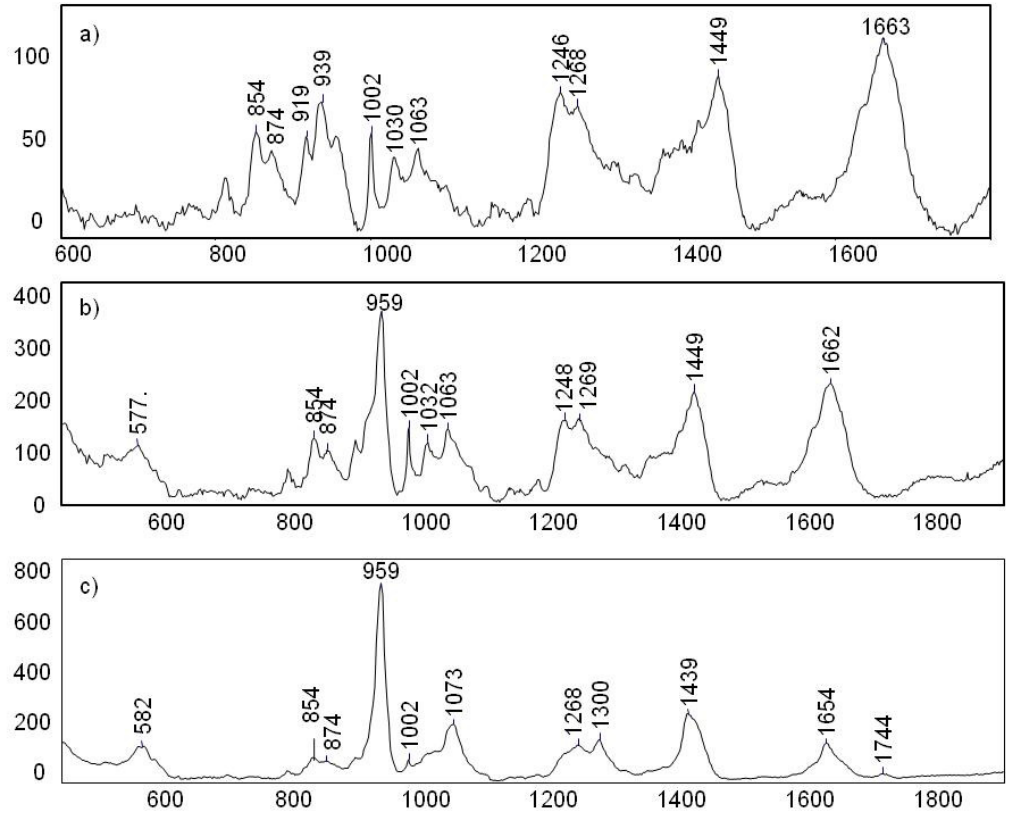

Figure 5.4: Raman spectra of proximal radius head at a) articular surface with intact cartilage, b) articular surface with cartilage removed and c) cancellous bone collected from a Raman microscope

Raman Shift (cm^{-1})	Assignment	Component
958	ν_1 PO_4^{3-}	Apatite Mineral
1001	Phenylalanine	Collagen Matrix
1062	ν C-C skeleton, trans	Lipid
1070	ν_2 CO_3^{2-}	Apatite Mineral
1079	ν C-C skeleton, random	Lipid
1268	=CH deformation	Lipid
1300	CH_2 deformation	Lipid
1439	CH_2 deformation	Lipid
1450	CH_2 deformation	Protein, Lipid
1654	ν (C=C)	Lipid
1745	ν (C=O)	Lipid

Table 5.1: Band assignments for major bands found in Raman spectra cancellous bone. Carbonated apatite mineral and lipids were the major contributions in spectra from cancellous bone.

Ratio, Specimen	Microscope	Arthroscope	**% difference**
CO_3:PO_4, subchondral bone	0.24	0.25	4
MTMR, subchondral bone	2.2	3.3	50
Amide III, subchondral bone	0.79	0.52	34
CO_3:PO_4, cancellous bone	0.21	0.28	29
MTMR, cancellous bone	6.9	3.7	46
Amide III, cancellous bone	0.47	0.41	13

Table 5.2: Raman band intensity ratios calculated from spectra of subchondral and cancellous bone on a Raman microscope (λ=785 nm) and fiber-optic Raman arthroscope (λ=830 nm)

Specimen	**λ (nm)**	**μ_s (1/cm)**	**μ_a (1/cm)**	**g**
Cartilage, rabbit	632.8	214 ± 0.2	0.33 ± 0.05	N/A
Articular cartilage, equine	850	6*	1*	0.8
Cartilage, human	633	246 ±16	1.0 ±0.1	0.95±0.01
Cortical bone, porcine	950	350±7	0.4±0.02	0.945±0.013

Table 5.3: Optical absorption and scattering coefficients of cartilage and bone in the visible or near-infrared wavelengths. Kubelka-Monk absorption and scattering coefficients were estimated for horse articular cartilage and are marked with * in the table.

References

1. Hunziker EB: **Articular cartilage repair: basic science and clinical progress. A review of the current status and prospects**. *Osteoarthritis and Cartilage* 2002, **10**(6):432-463.
2. Moskowitz RW, Altman RD, Hochberg MC, Buckwalter JA, Goldberg VM: **Osteoarthritis: diagnosis and medical/surgical management**, 4 edn. Philadelphia: Wolters Kluwer/Lippincott Williams & Wilkins; 2007.
3. David-Vaudey E, Burghardt A, Keshari K, Brouchet A, Ries M, Majumdar S: **Fourier-transform infrared imaging of focal lesions in human osteoarthritic cartilage**. *European Cells and Materials* 2005, **10**:51-60.
4. Felson DT, Neogi T: **Osteoarthritis: Is it a disease of cartilage or of bone?** *Arthritis & Rheumatism* 2004, **50**(2):341-344.
5. Squires GR, Okouneff S, Ionescu M, Poole AR: **The pathobiology of focal lesion development in aging human articular cartilage and molecular matrix changes characteristic of osteoarthritis**. *Arthritis & Rheumatism* 2003, **48**(5):1261-1270.
6. Ratcliffe A, Billingham MEJ, Saed-Nejad F, Muir H, Hardingham TE: **Increased release of matrix components from articular cartilage in experimental canine osteoarthritis**. *Journal of Orthopaedic Research* 1992, **10**(3):350-358.
7. Keuttner KE, Peyron JG, Schleyerbach R, Hascall VC: **Articular Cartilage and Osteoarthritis**. In: *Workshop Conference: Articular Cartilage and Osteoarthritis: 1991; Wiesbaden*: Raven Press; 1991.
8. Panula HE, Hyttinen MM, Arokoski JPA, Langsjo TK, Pelttari A, Kiviranta I, Helminen HJ: **Articular cartilage superficial zone collagen birefringence reduced and cartilage thickness increased before surface fibrillation in experimental osteoarthritis**. *Ann Rheum Dis* 1998, **57**:237-245.
9. Li B, Aspden RM: **Composition and Mechanical Properties of Cancellous Bone from the Femoral Head of Patients with Osteoporosis or Osteoarthritis**. *Journal of Bone and Mineral Research* 1997, **12**(4):641-651.
10. Ferguson VL, Bushby AJ, Boyde A: **Nanomechanical properties and mineral concentration in articular calcified cartilage and subchondral bone**. *Journal of Anatomy* 2003, **203**:191-202.
11. Bailey AJ, Mansell JP, Sims TJ, Banse X: **Biochemical and mechanical properties of subchondral bone in osteoarthritis**. *Biorheology* 2004, **41**(3-4):349-358.
12. Day JS, van der Linden JC, Bank RA, Ding M, Hvid I, Sumner DR, Weinans H: **Adaptation of subchondral bone in osteoarthritis**. *Biorheology* 2004, **41**(3-4):359-368.
13. Potter K, Kidder LH, Levin IW, Lewis EN, Spencer RG: **Imaging of collagen and proteoglycan in cartilage sections using Fourier transform infrared spectral imaging**. *Arthritis & Rheumatism* 2001, **44**(4):846-855.
14. West PA, Torzilli PA, Chen C, Lin P, Camacho NP: **Fourier transform infrared imaging spectroscopy analysis of collagenase induced cartilage degradation**. *Journal of Biomedical Optics* 2005, **10**(1):014015-014011-014016

15. Bi X, Yang X, Bostrom MPG, Camacho NP: **Fourier transform infrared imaging spectroscopy investigations in the pathogenesis and repair of cartilage**. *Biochimica et Biophysica Acta (BBA) - Biomembranes* 2006, **1758**(7):934-941.
16. West PA, Bostrom MPG, Torzilli PA, Camacho NP: **Fourier Transform Infrared Spectral Analysis of Degenerative Cartilage: An Infrared Fiber Optic Probe and Imaging Study**. *Applied Spectroscopy* 2004, **58**(4).
17. Pan Y, Li Z, Xie T, Chu CR: **Hand-held arthroscopic optical coherence tomography for in vivo high-resolution imaging of articular cartilage**. *Journal of Biomedical Optics* 2003, **8**(4):648-654.
18. Esmonde-White FWL, Schulmerich MV, Esmonde-White KA, Morris MD: **Automated Raman spectral preprocessing of bone and other musculoskeletal tissues**. In: *Optics in Bone Biology and Diagnostics: 2009; San Jose, CA, USA*: SPIE; 2009.
19. Chrit L, Hadjur C, Morel S, Sockalingum G, Lebourdon G, Leroy F, Manfait M: **In vivo chemical investigation of human skin using a confocal Raman fiber optic microprobe**. *Journal of Biomedical Optics* 2005, **10**(4):044007.
20. Lakshmi RJ, Alexander M, Kurien J, Mahato KK, Kartha VB: **Osteoradionecrosis (ORN) of the Mandible: A Laser Raman Spectroscopic Study**. *Applied Spectroscopy* 2003, **57**(9):1100-1116.
21. Goodyear SR, Gibson IR, Skakle JMS, Wells RPK, Aspden RM: **A comparison of cortical and trabecular bone from C57 Black 6 mice using Raman spectroscopy**. *Bone* 2009, **44**(5):899-907.
22. Beek JF, Blokland P, Posthumus P, Aalders M, Pickering JW, Sterenborg HJCM, Gemert MJCv: **In vitro double-integrating-sphere optical properties of tissues between 630 and 1064 nm**. *Physics in Medicine and Biology* 1997, **42**(11):2255-2261.
23. Qu J, MacAulay C, Lam S, Palcic B: **Optical properties of normal and carcinomatous bronchial tissue**. *Appl Opt* 1994, **33**(31):7397-7405.
24. Ebert DW, Roberts C, Farrar SK, Johnston WM, Litsky AS, Bertone AL: **Articular Cartilage Optical Properties in the Spectral Range 300--850 nm**. *Journal of Biomedical Optics* 1998, **3**(3):326-333.
25. Firbank M, Hiraoka M, Essenpreis M, Delpy DT: **Measurement of the optical properties of the skull in the wavelength range 650-950 nm**. *Physics in Medicine and Biology* 1993, **38**(4):503-510.

Chapter 6

Dynamics of Biofluid Drop Deposition

Introduction

Drop deposition of fluids, in which a small-volume drop of fluid is placed onto a flat substrate and allowed to dry, is a well characterized phenomenon that is used to model fluid dynamics, polymer film drying, and conformation of macromolecules.[1-3] Drop deposition has the dual advantages of preconcentration and a coarse separation. In its simplest model, a pinned contact line forms at the edge of the drop, capillary flow transports solute toward the contact line as solvent evaporates and a ring-shaped deposit is formed.[4, 5] A recent study showed that suppression of Marangoni flow, induced by temperature gradients within the drop, is equally important to drop formation. [2] Additional studies showed that fluid properties, solute-substrate interaction, intermolecular forces, and drying conditions affect drop shape and drop surface properties.[6-8] The resulting dried drop can be either ring-shaped, with the components coarsely separated, or a uniform deposition.

Drop deposition has been used to examine low abundance biofluids, such as tears or joint fluid, and has been shown to be useful as a potential diagnosis of eye infection or osteoarthritis.[9-11] Because the biofluid drop is typically deposited onto a flat surface, and is stable over many weeks, the same biofluid drop can be examined using many techniques, such as optical microscopy, atomic force microscopy, MALDI-MS, or Raman spectroscopy. These multiple levels of information, such as drop thickness, visual drop features and chemical composition can then be used to provide a robust description of the physiochemical and viscoelastic properties of a biofluid. A combined drop deposition/Raman spectroscopy (DDRS) technique improved Raman detection limits because fluorescence impurities are localized in the drop center and the molecule of interest is concentrated at the drop edges.[12, 13] DDRS, also called drop coating deposition Raman spectroscopy, has been shown to be an excellent technique for examining protein samples at low concentrations.[14-16] DDRS or drop deposition coupled with surface-enhanced Raman spectroscopy were used to profile drop thickness and demonstrated the relationship between a fluids viscoelastic properties and its deposition behavior.[17, 18]

Depending on the experiment, either a uniform dot or a ring-shaped deposition may be produced during drop deposition. Drop deposition can be optimized by controlling fluid preparation, environmental conditions, and substrate. Fluid preparation steps, including filtration or centrifugation, were used to remove tissue or cellular debris.[13] Incorporation of multiple centrifugal filters provided an additional dimension of mass-specific information in an examination of tear fluid by DDRS.[19] Environmental factors, such as drying conditions, can also be optimized because principles and experimental techniques for crystallization can also be applied to drop deposition. Choice of substrate for drop deposition is a simple factor to control, and it has a profound effect on drop formation.

In this study, we examined the effects of substrate surface chemistry, and fluid viscosity, and the interaction of these effects, on formation of plasma drops. Plasma was chosen as a model biofluid because plasma biomarkers and/or viscosity have been widely studied as a potential markers for obesity and cardiovascular diseases.[20, 21] Plasma was deposited onto four commercially-available substrates that spanned a broad range of surface hydrophobicity: fused silica, gold-coated glass, calcium fluoride (CaF_2) and Teflon-coated stainless steel (SpectRIM). Microscope images and Raman spectra collected from the dried drops were used to examine drop appearance and chemical composition. We found that substrate surface and fluid viscosity affected the final deposition pattern. Raman spectra of dried plasma drops showed a moderate effect of dilution on the amide I envelope intensity, but we found no significant differences in spectra collected from drops dried on different substrates.

Materials and Methods

Design of Experiments

Two main factors were examined: substrate surface chemistry and fluid viscosity. The substrate surface factor has four levels (SpectRIM, CaF_2, fused silica, gold-coated glass) and viscosity has three levels (high, medium, low). Interactions of the two factors were considered at all levels. The outcome measures were microscope image features, such as thin-films or cracks, and Raman band intensity ratios.

Materials

Freeze-dried human plasma was obtained through commercial sources, reconstituted using purified water, and used without additional preparation (Sigma, St. Louis, MO, USA). Benzoic acid (Sigma-Aldrich, St. Louis, MO, USA), and iodobenzene (98%, Acros Organics, Geel, Belgium) were used as received. A 1 mg/ml benzoic acid solution was prepared using purified water. SpectRIM (Tienta Sciences, Indianapolis, IN, USA), gold-coated glass (EMF Corporation, Ithaca, NY, USA), CaF_2 (International Crystal Laboratories, Garfield, NJ, USA), and fused silica slides were used as received.

Capillary Viscometry

A size 75 Cannon-Ubbeholde semi-micro ultra-low charge capillary viscometer, approximate viscometric constant: 0.008 (cSt/s), was used to measure viscosity of plasma dilutions. Viscosity was measured for plasma at the following dilutions: 1.0, 0.5 and 0.25 (volume fraction). Plasma dilutions were vacuum-loaded into the capillary viscometer and allowed to equilibrate in a 25°C water bath for 5 minutes prior to viscosity measurements. The standard deviation was less than 0.1 for the replicate measurements. Kinematic (η, cSt), relative (η_{rel}) and specific (η_{sp}) viscosity was calculated using Equations 1-3, where Δt is the efflux time (s), k is the viscometric constant (cSt/s) and η_0 is the kinematic viscosity of water.

$$\eta = k\Delta t \qquad \text{(Equation 1)}$$

$$\eta_{rel} = \frac{\eta}{\eta_0} \qquad \text{(Equation 2)}$$

$$\eta_{sp} = \eta_{rel} - 1 \qquad \text{(Equation 3)}$$

Static Contact Angle Measurements

A photograph was collected of a drop immediately following deposition using a digital camera. The image was imported into MATLAB (v 7.0, The Math Works, Natick, MA, USA) to magnify visualization of the drop. The magnified photo was printed and the contact angle was measured using the Young equation, as seen in Equation 4. Surface wetting was estimated from the contact angle, where low contact angle indicated good wetting and a high contact angle indicated poor wetting. Contact angle measurements of benzoic acid and iodobenzene were also collected on each of the substrates as references to encompass a range of fluid lipophilicity values.

$$0 = \gamma_{SV} - \gamma_{SL} - \gamma_{LV} \cos\theta_C \qquad \text{(Equation 4)}$$

Where γ_{SV} is the surface energy, γ_{SL} is the surface tension, γ_{LV} is the liquid surface free energy and θ_C is the contact angle.

Drop Deposition/Raman Spectroscopy

Fluids (v=2 μl) were deposited onto substrates using an Eagle micropipette (World Precision Instruments, Sarasota, FL, USA). Drops were allowed to dry at room temperature overnight. Microscopy images and Raman spectra were collected from dried drops. A Nikon E600 epi-fluorescence microscope (Nikon Inc., Melville, NY, USA) was modified for NIR Raman spectroscopy in-house. Microscope images were collected in epi-illumination mode with 2x/0.06NA Plan UW, 4x/0.20NA, 10x/0.50NA, and 20x/0.75NA S Fluor objectives (Nikon Inc., Melville, NY, USA). A 785 nm Kaiser Invictus laser was line focused (Kaiser Optical Systems Inc., Ann Arbor, MI, USA) onto dried drops using a 20x/0.75NA S Fluor objective. Laser intensity at the objective was ~ 100 mW. Raman-scattered light was collected through the same 20x/0.75 NA S Fluor objective and dispersed through a spectrograph (HoloSpec f/1.8, Kaiser Optical Systems Inc., Ann Arbor, MI, USA). Raman signal was collected for 3 minutes on a deep-depletion, back-thinned 1024x128 charge-coupled device (CCD) detector (DU401-BR-DD, Andor Technologies, Belfast, Ireland). Raman transects consisted of 126 Raman spectra arranged at equidistant points along a line through the specimen. Five transects were collected starting at 25 μm from the drop edge, spaced 20 μm apart, toward the drop center. Raman spectra were collected at the drop edge at least 25 μm from the drop edge because, in some cases, we observed protein dessication at the very edge of the drop. Raman spectra were not collected from drops dried onto CaF_2 because the CaF_2 surface produced a large background signal that prohibited detection of plasma Raman signal.

Raman Data Analysis

Data were imported into MATLAB software and corrected for curvature, dark current, and variations in the CCD quantum efficiency using in-house routines that were recently optimized.[22] Raman spectra collected from drops deposited on fused silica were not corrected for the fused silica background signal. Raman spectra were not corrected for water background signal. The mean spectrum was calculated for each transect and baseline corrected using a baseline fitting routine modified from Lieber.[23] Baseline corrected spectra of plasma were intensity-normalized to the phenylalanine ring breathing band intensity at ~1002 cm^{-1}. Table 6.3 shows the Raman band assignments. Pixel intensities corresponding the bands listed in Table 6.3 were calculated from the mean spectrum of each transect. Band intensity ratios corresponding to protein primary and secondary structure were calculated.[24, 25]

Results

Figure 6.1.a depicts the simultaneous concentration of biofluid (filled dots) at the drop edges and a coarse separation of biofluid from small salts or impurities (non-filled dots). Figure 6.1.b is a representation of Sommer's drop formation model, adapted for biofluid drop formation. There are two primary flows, capillary flow (F_C) and Marangoni flow (F_M), and two primary interactions, substrate-fluid interaction (I_S) and intermolecular interactions (I_{MM}). Table 6.1 shows how viscosity and contact angle measurements were interpreted as indications of the fundamental flows and interactions that guide drop deposition. Higher contact angle indicated poor substrate-fluid interaction and a higher Marangoni flow. Higher viscosity values indicated a greater degree of intermolecular interactions and reduced capillary flow.

Table 6.2 shows the contact angles of plasma on four commercially-available substrates. At any given plasma concentration, the contact angle was the highest for plasma drops on the SpectRIM substrate and the lowest on fused silica. Contact angle of plasma solutions were similar when deposited onto CaF_2 or gold-coated glass. The contact angle increased with decreasing plasma concentration when deposited on CaF_2, gold-coated glass and fused silica. Plasma contact angles decreased with plasma concentration when deposited onto SpectRIM substrates. Solutions of benzoic acid (log P=1.87) and iodobenzene (log P=3.25) were deposited onto all four substrates as lipophilicity standards.[26]

Figure 6.2 shows the effects of fluid viscosity and substrate on the deposition pattern of plasma on SpectRIM (1st row), CaF_2 (2nd row), gold-coated glass (3rd row) and fused silica (4th row). We observed that the deposition behavior of plasma was similar when deposited on fused silica, gold-coated glass and CaF_2. Plasma solutions deposited onto SpectRIM substrates dried in a different pattern and were characterized by large full-depth cracks in the dried drop. Figure 6.3 shows Raman spectra of plasma (0.5 v/v) deposited onto a) fused silica, b) SpectRIM, and c) gold-coated glass. CaF_2 was reported as a background-free substrate for drop deposition of tear fluid.[10] However, we found that the CaF_2 surface produced a large background signal that prohibited detection of plasma Raman signal. It is possible that the higher laser intensity in our study produced a non-linear effect in the CaF_2 crystal lattice giving rise to higher order bands in the 800-1700 cm^{-1} spectral region. The effect of water on Raman spectra of dried plasma drops was examined. Figure 6.4.a compares Raman spectra from plasma dried on gold-coated glass at three plasma concentrations. Figure 6.4.b shows that the normalized intensity of the amide I maximum at ~ 1655 cm^{-1} increases with decreasing plasma concentration. Table 6.4 shows Raman band intensity ratios corresponding to markers of protein primary and secondary structure for plasma dilutions deposited onto gold-coated glass.

Discussion

Microscope images revealed that the substrate used for drop deposition had an effect on the drop size and deposition pattern of dried plasma drops. As shown in Figure 6.2, the size and shape of the resulting dried drop varied because of the different substrate wetting properties. Plasma dried in a symmetric circular drop when deposited onto CaF_2 or gold-coated glass, but dried as an asymmetric circle when deposited onto fused silica. Because of the moderate wetting properties of CaF_2, gold-coated glass and fused silica, I_S was sufficiently low to allow ring formation and we observed a separation of plasma components. On these substrates, plasma dried as a smooth film-like ring at the drop edge with a crystalline deposit in the drop center when placed onto fused silica, CaF_2 and gold-coated glass.

An unexpected finding was that undiluted plasma formed a uniform dot when deposited onto SpectRIM substrates. We observed a large contact angle (θ_C>80°) of plasma drops on the SpectRIM substrate, which indicated incomplete surface wetting and a more pronounced Marangoni effect. We also observed that plasma drops shrunk during evaporation on SpectRIM. From these observations, we inferred that plasma did not form a pinned contact line on the SpectRIM substrate. Because the contact line was not pinned and Marangoni flow may not have been adequately suppressed, we concluded that plasma did not form a ring on SpectRIM substrate and our model of biofluid drop formation does not adequately describe biofluid deposition onto highly hydrophobic surfaces. It is more likely that plasma undergoes a piling-to-bucking transition, as described by Tadashi et al, during the evaporation process. Piling-to-bucking is commonly observed when polymer solutions are deposited onto highly hydrophobic surfaces.[1] Higher magnification microscope images revealed that plasma dried on SpectRIM substrates as a uniform deposition in the shape of a concave dot, which support a bucking-to-piling model. Raman spectra collected across the surface of uniform dot further supported this hypothesis.

The observation that undiluted plasma formed a uniform dot on SpectRIM substrates was unexpected because previous reports had shown ring formation of low concentration (µM-mM) protein solutions.[12, 13] However, the protein concentration in plasma is 100x greater than protein solutions where ring formation was reported. Higher protein concentrations and the presence of biopolymers such as glycoproteins, lipids, or polysaccharides in plasma resulted in a higher fluid viscosity. Because of the inverse relationship between viscosity and capillary flow, higher fluid viscosity, coupled with poor wetting on the SpectRIM substrate, resulted in formation of a uniform dot for plasma instead of a ring for protein solutions. Formation of a uniform dot can be advantageous for some analytical approaches because segregation of components is undesirable. For example, a uniform dot is the preferred deposition pattern for liquid MALDI-MS samples because matrix is not segregated from the analyte, enabling more efficient analyte ionization. We observed partial ring formation in dried drops of diluted plasma because there was a slightly lower contact angle and the fluid was less viscous. These two factors enabled ring formation of diluted plasma on SpectRIM substrates.

Raman spectroscopy of dried drops provided an indication about the effects of dilution or ring formation on protein secondary structure and hydration. 5 transects were collected across approximately a 100 μm section of the dried outer ring, at least 25 μm interior to the ring edge. Spectra collected from dried plasma drops were dominated by albumin contributions. Within a single drop, the measured area was chemically homogeneous, and the standard deviation of mean spectra corresponding to the 5 transects was less than 0.02. High magnification (80x) Raman spectra collected within a deposited ring of aqueous protein mixtures indicated chemical heterogeneity.[27] Although the chemical composition of plasma is primarily albumin, it is chemically heterogeneous. It is possible that, at higher magnifications, we would also observe Raman bands that could be attributed to individual plasma proteins. In another approach, tryptic digestion of albumin or preparative chromatography can be used to prepare plasma prior to drop deposition. These preparative steps may enable detection of low abundance plasma proteins.

We observed minor effects of substrate surface on Raman spectra collected from dried plasma drops, and the differences primarily arose because fused silica background signal overlapped with a few of the measured band intensities. The effects of substrate surface are presented in Figure 6.3 that shows representative spectra of undiluted plasma after drying on a) fused silica, b) SpectRIM and c) gold-coated glass. A large background signal from the fused silica is evident in the top spectrum of Figure 6.3.a. Filik and Stone reported similar findings.[27] The normalized intensity of the amide I envelope at ~ 1655

cm^{-1} is slightly higher in Raman spectra collected from plasma deposited onto fused silica. Most ratios were not significantly affected by substrate surface at any single plasma dilution.

There were moderate concentration effects when plasma dilutions were deposited onto a single substrate, most notably in the amide I envelope maximum. The maximum of the amide I envelope at ~ $1655cm^{-1}$ increased in spectra collected from dried drops of diluted plasma. Figure 6.4.a illustrates this effect on plasma deposited onto gold-coated glass. Undiluted plasma (bottom spectrum) has the lowest normalized Amide I intensity while the 0.25 v/v plasma (top spectrum) has the highest normalized Amide I intensity. Figure 6.4.a also shows that the bands at ~1603 cm^{-1} and 1617 cm^{-1}, corresponding to Phe and Tyr amino acids in albumin, are less resolved in spectra collected from diluted plasma drops. Figure 6.4.b shows the trend of increasing Amide I envelope intensity was independent of the substrate surface. Linear trendlines were calculated for fused silica: $y = -0.2406x + 0.9701$ ($R^2=0.90$), for SpectRIM: $y = -0.2405x + 0.8768$ ($R^2=0.96$), for gold-coated glass $y = -0.2804x + 0.9133$ ($R^2=0.99$).

Dilution had a minimal effect on the secondary structure of plasma proteins, as measured the intensity ratio of amide I bands at 1655 cm^{-1} and 1670 cm^{-1}. We conclude that water used to dilute plasma samples affected the Raman measurements in two ways. The first is an increased efficiency in the Raman scatter of more dilute solutions. Dried drops of highly concentrated solutions have more light scattering centers which decreases collection efficiency because the excitation laser is spread out over a wider surface area. A higher plasma concentration may also result in a higher index of refraction. The second factor is the presence of additional free water. Raman O-H stretching bands from water bound to plasma proteins, arise in the amide I envelope at 1630-1645 cm^{-1}, and free water at ~ 1650 cm^{-1}.[28]

Conclusions

Drop deposition is a simple, yet powerful, technique to prepare biofluids for a variety of analytical tools. Multiple levels of information can be obtained from a single drop and the technique can be modified for robotic liquid handling. The resulting dried drop can be either a ring-shaped deposit or a uniform dot. Once the proper conditions are identified, it is simple to produce either type of deposition pattern. Because the evaporation process is a simplified crystallization process, drying conditions can be controlled to ensure that the desired type of deposit is obtained. A condition that can be easily modified is the choice of substrate. There are several commercially-available substrates suitable for DDRS that have surface chemistries amenable to drop or uniform dot formation.

Simple physical measurements, such as contact angle and viscosity, incorporated into a drop deposition study can aid in interpreting the dried drop and provide insight into the complex drop deposition process. By measuring the contact angle plasma deposited onto a substrate, we obtained a relative measure of temperature gradients within the drop. Viscosity measurements provided an indication about the relative capillary flow and intermolecular interactions. Together, these measurements can help predict formation of a uniform dot or ring-shaped deposit, and provide additional information about the biofluid physical properties. We demonstrated that either a ring-shaped or uniform dot deposit can be obtained for plasma by using a different substrate. Microscopy images of dried plasma drops were used to determine the type of deposit and identify visual features such as thin-film accumulations or cracks within the drop.

Raman spectra collected from dried plasma drops suggest that the chemistry of the protein-rich outer edge in the dried drop was consistent when dried on different substrates. Dilution of plasma affected both the optical properties and the amount of free water in the dried drop. We concluded that the choice of substrate affects the final deposition pattern and the efficiency of the coarse separation. However, the important biofluid protein components remain unaffected during the evaporation process.

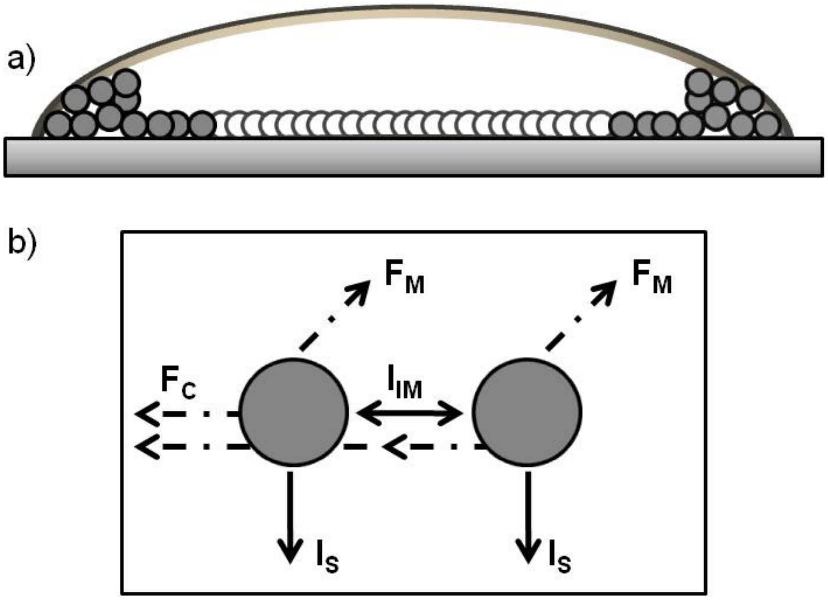

Figure 6.1: Drop deposition provides simultaneous coarse separation and preconcentration, as shown in Figure 6.1.a. Biofluid (closed circles) is concentrated in a ring at the outer edge of the drop while salts (open circles) are deposited in the drop center. Figure 6.1.b shows the primary flows and interactions that guide biofluid drop formation. Capillary flow, F_C is responsible for fluid motion toward the pinned contact lines at the drop edge, upward Marangoni flow, F_M, arises from a temperature gradient within the drying drop. Substrate and fluid interactions, I_S, and intermolecular interactions, I_{IM}, also influence drop deposition.

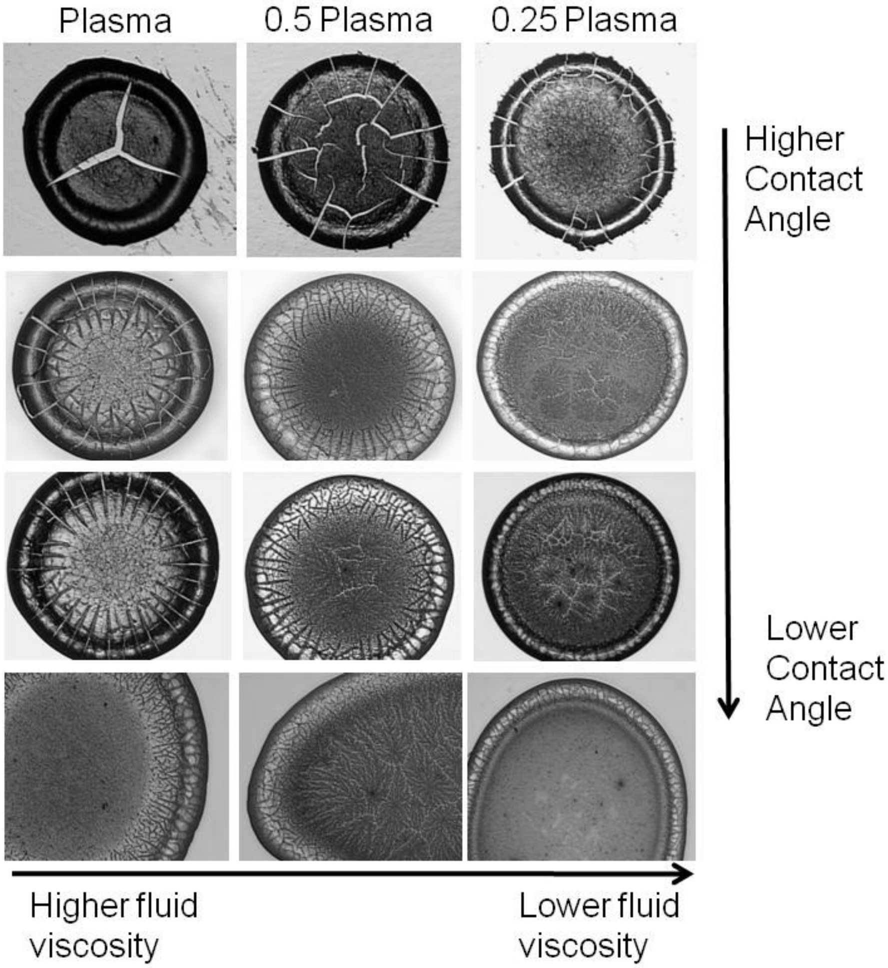

Figure 6.2: Low magnification microscope images of dried plasma drops shows the effect of substrate surface and fluid viscosity on the appearance of the dried drop.

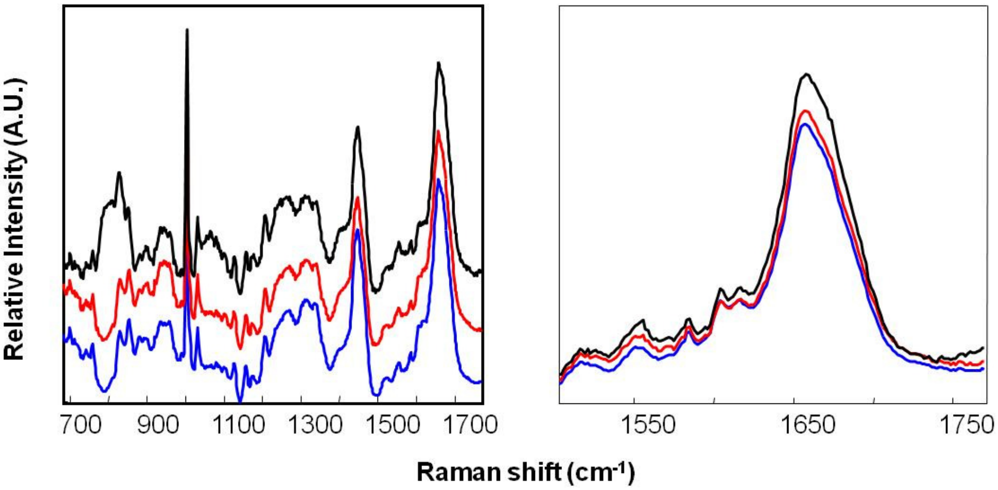

Figure 6.3: Raman spectrum of 0.5 v/v dried plasma drops after deposition on fused silica (top spectrum), SpectRIM (middle spectrum), and gold coated glass (bottom spectrum) in the 700-1700 cm^{-1} spectral region. Spectra in Figure 6.3.a are offset for clarity. Figure 6.3.b shows the amide I envelope at 1550-1750 cm^{-1}.

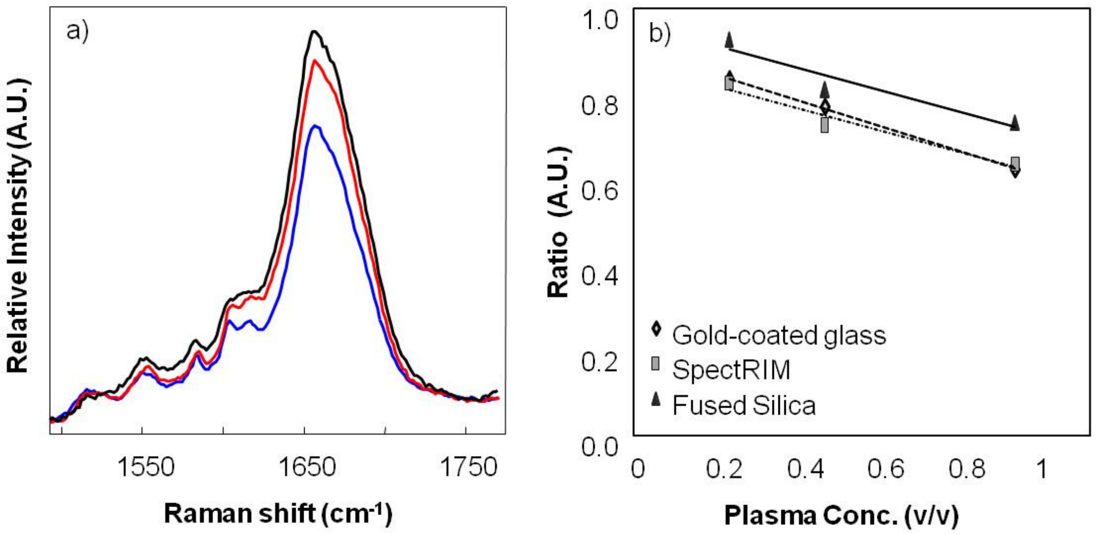

Figure 6.4: Raman spectrum of dried drops of 0.25 v/v (top spectrum), 0.5 v/v (middle spectrum), and undiluted (bottom spectrum), plasma after deposition on gold-coated glass in the amide I envelope at 1550-1750 cm^{-1}. Figure 6.4.b. shows the trend of increasing normalized amide I intensity with plasma dilution. The trendlines shown in Figure 6.4.b have an R^2 between 0.90 for fused silica to 0.99 for gold-coated glasses.

Interaction/Flow	Physical Measurement	Interpretation
Fluid-Substrate interaction (I_S)	Contact angle (θ_C)	$I_S \propto 1/\theta_C$
Intermolecular interactions (I_{MM})	Specific viscosity (η_{sp})	$I_{MM} \propto \eta_{sp}$
Capillary Flow (F_C)	η_{sp}	$F_C \propto 1/\eta_{sp}$
Marangoni Flow (F_M)	θ_C	$F_M \propto \theta_C$

Table 6.1: The relationship between measured physical properties and fundamental phenomenon that guide the drop deposition process. Contact angle is proportional to Marangoni flow (F_M in Figure 6.1) and inversely proportional to fluid-substrate interactions (I_S). A higher contact angle indicated reduced I_S and higher effects from F_M. Viscosity is proportional to intermolecular interactions (I_{IM}) and inversely proportional to capillary flow (F_C). Higher viscosity values indicated reduced F_C and higher I_{IM}.

	SpectRIM	CaF_2	Gold-coated glass	Fused silica
Plasma	88	57	53	29
0.5 v/v Plasma	87	61	59	34
0.25 v/v Plasma	85	71	62	39
Benzoic acid (aq)	86	84	44	43
Iodobenzene	82	60	< 10	49

Table 6.2: Contact angle of a drop was measured immediately after deposition onto a substrate.

Raman Shift (cm^{-1})	Band Assignment	Component
828	Tyr	Protein
852	Tyr	Protein
938	α-helix	Protein
1002	Aromatic ring breathing	Protein
1080	C-N, C-C stretch	Protein
1310	C-H/CH_2 bend	Protein
1340	C-H/CH_2 bend	Protein
1446	CH_2/CH_3 deformation	Organic content
1655	Amide I, α-helix	Protein
1670	Amide I, random coil	Protein

Table 6.3: Raman band assignments of dried plasma drops

Band Intensity Ratio	Undiluted Plasma	0.5 v/v Plasma	0.25 v/v Plasma
1655 cm^{-1}:1670 cm^{-1} (Amide I)	0.912	0.933	0.930
1080 cm^{-1}: 1002 cm^{-1}	0.133	0.140	0.144
852 cm^{-1}: 828 cm^{-1}	1.149	1.162	1.201
1340 cm^{-1}: 1310 cm^{-1}	0.995	0.965	0.977
1655 cm^{-1}: 1002 cm^{-1}	0.632	0.777	0.841
1448 cm^{-1}: 1002 cm^{-1}	0.616	0.652	0.683

Table 6.4: Raman band intensities of undiluted plasma, 0.5 v/v and 0.25 v/v plasma solutions deposited onto gold-coated glass.

References

1. Tadashi K, Eisuke N, Tatsuya Y, Masao D: **Piling-to-buckling transition in the drying process of polymer solution drop on substrate having a large contact angle**. *Physical Review E (Statistical, Nonlinear, and Soft Matter Physics)* 2006, **73**(1):011601.
2. Hu H, Larson RG: **Marangoni Effect Reverses Coffee-Ring Depositions**. *J Phys Chem B* 2006, **110**(14):7090-7094.
3. Chopra M, Li L, Hu H, Burns MA, Larson RG: **DNA Molecular Configurations in an Evaporating Droplet Near a Glass Surface**. *Journal of Rheology* 2003, **47**:1111-1132.
4. Deegan RD, Bakajin O, Dupont TF, Huber G, Nagel SR, Witten TA: **Contact line deposits in an evaporating drop**. *Physical Review E* 2000, **62**(1):756.
5. Deegan RD, Bakajin O, Dupont TF, Huber G, Nagel SR, Witten TA: **Capillary flow as the cause of ring stains from dried liquid drops**. *Nature* 1997, **389**(6653):827-829.
6. Sommer AP: **Microtornadoes under a Nanocrystalline Igloo: Results Predicting a Worldwide Intensification of Tornadoes**. *Crystal Growth & Design* 2007, **7**(6):1031-1034.
7. Sommer AP, Rozlosnik N: **Formation of Crystalline Ring Patterns on Extremely Hydrophobic Supersmooth Substrates: Extension of Ring Formation Paradigms**. *Crystal Growth & Design* 2005, **5**(2):551-557.
8. Adachi E, Dimitrov AS, Nagayama K: **Stripe Patterns Formed on a Glass Surface during Droplet Evaporation**. *Langmuir* 1995, **11**:1057-1060.
9. Yakhno T, Sedova O, Sanin A, Pelyushenko A: **On the existence of regular structures in liquid human blood serum (plasma) and phase transitions in the course of its drying**. *Technical Physics* 2003, **48**(4):399-403.
10. Filik J, Stone N: **Analysis of human tear fluid by Raman spectroscopy**. *Analytica Chimica Acta* 2008, **616**(2):177-184.
11. Esmonde-White KA, Mandair GS, Raaii F, Jacobson JA, Miller BS, Urquhart AG, Roessler BJ, Morris MD: **Raman spectroscopy of synovial fluid as a tool for diagnosing osteoarthritis**. *Journal of Biomedical Optics* 2009, **14**(3):034013.
12. Zhang D, Mrozek MF, Xie Y, Ben-Amotz D: **Chemical Segregation and Reduction of Raman Background Interference Using Drop Coating Deposition**. *Applied Spectroscopy* 2004, **58**(8):929-933.
13. Ortiz C, Zhang D, Xie Y, Ribbe AE, Ben-Amotz D: **Validation of the drop coating deposition Raman method for protein analysis**. *Analytical Biochemistry* 2006, **353**(2):157-166.
14. Zhang D, Xie Y, Mrozek MF, Ortiz C, Davisson VJ, Ben-Amotz D: **Raman Detection of Proteomic Analytes**. *Anal Chem* 2003, **75**(21):5703-5709.
15. Ortiz C, Zhang D, Xie Y, Davisson VJ, Ben-Amotz D: **Identification of insulin variants using Raman spectroscopy**. *Analytical Biochemistry* 2004, **332**(2):245-252.
16. Xie Y, Zhang D, Jarori GK, Davisson VJ, Ben-Amotz D: **The Raman detection of peptide tyrosine phosphorylation**. *Analytical Biochemistry* 2004, **332**(1):116-121.

17. Kopecký JV, Baumruk V: **Structure of the ring in drop coating deposited proteins and its implication for Raman spectroscopy of biomolecules**. *Vibrational Spectroscopy* 2006, **42**(2):184-187.
18. Esmonde-White KA, Le Clair SV, Roessler BJ, Morris MD: **Effect of Conformation and Drop Properties on Surface-Enhanced Raman Spectroscopy of Dried Biopolymer Drops**. *Appl Spectrosc* 2008, **62**(5):503-511.
19. Filik J, Stone N: **Investigation into the protein composition of human tear fluid using centrifugal filters and drop coating deposition Raman spectroscopy**. *Journal Of Raman Spectroscopy* 2008, **40**(2):218-224.
20. Ercan M, Konukoglu D, Yesim TE: **Association of plasma viscosity with cardiovascular risk factors in obesity: An old marker, a new insight**. *Clinical Hemorheology and Microcirculation* 2006, **35**(4):441-446.
21. Koenig W, Sund M, Filipiak B, Doring A, Lowel H, Ernst E: **Plasma Viscosity and the Risk of Coronary Heart Disease : Results From the MONICA-Augsburg Cohort Study, 1984 to 1992**. *Arterioscler Thromb Vasc Biol* 1998, **18**(5):768-772.
22. Esmonde-White FWL, Schulmerich MV, Esmonde-White KA, Morris MD: **Automated Raman spectral preprocessing of bone and other musculoskeletal tissues**. In: *Optics in Bone Biology and Diagnostics: 2009; San Jose, CA, USA*: SPIE; 2009.
23. Lieber CA, Mahadevan-Jansen A: **Automated Method for Subtraction of Fluorescence from Biological Raman Spectra**. *Applied Spectroscopy* 2003, **57**(11):1363-1367.
24. Lin VJC, Koenig JL: **Raman studies of bovine serum albumin**. *Biopolymers* 1976, **15**(1):203-218.
25. Chourpa I, Ducel V, Richard J, Dubois P, Boury F: **Conformational Modifications of α– Gliadin and Globulin Proteins upon Complex Coacervates Formation with Gum Arabic as Studied by Raman Microspectroscopy**. *Biomacromolecules* 2006, **7**(9):2616-2623.
26. Poole SK, Patel S, Dehring K, Workman H, Dong J: **Estimation of octanol-water partition coefficients for neutral and weakly acidic compounds by microemulsion electrokinetic chromatography using dynamically coated capillary columns**. *Journal of Chromatography B* 2003, **793**(2):265-274.
27. Filik J, Stone N: **Drop coating deposition Raman spectroscopy of protein mixtures**. *The Analyst* 2007, **132**:544-550.
28. Sane SU, Cramer SM, Przybycien TM: **A Holistic Approach to Protein Secondary Structure Characterization Using Amide I Band Raman Spectroscopy**. *Analytical Biochemistry* 1999, **269**(2):255-272.

Chapter 7

Raman Spectroscopy of Synovial Fluid as a Tool for Diagnosing Osteoarthritis

Introduction

Osteoarthritis (OA) is considered a disease of the whole joint as a result of biological, chemical and viscoelastic changes to the cartilage, synovium, subchondral bone, and synovial fluid.[1, 2] Synovial fluid research is important not only to understand the role of synovial fluid (SF) in OA pathophysiology but also to identify biomarkers that may have significant diagnostic value. SF is primarily composed of water, proteins, proteoglycans, glycosaminoglycans (GAGs), lipids, small inorganic salts, and metabolites such as amino acids or sugars. Moreover, individual SF components may often perform multiple functions. For example, hyaluronic acid (HA), an unsulfated GAG, maintains the complex viscoelastic properties of SF and regulates the biological activity of advanced glycation end-products, cytokines, and enzymes associated with OA.[3-5] Normal joint function is dependent on the status of SF composition, especially considering the large interaction between the individual SF components. Therefore, measurements that reflect the entire SF chemical, biological or viscoelastic profile may prove to be a robust approach to the clinical diagnosis of OA.

Analysis of SF is an attractive target for the early detection of OA damage because it allows for collection of multiple levels of information from the clinic and the laboratory. SF aspirates are obtained using a sterile needle and thus allows the rheumatologist to perform an preliminary visual inspection for features such as color, clarity, string test, and the mucin clot test.[6, 7] Although these visual tests have been used by rheumatologists for the past 50 years, they provide limited quantitative data. To obtain more quantitative result, viscosity measurements on SF aspirates can be performed. This approach has been used to establish the deleterious effects of OA and age on SF viscosity. [8] More recently, the measurement of mechanical properties of SF, such as lubricity, suggest an untapped potential for SF-based diagnostics of OA.[9]

Besides changes in viscosity, SF in arthritic joints may undergo biochemical and chemical changes, such as alterations in protein composition and proteomic profile. [10, 11] Chemical changes affect many types of SF molecules. The complexity of this disease is reflected in the lack of a consensus regarding OA biomarkers in SF, serum or urine. Two approaches have been presented in the literature. The first approach is to look for a single molecular marker, and recent studies have shown that cartilage oligomeric matrix protein (COMP) is a promising marker. [10, 12-16] Arthritic SF may contain higher levels of cartilage fragments, low molecular weight HA molecules, and basic calcium phosphate crystals.[17-19] Another approach is to examine the entire chemical profile and proteomic analysis, using 2-D electrophoresis or mass spectrometry, has been demonstrated for SF.[20] A recent SF proteomic analysis had found changes in abundant proteins in SF from arthritic joints, but these changes in protein profile were not dependent on the stage of OA.[11] Biochemical and chemical changes that occur in SF associated with OA progression have been examined using immunoassay, chromatography, or mass spectrometry and the results are typically compared with clinical measures of severity including conventional radiographs, magnetic resonance imaging, or arthroscopy.[21-23]

Molecular spectroscopy techniques, such as near-infrared (NIR), Raman and infrared spectroscopy, are used to analyze biomedical specimens such as cells, tissues or fluids because of their specificity, ease-of-use, and non-destructive nature.[24, 25]. Vibrational spectroscopy has been used to examine joint tissues, and spectra identified early chemical alterations in animal and human arthritic cartilage or subchondral bone.[26-30] NIR and Fourier-transform infrared (FTIR) spectroscopy have both been used to analyze the chemical composition of SF from osteoarthritis, rheumatoid arthritis, or spondyloarthropathy patients.[31-34] NIR or FTIR spectra of dried SF films allowed automated identification of arthritis with a classification rate greater than 95%. Individual components in SF could not be identified using NIR or FTIR spectra. However, the overall chemical composition did correlate with spectral patterns. These early studies provided evidence that vibrational spectra of SF could be used to discriminate between different types of arthritis. A fuzzy C-means cluster/adaptive wavelet analysis of IR spectra from SF films yielded good agreement with clinical diagnosis for OA and rheumatoid arthritis (Kappa,κ=0.6).[34]

Drop deposition, also known as the “coffee ring” effect, is a simple technique in which a fluid drop dries on a solid substrate.[35] Drop deposition differs from film preparation because a rough separation of components occurs and the solution state conformation is preserved during the drop drying process. Because drops are typically deposited on a flat solid substrate, the dried drops can be examined using one or more microscopy or spectroscopy tools. Drop deposition of biofluids is a potential biomedical diagnostic, owing to its simplicity, small volume requirements, and broad applicability.[36, 37] Recently, Raman spectroscopy has been used in conjunction with drop deposition to examine protein mixtures and biofluids.[38, 39] A combined drop deposition/Raman technique for tears and synovial fluid showed subtle differences in the chemical composition at various locations in a drop. [40, 41] Raman signal of poorly scattering components can be improved because impurities that fluoresce, and otherwise dominate the Raman spectra, are segregated in the drop center during the drying process.[42] Multiple studies that compared solution and dried drop Raman spectra of proteins found that solution-state conformation of proteins is preserved during the deposition process.[43, 44] Raman band intensities were used to estimate the relative thickness of dried albumin or HA drops.[44, 45]

In this study, drop deposition/Raman spectroscopy (DDRS) was used as a method to assess knee OA severity and was compared with conventional radiographs. DDRS of SF does not require specimen pretreatment or extensive preparation. The purpose of this study was to identify Raman spectroscopic markers in SF associated with knee OA. Raman band intensity ratios used to describe protein content and structure correlated with

Kellgren/Lawrence (K/L) radiographic scoring of OA damage. These results are the first indications that DDRS may have value for rapid staging of knee OA.

Materials and Methods

Clinical Protocol

All aspects of the clinical protocol were reviewed and approved by the University of Michigan Medical School Institutional Review Board (IRBMED). A total of 40 patients with clinical symptoms of chronic knee pain, and who were also scheduled for elective surgical treatment were enrolled in the study. Pre-operative conventional postero-antero radiographs of the symptomatic knee were reviewed by a musculoskeletal radiologist. Radiographs were read using the Osteoarthritis Research Society International atlas for identification of definite osteophytes [46] and OA was defined as the presence of a definite osteophyte in any of three views in accordance with American College of Rheumatology criteria for knee OA [47]. Overall radiographic severity of OA was assessed using Kellgren/Lawrence (K/L) criteria on the postero-antero view only [48]. Patients were classified into two groups by K/L score. Even though all of the patients presented clinical evidence of OA (knee effusion and pain), x-rays of the affected knee joint had found that 17 patients had a low K/L score (K/L=0-1) and were placed in the negative for radiological OA (-/ROA) group. Patients with a K/L score above 2 (K/L=2-4) were placed in the positive for radiological OA (+/ROA) group. These grouping are congruent with other arthritis studies that use a K/L score.[12, 15, 49, 50]

22 patients in the study underwent total knee arthroplasty, 1 patient underwent hemiarthroplasty and 17 patients underwent therapeutic arthroscopy. Patient demographics are shown in Table 1. At the time of surgery, SF was obtained from the knee by needle aspiration using a size 18 gauge needle and immediately placed into glass specimen tubes. (SCAT-1, Haematologic Technologies Inc., Essex Junction, VT, USA). SCAT-1 tubes contained 25 $\mu\underline{M}$ Phe-Pro-Arg-chloromethylkeytone as an anti-coagulant, 200 KIU/ml aprotinin as an enzyme inhibitor and 4.5 m$\underline{M}$ EDTA buffer. Additives in SCAT-1 tubes were examined using Raman spectroscopy to verify that their Raman spectrum does not overlap with SF Raman bands. Macroscopic debris in SF was removed

by low speed centrifugation and specimens were aliquoted then snap frozen and stored at -80°C until use.

Power Analysis

A total of N=40 subjects and a normal distribution of K/L scores with 20 subjects in the -/ROA (K/L=0-1) group and 20 subjects in the +/ROA (K/L=2-4) group was assumed for *a priori* power calculations. A two-sample t-test of means with a 95% confidence limit yielded a power of 87% (N=40) to detect moderate differences between -/ROA and +/ROA groups. Raman data from three SF specimens were removed from the -/ROA group when comparing Raman band intensity ratios because these specimens had severe contamination from hemoglobin or anti-coagulant from the storage vial. Raman data of synovial fluid from 37 patients were used in comparing Raman band intensity ratios between -/ROA (n=14) and +/ROA (n=23) groups. For N=37, the power was 84%. The power for a comparison of all five K/L groups (0-4) was 62% using an ANOVA, one-way, fixed effect f-test. The *a priori* power tests indicated adequate power for comparison of differences between -/ROA and +/ROA groups.

Drop Deposition of Synovial Fluid

Synovial fluid from all 40 patients was examined using the DDRS protocol. SF specimens were examined without extensive preparation. Two small volume (2-10 µl) drops of synovial fluid were deposited onto a fused silica slide using an Eagle pipette (World Precision Instruments, Sarasota, FL, USA). Drops were allowed to dry overnight, semi-covered, at room temperature then examined the following day using light microscopy and Raman spectroscopy. Light microscope images were taken for both SF drops, and Raman spectra were collected from one SF drop.

Microscopy/Raman Spectroscopy

A Nikon E600 epi-fluorescence microscope (Nikon Inc., Melville, NY, USA) was modified for NIR Raman spectroscopy in-house. Microscope images were collected in epi-illumination and transmission illumination modes with 2x/0.06NA, 4x/0.20NA, 10x/0.50NA, and 20x/0.75NA S Fluor objectives (Nikon Inc., Melville, NY, USA). A

785 nm Kaiser Invictus laser was line focused (Kaiser Optical Systems Inc., Ann Arbor, MI, USA) onto dried drops using a 20x/0.75NA S Fluor objective. Raman-scattered light was collected through the same 20x/0.75 NA S Fluor objective and dispersed through a spectrograph (HoloSpec *f*/1.8, Kaiser Optical Systems Inc., Ann Arbor, MI, USA). Raman signal was collected for 10 minutes on a charge-coupled device (CCD) detector optimized for near-infrared wavelengths (DU401-BR-DD, Andor Technologies, Belfast, N. Ireland). Raman transects consisted of 126 Raman spectra arranged at equidistant points along a line through the specimen. 6-12 transects were collected at various locations across the surface of each of the dried drops. A total of 418 Raman transects (52,668 spectra) were collected in this study.

Data Analysis

Raman data was collected and processed without prior knowledge of the radiography results. Data were imported into MATLAB software (v 7.0, The Math Works, Natick MA) and corrected for curvature, dark current, and variations in the CCD quantum efficiency. A mean spectrum was calculated from each transect after correction for the fused silica background. The mean spectrum was imported into GRAMS/AI (ThermoGalactic, Salem, NH, USA) and baseline corrected using a user-defined multi-point baseline fitting routine. Baseline corrected spectra were intensity-normalized to the phenylalanine ring breathing band intensity at ~1002 cm^{-1} because it was the best resolved band and is not sensitive to local chemical environments. Raman bands in baseline corrected spectra were fitted with mixed Gaussian/Lorentzian functions. Curve fitting results were accepted when the residuals were minimized ($R^2 > 0.99$) and no negative bands were generated. Bands generated in the 600-1750 cm^{-1} spectral region were identified as primarily from proteins. Band positions were reproducible to ± 2 cm^{-1}. Raman band data (area, intensity, width) were imported to Excel and band intensity ratios were calculated. Intensity band ratios at 1080 cm^{-1}/1002 cm^{-1}, 1080 cm^{-1}/1125 cm^{-1}, 1235 cm^{-1}/1260 cm^{-1} (amide III), 1655 cm^{-1}/1448 cm^{-1} and 1670 cm^{-1}/1655 cm^{-1} (amide I) were used to evaluate protein content and structure. Raman spectra collected from drop edges were analyzed separately from Raman spectra collected from the drop center. After Raman data was analyzed for the entire patient cohort, radiograph scores were provided.

Band intensity ratios from 37 patients were plotted according to the patient's K/L score and compared in two ways: 1) -/ROA group vs. +/ROA group and 2) according to K/L scores 0-4. Raman data corresponding to patients with a K/L score of 3 and 4 were grouped together because there were only 2 patients in the K/L=4 group.

A nonparametric Wilcoxon rank sum analysis was used to test for significance in differences between -/ROA and +/ROA groups. The null hypothesis, that Raman band intensity ratios come from distributions with equal mean values, was rejected if $p<0.05$. Differences in Raman data corresponding with the individual K/L scores (K/L=0,1,2,3&4) were tested for significance using Kruskal-Wallis test for the major factor and multiple comparison was performed using the Kruskal-Wallis criterion to test for significance between mean ranks of groups.

In another test, MATLAB was used to preprocess all spectra from drop edges, perform baseline and background corrections, and generate a mean spectrum for each patient using only the spectra collected from SF drop edges. The mean spectra were input into an unsupervised K-means cluster analysis. Raman peaks were not fitted with Gaussian/Lorentzian functions for k-means clustering. Classification was based on pixel intensities corresponding to the 1080 cm^{-1}/1002 cm^{-1} and amide I ratios and we input two groups to correspond to the -/ROA and +/ROA groups.

Results

Light Microscopy of Dried SF Drops

All of the SF drops dried as a heterogeneous deposit. Drop deposition provided a coarse separation as shown by the low magnification microscope images in Figure 7.1. In Figure 1a, the dried drop contains two distinct regions. The outer edge gave a glassy appearance and the drop center contained fern shaped crystalline deposits. There are other distinguishable features, including cracks radiating from the drop center and interference patterns along the edges of some radial cracks. Most of the drops dried in the same general pattern and was independent of the SF volume aspirated from the patient and K/L score. We did observe some variety in the SF deposition pattern, as seen in Figure 7.1.

Approximately 1/3 of the drops (n=11) did not dry in the deposition pattern seen in Panel a. Alternative deposition patterns either lacked cracks near the drop edges (Panel b), were glassy throughout the drop (Panel c), or contained no fern shaped crystal deposits (Panel d). Analysis of microscope images for presence of radial cracks at the drop edge and fern-shaped crystals indicated a moderate correlation between OA severity and the presence of these drop features at low magnification (R^2=0.30). Detailed visual features are apparent upon higher magnification (10x) and these features may correlate more strongly with fluid viscosity or arthritis damage. Figure 7.2 shows representative images of synovial fluid drops at the drop edge (panels a and b) and in the drop center (panels c and d). Automated image analysis algorithms, similar to ones used for automated cell phenotype scoring, may also be able to find a stronger correlative trend between the visual features observed in SF drops and radiographic scoring.[51]

Separation of Synovial Fluid Components by Drop Deposition

Figure 7.3 shows a Raman spectrum collected from the drop edge (Spectrum a) and the drop center (Spectrum b) of one dried SF drop. Raman spectra collected from the drop edges are typical of proteins, as seen in spectrum A Figure 7.3. Raman transects collected in the drop center of 26 SF specimens contained additional bands at ~920 cm^{-1} and 1410 cm^{-1} and are highlighted in Figure 7.3.b. The 920 cm^{-1} and 1410 cm^{-1} bands were initially attributed to α-helical secondary structure and ionized carboxyl groups in SF proteins, and we hypothesized that more-soluble SF protein species had precipitated in the drop center.[41] Upon further examination, this initial hypothesis was determined to be null because it is inconsistent with principles of drop deposition and crystallization. During drop deposition, more soluble components precipitate in the drop center. These deposits found in the center of dried drops are usually crystalline because the more soluble material is often a small molecule with ionic side groups. Because the small molecules have a relatively longer time to precipitate, long-range ordered interactions can occur and the resulting precipitate is usually crystalline.

Assignment of the 920 cm^{-1} and the 1410 cm^{-1} bands provide conflicting interpretations as to the nature of the deposits found in the center of dried SF drops. The Raman band at

920 cm^{-1}, assigned to α-helix secondary structure, supports the hypothesis of smaller (<1000 Da) SF protein or peptide deposits in the center. However, the band at 1410 cm^{-1}, assigned to ionized carboxyl groups, contradicts the possibility of long-range ordered interactions because the anions would repel each other.

Another possibility was contamination of SF with specimen vial additives. An empty SCAT-1 specimen vial was examined by Raman spectroscopy and the contents were found to contain strong bands at ~920 cm^{-1} and 1410 cm^{-1}, which were identified as bands arising from PPACK. We concluded that PPACK had partially dissolved in SF. PPACK contamination of SF likely affected whole-fluid analyses such as viscosity. However, PPACK contamination of SF did not affect identification of chemical changes in SF using DDRS because of the coarse separation. Even with the PPACK contamination, DDRS was able to identify spectroscopic markers that can be associated with OA damage. The extent of PPACK contamination was measured by the intensities of the most prominent PPACK bands at ~920 cm^{-1} and 1410 cm^{-1} and the intensities did not depend on K/L score or SF volume. Principal components analysis of spectra collected from the drop center readily separated PPACK signal from SF signal and it is possible that potentially diagnostic information can be extracted from data collected from the center of dried SF drops.

Drop Deposition/Raman Spectroscopy of Dried SF Drops

Raman spectra of the dried SF drops also identified two primary regions within the drop, which supported our findings from the light microscopy studies. Spectra collected from the drop edges were comprised primarily of protein Raman bands, shown in Figure 7.3, which provided sufficient data for evaluating the physiochemical composition of human SF. Although Raman bands from glycosaminoglycans (GAGs) and lipids can overlap with some protein bands, they are relatively weak Raman scatterers and thus do not contribute significantly to the overall SF spectra. However, interaction of proteins with GAGs and lipids may still influence protein spectral features such as band position, width, height, or area. Previous studies of DDRS to examine solutions of proteins or biofluids found drop deposition spectra of proteins were similar to solution state or solid state spectra.[41, 43, 44] As expected, SF volume increased with OA damage, but the differences in SF volume were not statistically significant.

To interpret and eventually quantify changes to SF composition, bands were identified and assigned. Table 7.2 shows band assignments made for SF spectra, based from previous Raman studies of proteins and GAG's. [52-56] The most promising ratios were the 1080 cm^{-1}/1002 cm^{-1} ($p=8.1x10^{-8}$) and amide I band intensity ($p=5.6x10^{-5}$) ratios. Differences between -/ROA and +/ROA groups were significant for the 1080cm^{-1}/1002cm^{-1}. Figure 7.4 shows the 1080 cm^{-1}/1002 cm^{-1} and amide I band intensity ratio sorted by ± ROA group (panels a and b) and by K/L score (panels c and d). The 1080 cm^{-1}/1002 cm^{-1} (Panel a) intensity ratio increased in the +/ROA group and is evidence that the chemical environment of the protein backbone is altered with OA damage. The ratio of band intensities in the amide I envelope provide a marker of the relative abundance of disordered random coil secondary structure and ordered α-helix secondary structure. Higher amide I ratio observed in SF from patients in the +/ROA group indicate more disorder in protein secondary structure and provide further evidence of altered electrostatic interactions. Panels c and d of Figure 7.4 show that the mean ratio values begin to overlap in adjacent K/L score groups, but there is a moderate correlation of the ratios with K/L score ($R^2=0.31$ for amide I and $R^2=0.35$ for 1080 cm^{-1}/1002 cm^{-1} ratio). Kruskal-Wallis comparison showed significant differences in the mean rank between K/L groups 0-1, 0-2, 0-3 and 1-3 for the 1080 cm^{-1}/1002 cm^{-1} intensity ratio and between K/L groups 0-3, 1-3 and 2-3 for the Amide I ratio.

Preliminary application of automated data analysis techniques shows a good separation of data in the -/ROA and +/ROA groups. Figure 7.5 shows k-means clustering of pixel intensities corresponding to the 1080 cm^{-1}/1002 cm^{-1} and amide I ratios. The data indicate that simple pixel intensity ratios could be a good input for a k-means cluster analysis. Table 7.3 presents the sensitivity and selectivity of the cluster analysis. Based on the *a priori* power analysis, we chose to cluster the data into two groups because there was a higher power of analysis (84%). A mean spectrum for each SF specimen was calculated (N=37) and an unsupervised K-means cluster analysis was performed on the entire spectrum. The sensitivity (74%) and selectivity (71%) of the analysis is satisfactory for an unsupervised classification. We observed a high degree of misclassification when creating clusters based on bands that span a wide spectral range. Additional approaches, including principal components analysis, limiting the spectral window, or wavelet analysis, may improve sensitivity and classification rate. Using a support vector machine or principal components analysis with cluster analysis, or leave-one-out validation, are additional possible software approaches to improve classification rate.

Discussion

DDRS is compatible with standard clinical practice of SF collection. Small peptides used to preserve SF do not complicate Raman identification of chemical changes in SF because of the coarse separation provided by drop deposition. A peptide used as an anti-coagulant in the collection vials, PPACK, was localized in the drop center. Raman spectra collected from drop center had spectral contributions from dissolved SCAT-1 vial additives, as shown in Figure 7.3. In 2 SF specimens with the lowest aspiration volume (<0.5 ml), we observed extensive PPACK contamination so DDRS data from these two patients were removed from the final data set. The extent of PPACK contamination was measured by the intensities of its most prominent bands at ~920 cm^{-1} and 1410 cm^{-1}, which did not correlate with K/L score or SF volume.

Raman spectra collected from the edge of SF drops provided the most diagnostic information and showed significant differences between -/ROA (K/L=0-1) and +/ROA (K/L=2-4) groups. Comparison of Raman band intensity ratios from -/ROA and +/ROA groups show regions corresponding to protein backbone and amide linkages in the Raman spectra were sensitive to OA damage. Calculation of band intensity ratios from fitting peaks to SF spectra and cluster analysis indicate that the chemical environment is altered in SF collected from patients with radiological evidence of OA. Ratios of bands in the 1010-1150 cm^{-1} spectral region provided evidence for changes in the chemical environment of SF protein backbone. Raman spectra are sensitive to different protein amide linkages in secondary structures such as α-helix, β-sheet and random coil.[53] Increases in the amide I ratio is evidence of decreased relative amount in ordered protein secondary structure such as an α-helix. The trend toward reduced α-helical structure in SF proteins also indicates disruption in SF macromolecular interactions.

There are several possible mechanisms for an altered chemical environment in SF including: lower pH of diseased SF disrupts normal hydrogen bonding and partially denatures SF proteins, altered HA-protein interactions because HA depolymerizes in diseased SF, and/or more degraded type II collagen fragments in diseased SF.[8, 14] A recent proteomic analysis of SF found that cystatin A, an inhibitor of cysteine proteases, is elevated in healthy SF.[11] It is possible that, in diseased SF, cysteine proteases are more active and may disrupt normal SF electrostatic interactions.

Conclusions

The lack of a robust diagnostic of knee OA in its early stages, especially before structural alterations become apparent by conventional radiographs, continues to hinder research progress in both the etiologic and therapeutic arenas. The application of vibrational spectroscopy to examine chemical changes in SF may have diagnostic or prognostic value. In this study we employed a novel drop deposition/Raman spectroscopy protocol (DDRS) to examine SF from forty patients with clinical and radiographic evidence of knee OA. Analysis of light microscope images of dried drops revealed a coarse separation of the SF components, while measured Raman spectra provided information on protein secondary structure and content. We hypothesized that changes to the protein secondary structure could be used as general marker of chemical changes in SF and that these changes can be associated with radiographic scoring of knee damage. Raman data confirm our hypothesis and indicate a mechanism in which normal electrostatic interactions are disrupted in SF from damaged joints.

Raman spectra collected from dried synovial fluid drops were compared to x ray images collected from the affected knee joint. X ray scoring of radiological features using the K/L system provided an objective measurement of joint tissue damage because all of the patients exhibited clinical symptoms of OA such as effusion or pain. Comparison of SF Raman band intensity ratios from -/ROA and +/ROA groups support our hypothesis. We observed significant differences between Raman spectra of SF in -/ROA and +/ROA groups and showed trends toward a measurement that moderately correlates to individual K/L scores. The DDRS method can provide a “yes/no” classification of OA damage based on calculation of band intensity ratios or use of cluster analysis. Raman band intensity ratios indicate a possible trend toward correlation of the amide I or 1080 cm^{-1}/1002 cm^{-1} ratio with K/L score. We expect that expanded clinical studies will provide further discrimination between -/ROA and +/ROA groups, and possibly between adjacent K/L scores. Furthermore, it is also possible that DDRS of SF has value as a predictive measurement and this hypothesis will also be tested in longitudinal studies.

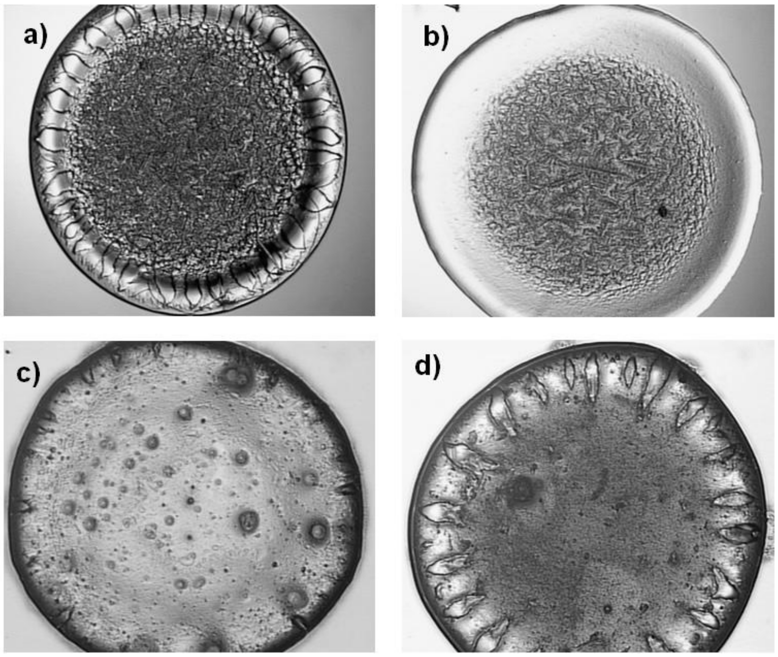

Figure 7.1: Microscope images of human synovial fluid (SF) dried drops at low magnification show a heterogeneous deposit.

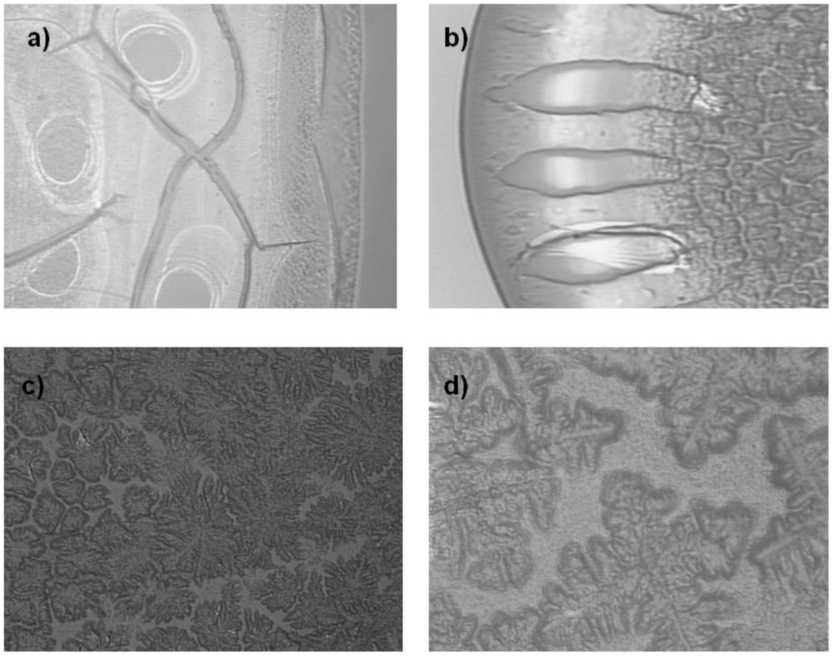

Figure 7.2: Higher magnification microscope images of SF drops reveal visual features such as accumulation of thin films and full-thickness cracking or shallow radial cracking (Panels a and b). Fern-shaped crystalline deposits were localized in the drop center (Panels c and d).

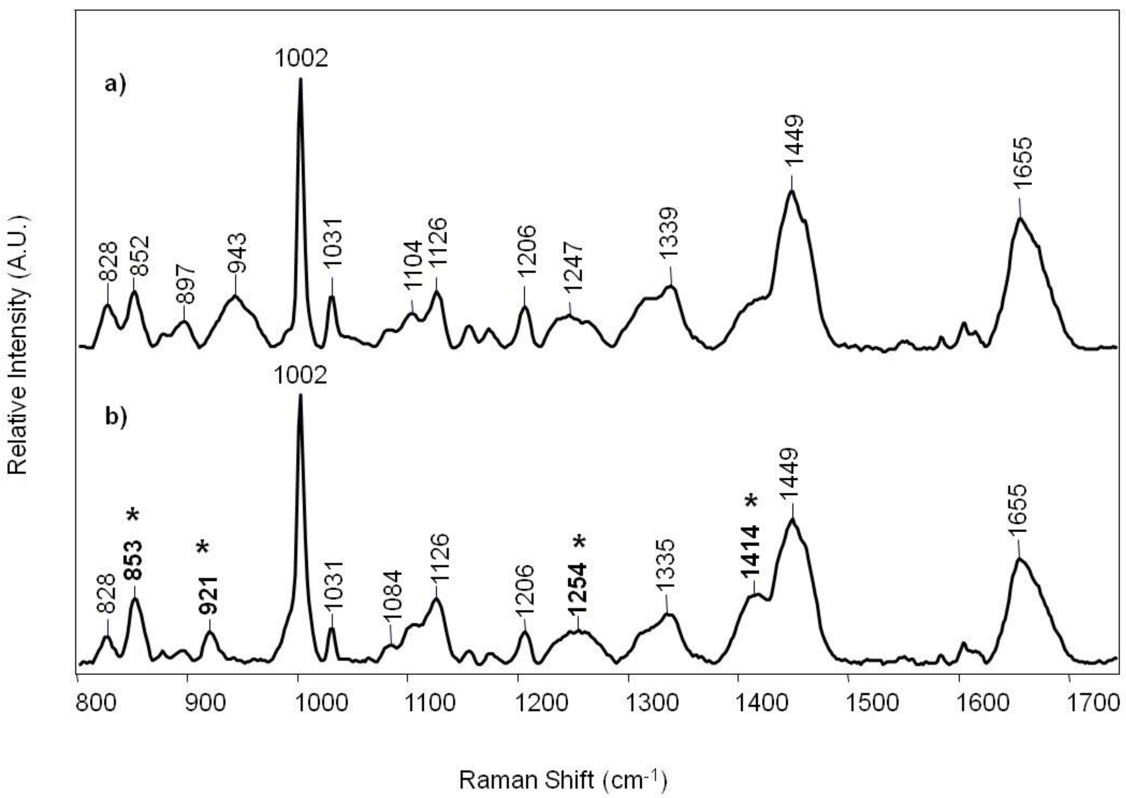

Figure 7.3: Raman spectra collected from the drop edge (a) and the drop center (b) indicated a coarse separation of SF from vial additives.

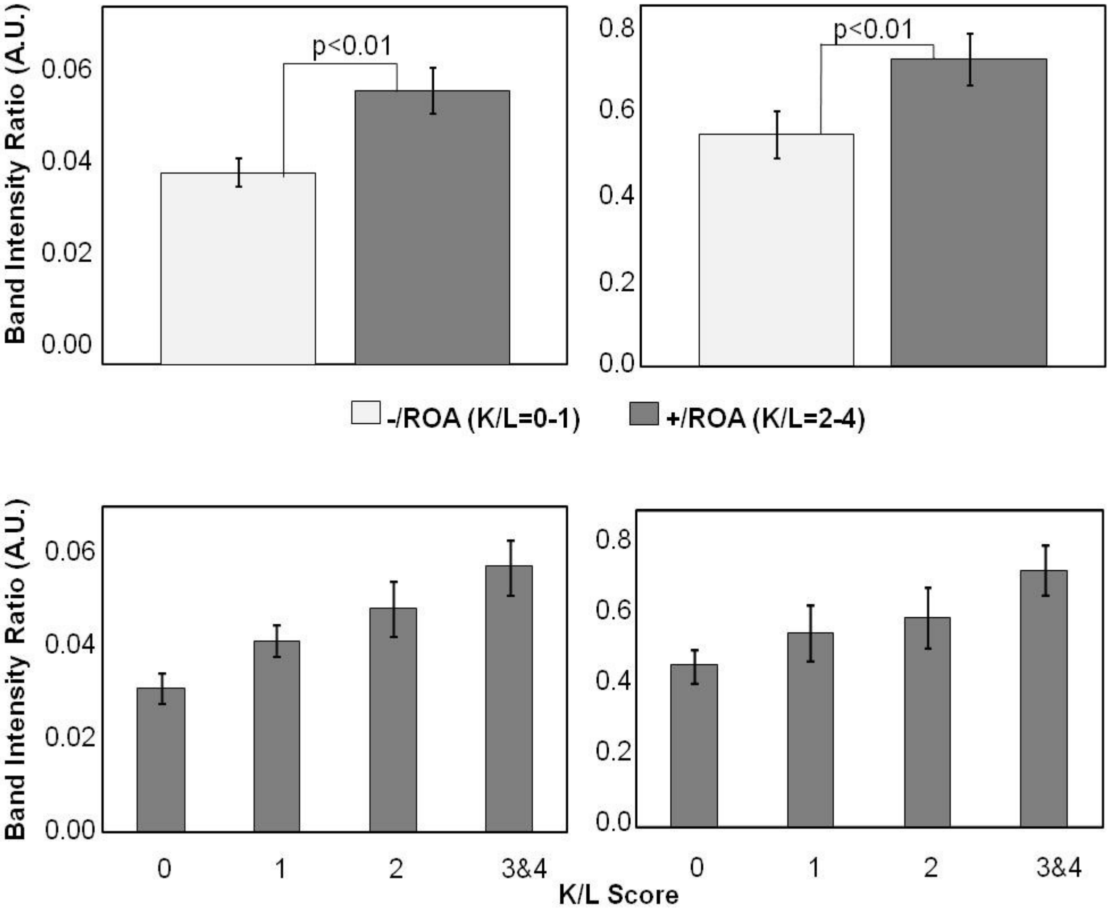

Figure 7.4: Comparison of two band intensity ratios for -/ROA (K/L=0-1) and +/ROA (K/L=2-4) groups found significant differences ($p<0.01$) in the +/ROA group. Error bars show the 95% confidence interval. The 1080 cm^{-1}/1002 cm^{-1} (Panel a) and amide I (Panel b) band intensity ratios indicated alterations to protein chemical structure. When these ratios are sorted by K/L score (1080 cm^{-1}/1002 cm^{-1} , Panel c and amide I, Panel d) these differences begin to diminish but moderate correlative trends (0.31 and 0.35, respectively) were still observed.

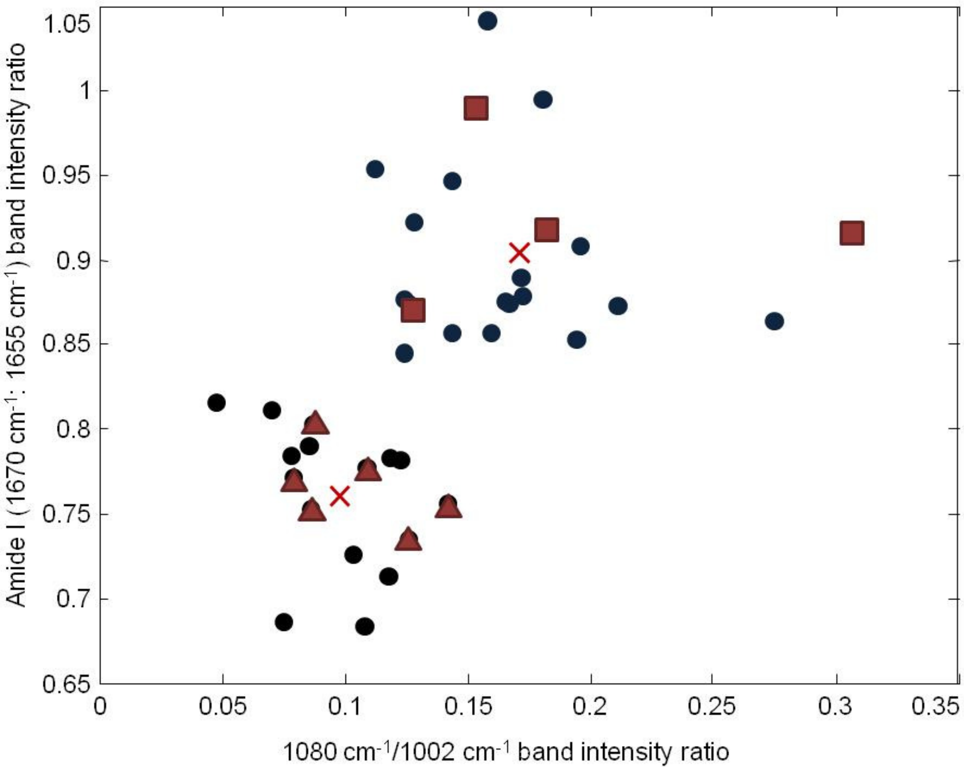

Figure 7.5: In another analysis, unsupervised K-means cluster analysis was performed on data collected from the edges of dried SF drops. Closed circles represent correct classification, closed triangles represent false negative and closed squares represent false positives.

K/L Score	Average Age (yrs.)	Age Range (yrs.)	# Male	# Female
0	44	19-66	7	1
1	53	31-72	7	2
2	59	43-78	5	3
3&4	59	42-69	10	5

Table 7.1: Patient demographics in the drop deposition/Raman spectroscopy study.

Raman Shift (cm^{-1})	Band Assignment	Component
895	C-C stretch	Protein
938	C-C stretch, α-helix	Protein
1002	Ring breathing	Protein
1080	C-N, C-C stretch	Protein
1125	C-C, C-OH, C-N stretch	Protein
	C-O-C glycosidic linkage	Protein
1235	Amide III, random coil	Protein
1260	Amide III, α-helix	Protein
1340	CH_2/CH_3 wag	Protein
1446	CH_2/CH_3 deformation	Organic content
1655	Amide I, α-helix	Protein
1670	Amide I, random coil	Protein
1687	Amide I, β-sheet	Protein

Table 7.2: Raman band assignments of SF drops were based on literature reports of proteins and biological specimens.

	-/ROA	**+/ROA**
K/L=0-1	10	4
K/L=2-4	6	17

Sensitivity: 74%

Selectivity: 71%

Positive Predictive Value: 81%

Negative Predictive Value: 63%

Table 7.3: Results from unsupervised K-means cluster analysis of mean Raman spectra generated from each patient's synovial fluid (n=37).

References

1. Felson DT, Neogi T: **Osteoarthritis: Is it a disease of cartilage or of bone?** *Arthritis & Rheumatism* 2004, **50**(2):341-344.
2. Dieppe PA, Lohmander LS: **Pathogenesis and management of pain in osteoarthritis**. *The Lancet* 2005, **365**(9463):965-973.
3. Cowman MK, Matsuoka S: **Experimental approaches to hyaluronan structure**. *Carbohydrate Research* 2005, **340**(5):791-809.
4. Neumann A, Schinzel R, Palm D, Riederer P, Münch G: **High molecular weight hyaluronic acid inhibits advanced glycation endproduct-induced NF-kB activation and cytokine expression**. *FEBS Letters* 1999, **453**(3):283-287.
5. Wang CT, Lin YT, Chiang BL, Lin YH, Hou SM: **High molecular weight hyaluronic acid down-regulates the gene expression of osteoarthritis-associated cytokines and enzymes in fibroblast-like synoviocytes from patients with early osteoarthritis**. *Osteoarthritis and Cartilage* 2006, **14**(12):1237-1247.
6. Brannan SR, Jerrard DA: **Synovial fluid analysis**. *Journal of Emergency Medicine* 2006, **30**(3):331-339.
7. Larkin JG, Lowe GDO, Sturrock RD, Forbes CD: **The Correlation of Clinical Assessment of Synovial Fluid with its Measured Viscosity**. *Rheumatology* 1984, **23**(3):195-197.
8. Jebens EH, Monk-Jones ME: **On the Viscosity and pH of Synovial Fluid and the pH of Blood**. *Journal of Bone and Joint Surgery* 1959, **41B**(2):388-400.
9. Jay GD, Torres JR, Rhee DK, Helminen HJ, Hytinnen MM, Cha C-J, Elsaid K, Kim K-S, Cui Y, Warman ML: **Association between friction and wear in diarthrodial joints lacking lubricin**. *Arthritis & Rheumatism* 2007, **56**(11):3662-3669.
10. Williams F, Spector T: **Biomarkers in osteoarthritis**. *Arthritis Research & Therapy* 2008, **10**(1):101.
11. Gobezie R, Kho A, Krastins B, Sarracino DA, Thornhill TS, Chase M, Millett PJ, Lee DM: **High Abundance Synovial Fluid Proteome: Distinct Profiles in Health and Osteoarthritis**. *Arthritis Research and Therapy* 2007, **9**(2):R36.
12. Bauer DC, Hunter DJ, Abramson SB, Attur M, Corr M, Felson D, Heinegard D, Jordan JM, Kepler TB, Lane NE: **Classification of osteoarthritis biomarkers: a proposed approach**. *Osteoarthritis and Cartilage* 2006, **14**(8):723-727.
13. Sharif M, Granell R, Johansen J, Clarke S, Elson C, Kirwan JR: **Serum cartilage oligomeric matrix protein and other bio-marker profiles in tibiofemoral and patellofemoral osteoarthritis of the knee**. *Rheumatology (Oxford)* 2006, **45**:522 - 526.
14. Lindhorst E, Wachsmuth L, Kimmig N, Raiss R, Aigner T, Atley L, Eyre D: **Increase in degraded collagen type II in synovial fluid early in the rabbit meniscectomy model of osteoarthritis**. *Osteoarthritis and Cartilage* 2005, **13**(2):139-145.
15. Takahashi M, Naito K, Abe M, Sawada T, Nagano A: **Relationship between radiographic grading of osteoarthritis and the biochemical markers for arthritis in knee osteoarthritis**. *Arthritis Res Ther* 2004, **6**(3):R208 - R212.

16. DeGroot J, Bank RA, Tchetverikov I, Verzijl N, TeKoppele JM: **Molecular markers for osteoarthritis: the road ahead**. *Current Opinion in Rheumatology* 2002, **14**:585-589.

17. Yavorskyy A, Hernandez-Santana A, McCarthy G, McMahon G: **Detection of calcium phosphate crystals in the joint fluid of patients with osteoarthritis - analytical approaches and challenges**. *The Analyst* 2008, **133**(3):302-318.

18. Schmidt-Rohlfing B, Thomsen M, Niedhart C, Wirtz DC, Schneider U: **Correlation of bone and cartilage markers in the synovial fluid with the degree of osteoarthritis**. *Rheumatology International* 2002, **21**:193-199.

19. Praest BM, Greiling H, Kock R: **Assay of synovial fluid parameters: hyaluronan concentration as a potential marker for joint diseases**. *Clinica Chimica Acta* 2003, **266**:117-128.

20. Wilson R, Bateman JF: **Cartilage proteomics: Challenges, solutions and recent advances**. *Proteomics-Clinical Applications* 2008, **2**(2):251-263.

21. Nalbant S, Martinez JAM, Kitumnuaypong T, Clayburne G, Sieck M, Schumacher JHR: **Synovial fluid features and their relations to osteoarthritis severity: new findings from sequential studies**. *Osteoarthritis and Cartilage* 2003, **11**(1):50-54.

22. Hunter DJ, Li J, LaValley M, Bauer DC, Nevitt M, DeGroot J, Poole R, Eyre D, Guermazi A, Gale D *et al*: **Cartilage markers and their association with cartilage loss on magnetic resonance imaging in knee osteoarthritis: the Boston Osteoarthritis Knee Study**. *Arthritis Res Ther* 2007, **9**:R108-R116.

23. Marini S, Francesco Fasciglione G, Monteleone G, Maiotti M, Tarantino U, Coletta M: **A correlation between knee cartilage degradation observed by arthroscopy and synovial proteinases activities**. *Clinical Biochemistry* 2003, **36**(4):295-304.

24. Jackson M, Mantsch HH: **Pathology by Infrared and Raman Spectroscopy**. New York: John Wiley and Sons LTD; 2002.

25. Rolfe P: **In vivo near-infrared spectroscopy**. *Annual Review of Biomedical Engineering* 2000, **2**(1):715-754.

26. Potter K, Kidder LH, Levin IW, Lewis EN, Spencer RG: **Imaging of collagen and proteoglycan in cartilage sections using Fourier transform infrared spectral imaging**. *Arthritis & Rheumatism* 2001, **44**(4):846-855.

27. Bi X, Yang X, Bostrom MPG, Camacho NP: **Fourier transform infrared imaging spectroscopy investigations in the pathogenesis and repair of cartilage**. *Biochimica et Biophysica Acta (BBA) - Biomembranes* 2006, **1758**(7):934-941.

28. Miller LM, Carlson CS, Carr GL, Chance MR: **A method for examining the chemical basis for bone disease: synchrotron infrared microspectroscopy**. *Cellular and Molecular Biology (Noisy le Grand)* 1998, **44**(1):117-127.

29. Ueno M, Shibata A, Yasui S, Yasuda K, Ohsaki K: **A proposal on the hard tissue remineralization in osteoarthritis of the knee joint investigated by FT-IR spectrometry**. *Cellular and Molecular Biology* 2003, **49**(4):613-619.

30. Dehring KA, Crane NJ, Smukler AR, McHugh JB, Roessler BJ, Morris MD: **Identifying Chemical Changes in Subchondral Bone Taken from Murine**

Knee Joints Using Raman Spectroscopy. *Applied Spectroscopy* 2006, **60**(10):1134-1141.

31. Shaw RA, Kotowich S, Eysel HH, Jackson M, Thomson GTD, Mantsch HH: **Arthritis diagnosis based upon the near-infrared spectrum of synovial fluid**. *Rheumatology International* 1995, **15**(4):159-165.
32. Eysel HH, Jackson M, Nikulin A, Somorjai RL, Thomson GTD, Mantsch HH: **A Novel Diagnostic Test for Arthritis: Multivariate Analysis of Infrared Spectra of Synovial Fluid**. *Biospectroscopy* 1997, **3**(2):161-167.
33. Ziegler CM, Kircher P, Hassfeld S: **Analysis of Temporomandibular Joint Synovial Fluid Using Fourier-Transform/Infrared Spectroscopy**. *Journal of Oral and Maxillofacial Surgery* 2002, **60**(11):1302-1306.
34. Cui J, Loewy J, Kendall EJ: **Automated search for arthritic patterns in infrared spectra of synovial fluid using adaptive wavelets and fuzzy C-Means analysis**. *IEEE Transactions on Biomedical Engineering* 2006, **53**(5):800-809.
35. Deegan RD, Bakajin O, Dupont TF, Huber G, Nagel SR, Witten TA: **Capillary flow as the cause of ring stains from dried liquid drops**. *Nature* 1997, **389**(6653):827-829.
36. Yakhno TA, Yakhno VG, Sanin AG, Sanina OA, Pelyushenko AS, Egorova NA, Terentiev IG, Smetanina SV, Korochkina OV, Yashukova EV: **The informative-capacity phenomenon of drying drops**. *Engineering in Medicine and Biology Magazine, IEEE* 2005, **24**(2):96-104.
37. Yakhno T, Sedova O, Sanin A, Pelyushenko A: **On the existence of regular structures in liquid human blood serum (plasma) and phase transitions in the course of its drying**. *Technical Physics* 2003, **48**(4):399-403.
38. Filik J, Stone N: **Drop coating deposition Raman spectroscopy of protein mixtures**. *The Analyst* 2007, **132**:544-550.
39. Zhang D, Xie Y, Mrozek MF, Ortiz C, Davisson VJ, Ben-Amotz D: **Raman Detection of Proteomic Analytes**. *Anal Chem* 2003, **75**(21):5703-5709.
40. Filik J, Stone N: **Raman point mapping of tear ferning patterns**. In: *Biomedical Optical Spectroscopy: 2008; San Jose, CA, USA*: SPIE; 2008: 685309-685306.
41. Esmonde-White KA, Mandair GS, Raaii F, Roessler BJ, Morris MD: **Raman spectroscopy of dried synovial fluid droplets as a rapid diagnostic for knee joint damage**. In: *Biomedical Optical Spectroscopy: 2008; San Jose, CA, USA*: SPIE; 2008: 68530Y-68539.
42. Zhang D, Mrozek MF, Xie Y, Ben-Amotz D: **Chemical Segregation and Reduction of Raman Background Interference Using Drop Coating Deposition**. *Applied Spectroscopy* 2004, **58**(8):929-933.
43. Ortiz C, Zhang D, Xie Y, Ribbe AE, Ben-Amotz D: **Validation of the drop coating deposition Raman method for protein analysis**. *Analytical Biochemistry* 2006, **353**(2):157-166.
44. Kopecký JV, Baumruk V: **Structure of the ring in drop coating deposited proteins and its implication for Raman spectroscopy of biomolecules**. *Vibrational Spectroscopy* 2006, **42**(2):184-187.

45. Esmonde-White KA, Le Clair SV, Roessler BJ, Morris MD: **Effect of Conformation and Drop Properties on Surface-Enhanced Raman Spectroscopy of Dried Biopolymer Drops**. *Appl Spectrosc* 2008, **62**(5):503-511.

46. Altman RD, Hochberg M, Murphy WA, Jr., Wolfe F, Lequesne M: **Atlas of individual radiographic features in osteoarthritis**. *Osteoarthritis and Cartilage* 1995, **3 Suppl A**:3-70.

47. Altman R, Asch E, Bloch D, Bole G, Borenstein D, Brandt K, Christy W, Cooke TD, Greenwald R, Hochberg M *et al*: **Development of criteria for the classification and reporting of osteoarthritis. Classification of osteoarthritis of the knee. Diagnostic and Therapeutic Criteria Committee of the American Rheumatism Association**. *Arthritis Rheum* 1986, **29**(8):1039-1049.

48. Kellgren JH, Lawrence JS (eds.): **Atlas of Standard Radiographs**. Oxford, UK: Blackwell Scientific; 1963.

49. Kellgren JH, Lawrence JS: **Radiological Assessment of Osteo-Arthrosis**. *Ann Rheum Dis* 1957, **16**(4):494-502.

50. Hoeksma HL, Dekker J, Ronday HK, Heering A, Lubbe NVD, Vel C, Breedveld FC, Ende CHMVD: **Comparison of manual therapy and exercise therapy in osteoarthritis of the hip: A randomized clinical trial**. *Arthritis Care & Research* 2004, **51**(5):722-729.

51. Carpenter AE: **Image-based chemical screening**. *Nat Chem Biol* 2007, **3**(8):461-465.

52. Sane SU, Cramer SM, Przybycien TM: **A Holistic Approach to Protein Secondary Structure Characterization Using Amide I Band Raman Spectroscopy**. *Analytical Biochemistry* 1999, **269**(2):255-272.

53. Pelton JT, McLean LR: **Spectroscopic Methods for Analysis of Protein Secondary Structure**. *Analytical Biochemistry* 2000, **277**:167-176.

54. Chourpa I, Ducel V, Richard J, Dubois P, Boury F: **Conformational Modifications of α– Gliadin and Globulin Proteins upon Complex Coacervates Formation with Gum Arabic as Studied by Raman Microspectroscopy**. *Biomacromolecules* 2006, **7**(9):2616-2623.

55. Lin VJC, Koenig JL: **Raman studies of bovine serum albumin**. *Biopolymers* 1976, **15**(1):203-218.

56. Edwards HGM, Russell NC, Weinstein R, Wynn-Williams DD: **Fourier transform Raman spectroscopic study of fungi**. *Journal Of Raman Spectroscopy* 1995, **26**(8-9):911-916.

Chapter 8

Surface-Enhanced Raman Spectroscopy Detection of Hyaluronic Acid: A Potential Biomarker for Osteoarthritis

Introduction

Osteoarthritis (OA), the progressive degeneration of synovial joints affects more than 20 million adults in the United States and is expected to rise to 70 million by 2030. Symptomatic knee OA is one of the most prevalent form of arthritis and affects 6 % of adults 30 years or older.[1] Current methods of detecting OA often rely upon physical examination and radiographic evaluation with follow-up times of about two years to establish the level of disease progression.[1, 2] Chemical, biological and viscoelastic properties of synovial fluid often precede or accompany radiographic evidence of joint damage. These synovial fluid markers may provide the first indications of early-stage OA progression. Additionally, synovial fluid markers may be used to monitor the efficacy of therapeutic interventions.

Evaluating chemical structure of sulfated or unsulfated glycosaminoglycans (GAGs) in synovial fluid or cartilage has received considerable attention in recent years as a potential biomarker of early-stage OA.[3-5] Inflammation of the synovial membrane leads to the enhanced secretion of pathological synovial fluid. An expression of altered synovial fluid is a lower abundance and lower molecular weight of the unsulfated GAG hyaluronic acid (HA) compared to normal synovial fluids.[4, 6] These changes are undesirable as HA is primarily responsible for the viscoelastic properties of synovial fluid and aids in the lubrication and protection of articular cartilage from mechanical injury. The loss of HA concentration is caused by infiltration of the plasma fluid and proteins into the synovial fluid, whereas the molecular size reduction is caused by abnormal metabolic processes occurring within the inflamed synovial structures.[4, 7, 8]

The depolymerization of hyaluronic acid into low molecular weight fragments results in decreased viscoelasticity of synovial fluid. Current techniques for measuring hyaluronic acid, such as chromatography, rheology or dynamic light scattering require large sample volumes and extensive sample preparation. We hypothesized that Raman spectroscopy could be used to examine hyaluronic acid in solution and in synovial fluid. Raman spectra of the HA polymer could be obtained using low volume and minimal sample preparation and the measured spectrum could correlate to the entanglement properties of HA.

Raman spectroscopy is a powerful tool for examining subtle changes in chemical structure or composition. The field of biomedical Raman spectroscopy has grown substantially in the past 10 years, as many applications using Raman to examine cells, tissues, and biofluids have been reported.[9-12] Surface-enhanced Raman spectroscopy has also been used to examine biological specimens such as biofilms, bacteria, or cancerous tissue.[13-17] Despite the large enhancement of Raman signal, the potential of SERS has not yet been fully realized because of the experimental difficulties in achieving reproducible signal enhancements.[18, 19] Recently, commercially available SERS substrates produced by semiconductor nanofabrication techniques have overcome the limitation in reproducibility of enhancement on substrate surfaces.[20, 21] These substrates are based on silicon photonic crystals, which are etched with void architectures and coated with a layer of gold producing a SERS-active surface.

Drop deposition is a seemingly simple phenomenon that has recently gained considerable attention in the biomedical and pharmaceutical fields as a way to rapidly measure protein-protein interactions or generate single-crystals for a polymorph crystal screen. The formation of a dried drop onto a solid surface is influenced primarily by capillary flow, and can be affected by variables such as substrate material, analyte concentration, and speed of evaporation.[22-24] Because most drop deposition studies are performed on flat substrates, such as silicon, mica or Teflon©, light microscopy is frequently used to follow solvent evaporation and examine the morphology of the resulting drop. The dimensions of the substrates are typically compatible with other microscope-based analytical tools such as cross-polarized light microscopy, fluorescence or microspectroscopy. Ben-Amotz et al recently demonstrated the use of normal Raman spectroscopy to detect proteins from dried drops at concentrations as low as 1 μM in the presence of a buffer.[25]

Because the ring formation can function simultaneously as both a low resolution separation and a preconcentration method, it can help overcome the well-known limitations of fluorescence interference and high sample concentration requirements that are inherent in normal Raman spectroscopy. However, normal Raman spectroscopic detection of rings may not be feasible for weakly scattering biomolecules, such as HA. Drying HA drops using the drop deposition technique on gold-coated SERS substrates can overcome this problem. Both the preconcentration effect of a ring shaped deposition and the surface-enhancement offers an additional improvement in the Raman signal intensity of weakly scattering HA biomolecules.

We explored the feasibility of using these gold-coated SERS substrates for the rapid and reproducible detection of HA at clinically useful levels in biofluids such as synovial fluid or plasma. We hypothesized that surface-enhanced Raman spectroscopy (SERS) can be used for evaluating the chemical structure of HA as a biomarker for pathological synovial fluid secretions. In our study, we deposited a small volume of liquid containing HA onto a SERS substrate and allowed the drop to dry naturally under ambient conditions. We tested the technique on aqueous HA solutions and synthetic models of synovial fluid before applying it to human synovial fluid specimens.

Materials and Methods

Raman Spectroscopy

Raman spectra were collected with a Raman microprobe, optimized for collection of near-infrared signal, described elsewhere.[26] The system consists of a 400 mW 785 nm laser (Invictus, Kaiser Optical Systems, Inc., Ann Arbor, MI) and an epi-illumination microscope (BH-2, Olympus, Center Valley, PA). Laser light was coupled with a 1.0 neutral density filter, Powell lens (StockerYale, Salem, NH), and lined-focused through a 20X/0.75 NA Fluor objective (Carl Zeiss, Inc., Thornwood, NY). A laser power output of ~8 mW was achieved at the objective. Raman scatter was collected using an *f*/1.8 axial transmissive spectrograph (HoloSpec, Kaiser Optical Systems, Inc., Ann Arbor, MI) and detected using a back-thinned deep depletion CCD camera (Andor Technologies, Belfast, Ireland). Raman spectra were acquired for 60-120 seconds. Wavenumber calibration, correction for variation in CCD response, dark current and image curvature were performed in Matlab 6.1 (The Math Works, Natick, MA) using built-in and locally-written scripts. Data preprocessing in Grams/AI 7.01 software (ThermoGalactic, Waltham, MA) consisted of user-input, multi-point baseline correction and (if applicable) correction for contributions from the substrate. Low magnification light microscope images of dried drops were collected using either a 5X/0.25 NA Fluor (Carl Zeiss, Inc., Thornwood, NY) or a 10X/0.50 Fluor (Carl Zeiss, Inc., Thornwood, NY) objective.

Materials

Rooster comb hyaluronic acid (HA, ~2000 kDa), bovine serum albumin (BSA), γ-globulins, and human plasma (*ca.,* 72 % albumin and 15 % γ-globulin) were obtained from Sigma-Aldrich (St. Louis, MO) and used as received. All other used reagents and solvents were of analytical grade.

Preparation of Standard Solutions

Aqueous HA standards (4-0.25 mg/mL) were prepared by dilution of a 6-8 mg/mL HA stock solution in water. Artificial synovial fluid standards (ASF) containing human plasma was prepared by mixing 25 μL HA standards (4-0.25 mg/mL) in 25 μL solutions containing 11.5 μL deionized water and 13.5 μL human plasma, giving final HA, albumin, and globulin concentrations of approximately 2.0-0.125, 11.8, and 3.8 mg/mL, respectively. A human plasma solution (27% v/v in deionized water) was prepared as an experimental control at the same albumin and γ-globulin concentrations. All solutions were stored at -4 °C.

Precipitation of hyaluronic acid from artificial synovial fluid

Precipitation of proteins was tested in artificial synovial fluid. Plasma, as a control fluid, was also tested. A 50 µL aliquot of ASF or plasma were transferred to 500 µL centrifuge tubes, followed by an equivalent volume of 10 % trichloroacetic acid (TCA) solution. The centrifuge tubes were vortexed for 30 seconds, incubated at -4 °C overnight, and centrifuged at 9,500 rpm for 10 min. The clear supernatant layer was extracted and stored at -4 °C.

Another approach was to isolate HA from a mixture of proteins and HA. We used the method of Kvam et al., to purify HA from synovial fluid using additions of chloroform and phenol-saturated buffer.[27] An aqueous mixture of HA (2 mg/mL), bovine serum albumin (11.8 mg/mL) and γ-globulin was dissolved in pH 7.4 PBS and stirred at room temperature for 1-2 hours. HA-protein mixtures can be either diluted 1:3 (%v/v) with pH 7.4 PBS or remain undiluted and then the HA was extracted using the following steps. A) The sample was extracted in a 1:1 (%v/v) mixture of phenol-saturated buffer, and centrifuged for 3 minutes at 5000 rpm. B) The upper phase was extracted with 2:1:1 (%v/v/v) phenol-saturated buffer: chloroform and centrifuged for 2 minutes at 5000 rpm. C) The aqueous phase was then extracted with 1:1 (%v/v) chloroform and centrifuged for 2 minutes at 5000 rpm. A 0.2 µL aliquot of the final HA solution was deposited onto a Klarite substrate within 1 hour of the final preparation step. Extraction protocols were tested against with two controls a) proteins-only solution that has also been run through the same phenol-chloroform extraction procedure and b) mixture of HA and proteins that was untreated.

SERS analysis protocols

For all fluids examined, 0.2-0.3 µL of each solution were deposited onto Klarite™ SERS Substrates (Mesophotonics Ltd, Hampshire, UK) and left to air dry at room temperature for 30 min. Raman spectra of the ring-like deposits were acquired with 60 or 120 second integration times and ~8 mW laser power. Normal Raman spectra of a 0.5 mg/mL HA deposits dried on bare gold and fused silica slides were acquired for 120 seconds. The resulting Raman spectra were examined for characteristic HA bands between 800 and 1700 cm^{-1}.

Results

Raman bands of HA are shown in Table 1.2. assignments were based on literature reports of the spectra of aqueous and solid HA.[28, 29] The major bands of HA are found at 899, 945, 1050, 1130 and 1410 cm^{-1} and were used to identify HA in artificial synovial fluid (ASF) preparations. Noise in the measured Raman spectra limited the reproducibility of band positions to ± 2 cm^{-1}.

The effect of substrate surface and HA concentration on drop shape was studied on fused silica, bare gold, and a SERS substrate. A consistent observation throughout these studies was the asymmetric ring shape when drops dried on the SERS substrate. As seen in Figure 8.1.a, the drop shape is similar to an octagon. A similar drop shape was observed when aqueous HA solutions at various concentrations (0.25-6 mg/ml) are deposited onto the SERS substrate. In addition to the non-spherical shape of the drop, asymmetric concentric rings at the drop edge (Figure 8.1.b) were observed when highly concentrated aqueous HA solutions were deposited on the SERS substrate. In Chapter 9 we discuss how concentration affects deposition patterns and SERS spectra of HA.

Figure 8.2 shows spectra of a 0.5 mg/ml aqueous HA solution evaporated onto fused silica (a), bare gold (b), and a gold-coated SERS substrate (c). It is clear from Figure 8.2 that normal (unenhanced) Raman spectroscopy is not possible at low concentrations of HA in solution, even using signal integration times as long as 120 seconds. Raman bands from HA are clearly observed on the SERS substrate, even with an integration time of 60 seconds. The positions of surface-enhanced Raman bands of HA are in good agreement with literature values for bands of the normal Raman spectrum of the molecule.

Several methods were evaluated for reduction of spectral interference from proteins. We examined filtration, drop deposition, and ultracentrifugation methods to separate protein from HA using protocols from the published literature.[30, 31] We concluded that these techniques do not adequately reduce the protein signal, which provides evidence for our hypothesis that hyaluronic acid binds non-specifically with synovial fluid proteins such as albumin or γ-globulin. By contrast, albumin and γ-globulin were almost completely removed from ASF using either the TCA or phenol/chloroform treatment. As shown in Figure 8.3, the intense phenylalanine ring breathing band at ~1000 cm^{-1} is reduced to intensities similar to or lower than the intensities of the most intense and characteristic HA bands.

Discussion

The use of a SERS substrate enables rapid collection of HA spectra at clinically relevant concentrations. Even at higher concentrations, attempts to collect unenhanced Raman spectra were unsuccessful. We did not observe HA bands when aqueous solutions at 6 mg/ml, 3 mg/ml or 0.5 mg/ml were deposited on fused silica or bare gold, even at integration times of 120 seconds. Previously reported detection limits for HA solutions by normal Raman spectroscopy are in the 40-50 mg/ml range. The limit of detection is reduced by at least two orders of magnitude. The current detection limit of about 0.5 mg/mL is within synovial fluid HA levels (0.25-3 mg/mL) observed in osteoarthritis patients.[27] By contrast, serum HA levels that are correlated with future (approximately 2 years) joint space narrowing are much lower (30.2 ± 19.6 ng/mL).[32] To reach such levels a more efficient illumination scheme or an evaporation protocol that produces smaller ring diameters will be need to be examined. The relatively high HA detection limit observed in our studies may be a consequence of using the drop evaporation technique. As HA concentration is reduced the ring of precipitated HA becomes narrower. Because the drop edge is illuminated by our line-focused laser and most of the deposited HA is not interrogated, the detection limit is relatively high.

We observed that the initial HA concentration and surface geometry of the substrate affected the pattern of the dried HA drop. Previous studies have demonstrated that concentric ring formation is concentration-dependent.[22] We hypothesize that the presence of concentric rings is related to entanglement of the HA polymer chains because the concentric rings are not prominent at concentrations below 2 mg/ml. The presence of these concentric rings does not prevent the collection of HA Raman spectra, and may provide additional information about the size distribution of the polysaccharide. Deposition of polygonal rather than circular rings appears to be a result of the geometry of the SERS substrate. Circular rings were observed when 0.2µl drops of the same HA solutions were deposited on fused silica slides or the bare gold portions of SERS substrates.

Several techniques were used to separate HA from proteins. Microscopy images and SERS spectra of dried ASF drops showed that drop deposition alone is inadequate for separation of HA from the proteins present in synovial fluid. Light microscope images of the deposits from untreated artificial synovial fluid showed a few concentric rings at the edges of the drops. SERS spectra showed that protein preferentially adsorbed onto the SERS surface. Small molecule impurities were still segregated in the drop center. We observed similar protein bands in SERS spectra of dried canine synovial fluid and canine plasma drops (data not shown). These experiments in artificial synovial fluid indicated non-specific binding of HA to albumin.[33] Even at higher starting HA concentrations (2 mg/ml) in untreated artificial synovial fluid, Raman spectra taken anywhere in the deposit are dominated by protein bands that obscure any HA signal.

Chemical pretreatment of ASF was necessary to reduce protein signal in dried ASF drops. Trichloroacetic acid (TCA) protein precipitation followed by ultracentrifugation was successful in reducing the protein concentration in ASF. However, we were not able to clearly identify HA in spectra collected from dried drops of ASF treated with TCA. Although microscope images and Raman spectroscopy showed TCA had primarily localized in the center of the dried drop, Raman spectra showed that some TCA co-precipitated with HA in the drop edges. Moreover, we observed overlap of TCA bands with characteristic HA bands at 899 and 945 cm^{-1}. As shown in Figure 8.3.a, ASF after TCA treatment contained primarily bands from TCA with possible contributions from HA. A broad TCA band is observed between 830-860 cm^{-1} and other bands are found at ~ 945 cm^{-1} and 1365 cm^{-1}.

Our results indicated that the phenol/chloroform protocol is better suited for isolation of HA than the TCA protocol. Raman spectra of HA with good signal-to-noise were demonstrated for HA at clinically relevant HA concentrations (final HA concentration ~0.66-2 mg/mL). We observed non-overlapping phenol solvent bands in SERS spectra taken from dried drops of the final HA isolation. A simple spectral subtraction of phenol solvent revealed HA bands. As shown in Figure 8.3.b, HA bands can be easily observed at 899, 1040, and 1117 cm^{-1} after treatment with phenol/chloroform. Protein signal was completely eliminated. Preliminary application of the phenol-chloroform treatment to synthetic synovial fluid indicates that dilution of untreated synovial fluid with phosphate buffer is also necessary in order to reduce fluid viscosity.

The phenol-chloroform method was used to isolate HA from human synovial fluid specimens. Prior to HA extraction by phenol/chloroform, synovial fluid specimens were diluted with phosphate buffered saline (pH 7.4). HA-protein interactions were reduced by addition of pronase E and protease K to diluted synovial fluid (stirred with synovial fluid specimens for 15 minutes at room temperature). Samples were then passed through a teflon filter to remove synovial fluid lipids. HA was then extracted using additions of phenol/chloroform. SERS spectra were collected from aliquots kept after the filtration step and the final product. Similar to Kvam's study, we found residual phenol solvent in the final product. [27] SERS spectra indicated that HA was present synovial fluid after the filtration step as shown in Figure 8.4.a, but the extraction steps removed most traces of HA as shown in Figure 8.4.b. We suspect that the enzymatic pretreatment did not adequately reduce HA-protein interactions and that HA was extracted with proteins during the phenol/chloroform additions.

Conclusions

The results demonstrate the potential of surface-enhanced Raman spectroscopy for hyaluronic acid detection in biofluids at clinically relevant concentrations. Removal of most proteins is necessary for successful measurement of HA in artificial models of biofluids. Simple filtration and chemical segregation by drop deposition were insufficient for reducing protein SERS signal. Two chemical extraction techniques were tested. Precipitation of proteins by TCA or extraction of HA by phenol/chloroform successfully reduced protein signal in an artificial model of synovial fluid. Incorporation of an enzymatic digestion step prior to HA extraction was necessary in human synovial fluid specimens because HA is the foci for proteoglycan aggregation and can also bind to many synovial fluid proteins.[34]

One limitation of the drop deposition protocol used in these experiments is that it leaves HA deposited in a ring that is difficult to interrogate efficiently with a line-shaped laser or point source. Optical and optomechanical systems for illuminating the entire drop simultaneously, or deposition onto chemically modified surfaces to manipulate the dried deposit shape, are potential solutions to this problem.

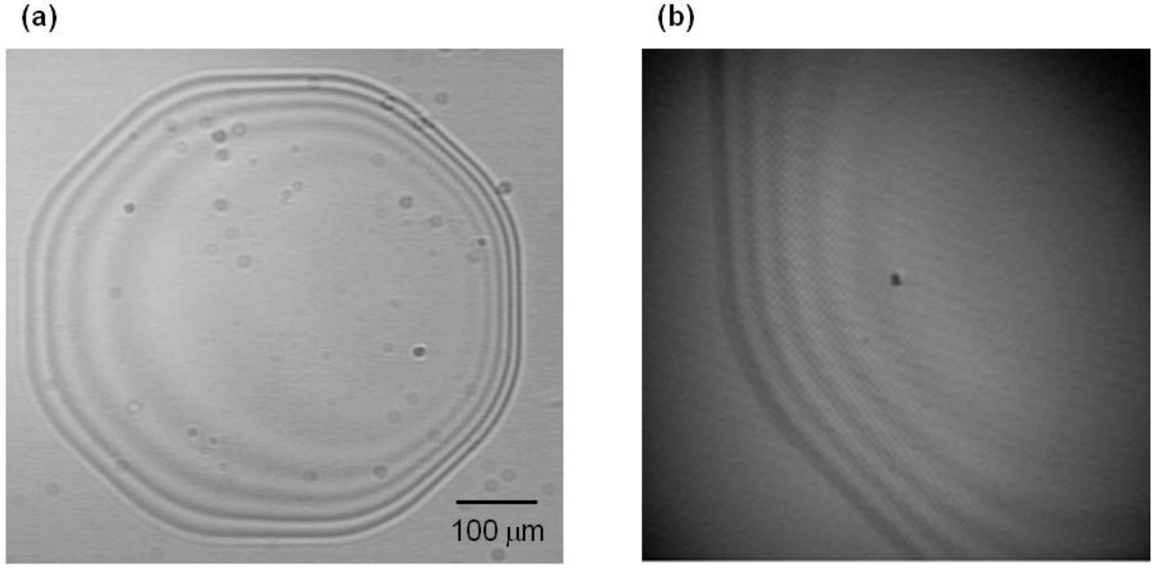

Figure 8.1: Microscope image of a droplet of 4 mg/ml aqueous solution of HA deposited onto a SERS substrate using an (a) 5X/0.25 NA and (b) 10X/0.50 NA objective.

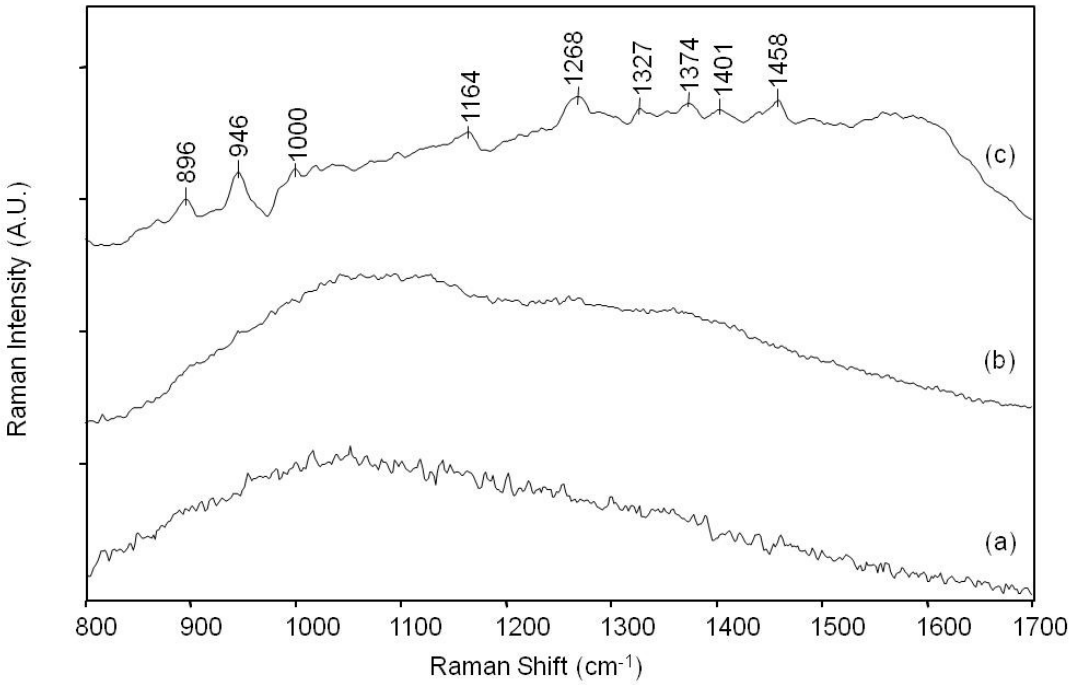

Figure 8.2: Identification of 0.5 mg/ml aqueous HA solution deposited onto (a) fused silica slide, (b) bare gold and (c) a gold-coated SERS substrate.

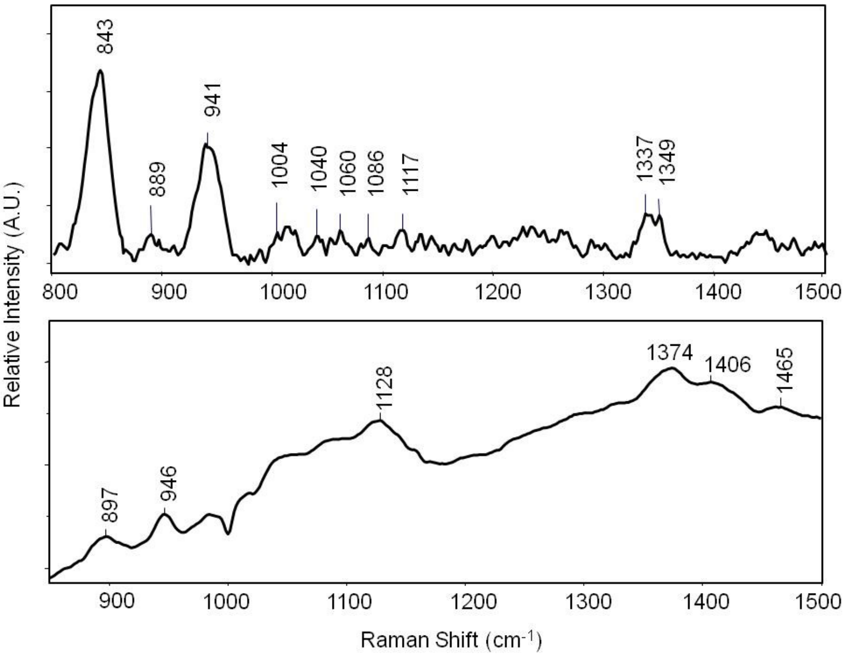

Figure 8.3: SERS spectra of artificial synovial fluid containing 0.5 mg/mL HA after treatment with 10 % TCA solution (a) and after phenol/chloroform treatment (b).

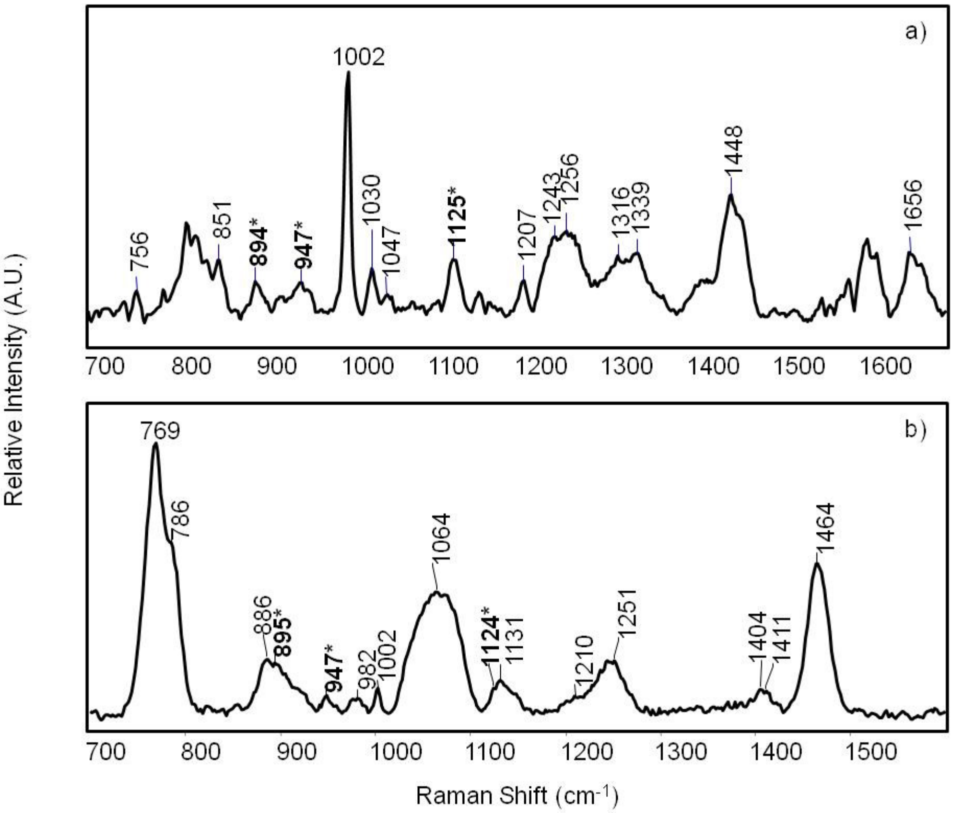

Figure 8.4: SERS spectra of human synovial fluid after the a) enzymatic digestion/filtration step and the b) subsequent phenol/chloroform extraction step of the Kvam method for extracting HA from synovial fluid. Bands attributed to HA at 894, 947 and 1125 cm^{-1} (bolded) were observed in synovial fluid after the enzymatic digestion/filtration step indicating partial reduction in non-specific HA-protein binding. However, the enzymatic digestion appeared to be incomplete because we did not observe HA bands in the supernatant after phenol/chloroform addition.

References

1. Leslie M: **Knee Osteoarthritis Management Therapies**. *Pain Management in Nursing* 2000, **1**(2):51-57.
2. DeGroot J, Bank RA, Tchetverikov I, Verzijl N, TeKoppele JM: **Molecular markers for osteoarthritis: the road ahead**. *Current Opinion in Rheumatology* 2002, **14**:585-589.
3. Fuller CJ, Barr AR, Sharif M, Dieppe PA: **Cross-sectional comparison of synovial fluid biochemical markers in equine osteoarthritis and the correlation of these markers with articular cartilage damage**. *Osteoarthritis and Cartilage* 2001, **9**(49-55).
4. Ghosh P, Guidolin D: **Potential mechanism of action in intra-articular hyaluronan therapy in osteoarthritis: are the effect molecular weight dependent?** . *Seminars in Arthritis and Rheumatism* 2002, **32**(1):10-37.
5. Ishimaru JI, Ogi N, Mizuno S, Goss AN: **Quantitation of chondroitin-sulfates, disaccharides and hyaluronan in normal, early and advanced osteoarthritic sheep temporomandibular joints**. *Osteoarthritis and Cartilage* 2001, **9**(4):365-370.
6. Praest BM, Greiling H, Kock R: **Assay of synovial fluid parameters: hyaluronan concentration as a potential marker for joint diseases**. *Clinica Chimica Acta* 2003, **266**:117-128.
7. Fujimura K, Segami N, Yoshitake Y, Tsuruoka N, Kaneyama K, Sato J, Kobayashi S: **Electrophoretic separation of the synovial fluid proteins in patients with temporomandibular joint disorders**. *Oral Surgery, Oral Medicine, Oral Pathology, Oral Radiology, and Endodontology* 2006, **101**(4):463-468.
8. Poortmans JR, S'Jongers J-J, Bidon G: **Distribution of Plasma Proteins and Hyaluronic Acid in Synovial Fluid and Serum of Human Subjects in Hydarthrosis**. *Clinica Chimica Acta* 1974, **55**:205-209.
9. Carden A, Morris MD: **Application of vibrational spectroscopy to the study of mineralized tissues (review)**. *Journal of Biomedical Optics* 2000, **5**(3):259-268.
10. Naumann D: **FT-Infrared and FT-Raman Spectroscopy in Biomedical Research**. *Applied Spectroscopy Reviews* 2001, **36**(2):239 - 298.
11. Mahadevan-Jansen A: **Raman Spectroscopy: From Benchtop to Bedside**. In: *Biomedical Photonics Handbook.* Edited by Vo-Dinh T. Boca Raton: CRC Press; 2003.
12. Jackson M, Mantsch HH: **Pathology by Infrared and Raman Spectroscopy**. New York: John Wiley and Sons LTD; 2002.
13. Zeiri L, Bronk BV, Shabtai Y, Eichler J, Efrima S: **Surface-Enhanced Raman Spectroscopy as a Tool for Probing Specific Biochemical Components in Bacteria**. *Appl Spectrosc* 2004, **58**(1):33-40.
14. Zeiri L: **SERS of plant material**. *Journal Of Raman Spectroscopy* 2007, **38**(7):950-955.
15. Kaminska A, Inya-Agha O, Forster RJ, Keyes TE: **Chemically bound gold nanoparticle arrays on silicon: assembly, properties and SERS study of**

protein interactions. *Physical Chemistry Chemical Physics* 2008, **10**(28):4172-4180.

16. Zeiri L, Bronk BV, Shabtai Y, Czégé J, Efrima S: **Silver metal induced surface enhanced Raman of bacteria**. *Colloids and Surfaces A: Physicochemical and Engineering Aspects* 2002, **208**(1-3):357-362.
17. Qian X, Peng X-H, Ansari DO, Yin-Goen Q, Chen GZ, Shin DM, Yang L, Young AN, Wang MD, Nie S: **In vivo tumor targeting and spectroscopic detection with surface-enhanced Raman nanoparticle tags**. *Nature Biotechnology* 2008, **26**(1):83(88).
18. Haynes CL, McFarland AD, Van Duyne RP: **Surface-enhanced Raman Spectroscopy**. *Anal Chem* 2005, **77**:338A-346A.
19. Sackmann M, Materny A: **Surface enhanced Raman scattering (SERS) - a quantitative analytical tool?** *Journal of Raman Spectroscopy* 2006, **37**(1-3):305-310.
20. Netti C, Lincoln JR: **Probing molecules with photonic crystal surface-enhanced Raman spectroscopy**. *Microscopy and Analysis* 2005, **19**(6):9-11.
21. Perney NMB, Baumberg JJ, Zoorob ME, Charlton MDB, Mahnkopf S, Netti CM: **Tuning localized plasmons in nanostructured substrates for surface-enhanced Raman scattering** *Optics Express* 2006, **14**(2):847-857.
22. Deegan RD: **Pattern formation in drying drops**. *Physical Review E* 2000, **61**(1):475-485.
23. Deegan RD, Bakajin O, Dupont TF, Huber G, Nagel SR, Witten TA: **Capillary flow as the cause of ring stains from dried liquid drops**. *Nature* 1997, **389**(6653):827-829.
24. Sommer AP, Rozlosnik N: **Formation of Crystalline Ring Patterns on Extremely Hydrophobic Supersmooth Substrates: Extension of Ring Formation Paradigms**. *Crystal Growth & Design* 2005, **5**(2):551-557.
25. Zhang D, Mrozek MF, Xie Y, Ben-Amotz D: **Chemical Segregation and Reduction of Raman Background Interference Using Drop Coating Deposition**. *Applied Spectroscopy* 2004, **58**(8):929-933.
26. Timlin JA, Carden A, Morris MD, Rajachar RM, Kohn D: **Raman spectroscopic imaging markers for fatigue-related microdamage in bovine bone**. *Anal Chem* 2000, **72**:2229-2236.
27. Kvam C, Granese D, Flaibani A, Zanetti F, Paoletti S: **Purification and Characterization of Hyaluronan from Synovial Fluid**. *Analytical Biochemistry* 1993, **211**:44-49.
28. Bansil R, Yannas IV, Stanley HE: **Raman Spectroscopy: A Structural Review of Glycosaminoglycans**. *Biochimica et Biophysica Acta* 1978, **541**:535-542.
29. Barrett TW, Peticolas WL: **Laser Raman Inelastic Light Scattering Investigations of Hyaluronic Acid Primary and Secondary Structure**. *Journal Of Raman Spectroscopy* 1979, **8**(1):35-38.
30. Jiang L, He L, Fountoulakis M: **Comparison of protein precipitation methods for sample preparation prior to proteomic analysis**. *Journal of Chromatography A* 2004, **1023**:317-320.

31. Polson C, Sarkar P, Incledon B, Raguvaran V, Grant R: **Optimization of protein precipitation based upon effectiveness of protein removal and ionization effect in liquid chromatography-tandem mass spectrometry**. *Journal of Chromatography B* 2003, **785**:263-275.
32. Pavelka K, Forejtova S, Olejarova M, Gatterova J, Senolt L, Spacek P, Braun M, Hulejova M, Stovickova J, Pavelkova A: **Hyaluronic acid levels may have predictive value for the progression of knee osteoarthritis**. *Osteoarthritis and Cartilage* 2004, **12**(4):277-283.
33. Grymonpre KR, Staggemeier BA, Dubin PL, Mattison KW: **Identification by Integrated Computer Modeling and Light Scattering Studies of an Electrostatic Serum Albumin-Hyaluronic Acid Binding Site**. *Biomacromolecules* 2001, **2**(2):422-429.
34. Kogan G, Šoltés L, Stern R, Gemeiner P: **Hyaluronic acid: a natural biopolymer with a broad range of biomedical and industrial applications**. *Biotechnology Letters* 2007, **V29**(1):17-25.

Chapter 9

Effect of Conformation and Drop Properties on Surface-Enhanced Raman Spectroscopy of Dried Biopolymer Drops

Introduction

Drop deposition of biofluids is an analytical method that is garnering attention in biomedicine because it is a rapid, specific and simple method to obtain physical chemical information that may have diagnostic value. Drop deposition, also known as the "coffee ring" phenomenon, is based on the observation that a drop of solution will form a ring-like shape as the water evaporates.[1-3] The evaporation process is influenced by drop composition and viscosity, evaporation conditions, and the surface chemistry of the substrate.[4-6] The resulting drop is rich in information; the shape of the resulting droplet and distribution of chemical components may be used to identify impurities, quantify biomarkers, direct crystallization of small molecules, or gauge chemical affinity to an enzyme. Drop deposition is performed on a flat solid surface, such as mica, fused silica or coated stainless steel. This format is compatible with analyses using a variety of optical microscopy or spectroscopic methods.[7-9] Surface-enhanced Raman spectroscopy (SERS) is an attractive analytical method to couple with drop deposition because Raman signal is enhanced 10^2-10^6 fold and detailed chemical information is obtained from SERS spectra.[10-12].

Thickness of polymer films and polymer conformations play important roles in SERS band intensities.[13-16] We hypothesized that drop thickness and polymer conformation would affect SERS band intensities of biopolymer drops similar to the effects observed in thin films. Microscope images of dried drops were used to estimate relative drop thickness. Dark areas in microscope images were areas where light was destructively interfered by a polymer drop. Relative drop thickness was estimated using the following relationship:

$$\Delta t = \frac{1}{2}\lambda(\frac{n_1}{n_2}) * \frac{1}{2}k \qquad \text{for k=1,3,5 etc} \qquad \text{(Equation 1)}$$

where t is the change in drop thickness, λ is the wavelength, n_1 is the index of refraction for air (n_1=1) and n_2 is the index of refraction of the drop (n_2~1.4).[15]

Most biofluids contain biopolymers, such as high molecular weight proteins (nucleoproteins, glycoproteins) or glycosaminoglycans. Hyaluronic acid (HA) is an unsulfated glycosaminoglycan. Although HA can be found throughout the body, it is most concentrated in vitreous humor and synovial fluid.[17] HA is biologically active in wound healing, treating inflammatory joint diseases, and may act as a signaling molecule.[18-21] Hyaluronic acid is also used in the preparation of injectable gels for use as a tissue engineering scaffold or a drug delivery system.[22, 23] The chemical structure of HA, shown in Figure 9.1, is comprised of repeating D-glucuronic acid and N-acetyl-D-glucosamine units. Because the carboxyl groups on D-glucuronic acid are ionized at physiological pH, HA is considered to be a polyelectrolyte polymer and its solution properties can be described using scaling theory.

Intermolecular interactions between HA chains and electrostatic interactions with solvent are extensive and are dominated by carboxyl functional groups on D-glucuronic acid monomers. These interactions are reflected in the sensitivity of HA viscosity to pH, salt, molecules such as sucrose or proteins, and solution temperature.[24-27] For accurate entanglement measurements, viscosity measurements of polyelectrolytes, such as HA, are measured in salt solutions to shield electrostatic repulsion of ionized carboxyl groups. Equations 2-4 were used to calculate the relative, specific, and reduced viscosity of HA:

$$\eta_{rel} = \frac{\eta}{\eta_0} \qquad \text{(Equation 2)}$$

$$\eta_{sp} = \eta_{rel} - 1 \qquad \text{(Equation 3)}$$

$$\eta_{red} = \frac{\eta_{sp}}{c} \qquad \text{(Equation 4)}$$

Where η_0 is the solvent viscosity, η denotes viscosity (η_{red} units of ml/mg, η_{rel} and η_{sp} are dimensionless). Intrinsic viscosity, $[\eta]$ units of ml/mg, is extrapolated from a plot of η_{red} vs. HA concentration using the 2-term Huggins equation[28]:

$$\eta_{red} = [\eta] + k[\eta]^2 c \qquad \text{(Equation 5)}$$

In a solution with added counterion, the rheology of a polyelectrolyte is similar to that of a neutral polymer in good solvent.[29] Scaling theory of polyelectrolyte solutions describes the behavior of polyelectrolytes in a no-salt solution and in a salt solution where electrostatic repulsion is shielded by counterions. Scaling theory describes three concentration domains of polyelectrolyte chains: dilute, semidilute and concentrated. Changes in intermolecular attraction of the polymer with relation to other coils and the solvent characterize each concentration domain. For dilute HA solutions, specific viscosity scales approximately linearly with concentration, reflecting little inter-chain attraction. The scaling theory is especially useful in the semidilute region, where there are large changes associated with concentration.[30] In the semidilute regime there are two intervals, semidilute unentangled and semidilute entangled. In salt solutions, scaling theory predicts that the specific viscosity of polyelectrolytes is dependent on concentration in the following proportions:

$$\eta_{sp} \approx c^{5/4} \text{ (semidilute unentangled)} \qquad \text{(Equation 6)}$$

$$\eta_{sp} \approx c^{15/4} \text{ (semidilute entangled)} \qquad \text{(Equation 7)}$$

Previous examinations of hyaluronic acid solution properties in 0.1 M NaCl and phosphate buffered saline showed a concentration dependence of specific viscosity within predictions of scaling theory.[27] In this study we used viscometry measurements to verify inter-chain attraction between HA molecules, and incorporated the viscosity data into our model of drop formation.

Raman spectroscopy has been used to examine the structure and conformation of hyaluronic acid and other glycosaminoglycans (GAG's) in solution. HA bands at 899 cm^{-1}, 949 cm^{-1} and 1130 cm^{-1} are established markers of HA conformation.[31] Raman spectra of a 4% HA solution (~40 mg/ml) did not change in the pH range of 6-8, where significant changes in HA viscosity and birefringence were observed, indicating the presence of inter-chain long-range interactions.[32, 33] We demonstrated that SERS could detect HA drops at clinically relevant concentrations (0.125-3 mg/ml) that were undetected when spotted onto fused silica or non-enhancing gold surfaces. [34, 35] Early experiments indicated that both drop shape and SERS spectra taken of the droplet were dependent upon HA concentration. [34]

Biopolymers affect bulk biofluid properties, such as viscosity, which are known to influence drop deposition. We incorporated scaling theory principles of polyelectrolyte solution behavior into a drop deposition model developed to describe ring formation of suspended particles.[5] As seen in Figure 9.2, there are four primary flows or interactions that are responsible for the fluid dynamics of drop deposition: capillary flow (F_C), Marangoni flow (F_M), intermolecular interactions (I_{IM}) and substrate-drop interaction (I_S). For suspended particles, I_{IM} is minimal and a simple prediction of ring formation can be made: when $I_S > F_C$ then there is a uniform deposition and when $I_S < F_C$ then there is ring formation. Biopolymers strongly interact with other polymer molecules, ions and water in solution. Thus the effects of intermolecular interaction on drop formation were considered in the model of polymer drop formation.

Our previous studies, described in Chapter 8, showed preliminary evidence on the effect of HA concentration on drop formation. The presence of concentric rings and a non-linear SERS response with HA concentration was initially attributed to the entanglement properties of HA. In that study, we examined HA from rooster comb with an average molecular weight of ~$2x10^6$ Da with unknown polydispersity and potential chain aggregation from minor protein contaminants.[24]

In this study, we measured the entanglement of well-characterized HA. Because the solution properties of HA is highly dependent on its molecular weight, we examined HA from bacterial sources with low polydispersity. [24, 25, 28] Salt solutions of high molecular weight HA (MW>$1x10^6$ Da) was expected to exhibit entanglement behavior at

~ 1 mg/ml, while solutions of low molecular weight HA (MW<$5x10^5$ Da) was not expected to exhibit entanglement at any concentration.

Viscosity measurements were used to incorporate the effect of intermolecular interactions on drop formation. HA entanglement behavior was modeled using scaling theory principles. We found combined effects of drop thickness and shape, and polymer conformation on SERS spectra of high molecular weight hyaluronic acid drops dried onto a SERS-active surface. Protein impurities that are known to induce aggregation of HA chains can be easily detected by SERS in binary protein-HA solutions. The ring breathing band at ~1001 cm^{-1} was used as a marker for synovial fluid protein content because there are no HA bands at that Raman shift. We found SERS band intensities of hyaluronic acid dried drops were affected by drop properties and HA conformation.

Materials and Methods

Raman spectroscopy

A Nikon E600 epi-illumination microscope was modified for Raman spectroscopy (Nikon, Melville, NY, USA). A Kaiser Invictus line-focused laser operating at 785 nm was used as an excitation source (Kaiser Optical Systems, Ann Arbor, MI, USA). The laser line was focused onto the sample using a 20X/0.75 Nikon S Fluar objective. A 0.3 neutral density filter was used to attenuate the laser intensity to 8-11 mW. Raman signal was collected for 3-5 minutes. Raman scattered light was collected by the 20X/0.75 S Fluor microscope objective, directed to a spectrograph (Kaiser HoloSpec *f*/1.8), and focused onto a 1024x128 near-infrared optimized CCD camera (Andor Technologies, Belfast, Ireland). Because of noise in the system and the spectral resolution of 4 cm^{-1}, band positions were reproducible to ± 1-2 cm^{-1}. The holographic grating used in the spectrometer provided a spectral window of 400-1800 cm^{-1}. A non-confocal geometry was used to maximize collection efficiency. White-light microscope images were collected using 2X/0.06NA Plan UW, 4X/0.02NA Plan Apo and 10X/0.45NA S Fluor microscope objectives (Nikon, Melville, NY, USA). Gold coated Klarite SERS substrates (D3 Technologies Ltd, Southamptom, UK) were used as received. No laser-induced damage was observed on the substrates or the dried droplets.

HA solution preparation and drop deposition

Sodium hyaluronate manufactured from bacterial fermentation using Strep. A. bacteria were used without further purification ($1.4x10^6$ Da for high MW, and $2.3x10^5$ Da for low MW) (Lifecore Inc., Chaska, MN, USA). Solvents and reagents were analytical grade. The molecular weight of the $1.4x10^6$ Da hyaluronic acid was verified as 1.5×10^6 in 0.1 M NaCl using the Mark-Houwink relationship $[\eta]=KM^a$, where $[\eta]=2.52$ ml/mg a=0.79 and K=0.0336 ml/g at 25° in 0.1 M NaCl.[27] Stock solutions of 6 mg/ml or 10 mg/ml were prepared by dissolving sodium hyaluronate in purified water. Stock solutions were stirred overnight in ambient laboratory conditions to ensure complete solubilization. Serial dilutions were prepared volumetrically from the stock solutions. Dilutions were prepared at concentrations of 0.125, 0.25, 0.5, 1, 1.5, 2, 3, 4, and 5 mg/ml and stored at 0°C until examination. Additional HA solutions were prepared in 0.1 M or 0.2 M NaCl using the protocol described above to examine HA entanglement behavior in a salt solution. HA solutions were evaluated using a capillary viscometer and the drop deposition/SERS protocol. For the drop deposition procedure, a 0.2-2 µl Eagle pipette (World Precision Instruments, Sarasota, FL, USA) was used to deposit 0.2 µl of HA solutions onto the substrate. Drops were dried in ambient laboratory conditions overnight prior to collecting spectra. Approximately 8 drops were deposited onto a SERS substrate in random order to reduce any effects of inter-chip variability. For ring-shaped drops, transects were collected within the ring. For uniform depositions, transects were collected at various locations in the drop.

Capillary viscometry

Cannon-Ubbeholde semi-micro ultra-low charge capillary viscometers were used to measure viscosity of HA solutions in concentrations ranging from 0.125-4 mg/ml. Three capillary viscometers were used: 1) size 50, approximate viscometric constant: 0.004 centiStokes/sec (cSt/s); 2) size 75, approximate viscometric constant: 0.008 (cSt/s); and 3) size 200, approximate viscometric constant: 0.1 cSt/s). The efflux time for deionized water, 0.1M NaCl, and 0.2 M NaCl in the size 75 viscometer was 151s, 153s, and 161s respectively. The overlap concentration (c*, in mg/ml) and entanglement concentration

(c_e, in mg/ml) was calculated from a log-log plot of specific viscosity versus HA concentration, shown in Figures 9.3 and 9.4.

SERS data analysis

Raman transects were imported to Matlab (v 6.1, The Math Works, Natick, MA). Spectra were corrected for curvature, dark current and variations in the CCD quantum efficiency. Corrected spectra were imported to GRAMS/AI© (ThermoGalactic). In GRAMS/AI©, background signal from the SERS substrate (if applicable) was subtracted and a baseline correction was performed using a user-defined, multi-point polynomial. Baseline corrected spectra were intensity normalized to the 1130 cm^{-1} band. HA peaks were fit to mixed Lorentzian/Gaussian bands using the GRAMS/AI© curvefit routine. The resulting curve-fit was accepted if the R^2 was > 0.999 and the calculation did not produce any negative subtraction artifacts.

Estimation of drop profile

White-light microscope images were collected on the Raman microscope using 2X/0.06NA Plan UW, 4X/0.02NA Plan Apo and 10X/0.45NA S Fluor microscope objectives (Nikon, Melville, NY, USA). Images were imported into Matlab where the position of the drop edge, drop center, and the middle of each interference band was estimated. The pixel positions were plotted in Excel and converted to microns using a 25 μm bar target standard. Thickness was estimated using Equation 1, and plotted against position.

Results

Viscosity measurements

A summary of viscosity measurements is presented in Table 9.1. Values for intrinsic viscosity [η], and the Huggins' constant 'k', for low and high MW HA in 0.1 M NaCl and 0.2 M NaCl solutions are included. For high and low MW HA, intrinsic viscosity was within reported ranges, and decreased with increasing salt concentration.[26] Figure 9.3 shows specific viscosity measurements of low molecular weight HA in water (Figure 9.3.a) and 0.1 M NaCl (Figure 9.3.b). Figure 9.4 shows the dependence of specific viscosity on high molecular weight HA concentration in water (Figure 9.4.a) or in salt solution (Figure 9.4.b).

Microscope images of dried droplets

Figure 9.5 shows white-light images of 5 mg/ml (Figure 9.5.a) and 0.25 mg/ml (Figure 9.5.b) HA in H_2O drop dried on the SERS substrate. Ring deposition versus uniform deposition was dependent on HA concentration. Figure 9.5.a shows a uniform deposition with concentric rings around the droplet edge, Figure 9.5.b shows a ring deposition and no concentric rings. Concentric rings around the droplet edge are evident in microscope images of concentrated (>1 mg/ml) HA solutions are dried on the SERS substrate. The position and number of concentric rings relative to the drop edge provides an indication of thickness. More concentric rings indicate a thicker HA deposition. Figure 9.6 shows the estimated drop thickness when dark rings are modeled as thin film interference patterns. At low HA concentrations (0.125-1 mg/ml), concentric rings were not observed and the shape of the drop changed from a ring (Figure 9.6.a) to a uniform deposition (Figure 9.6.b). The uniform deposition shape is maintained but the thickness of the deposition increases when more concentrated (>1 mg/ml) HA solutions are deposited onto the SERS surface (Figure 9.6.c).

SERS of HA dried droplets

Assignment of the major bands of HA were based on previous Raman reports of HA and are listed in Table 9.2.[31, 33] The bands at 899 cm^{-1}, 945 cm^{-1}, 1130 cm^{-1} and 1410 cm^{-1} were used to examine HA conformation in previous vibrational spectroscopic studies of glycosaminoglycans.[31, 33, 36, 37] Figure 9.7 shows a representative spectrum of high molecular weight HA at 1.5 mg/ml in water and 1.5 mg/ml in 0.2 M NaCl, after deposition onto the SERS substrate. HA does have a band in the amide I region (1590-1700 cm^{-1}), but it is weak and broad in Raman spectra. Thus, we focused our analysis on the 800-1500 cm^{-1} region. HA Raman spectra in water and salt solution are similar to a spectrum of solid state HA. These observations are consistent with Raman spectra of other glycosaminoglycans.[31, 33]

Figure 9.8 shows the effect of HA conformation, drop type, and drop thickness on SERS band intensities at 899 cm^{-1} and 945 cm^{-1}. Figure 9.8.a shows the effect of outward convective flow and substrate-HA attraction on SERS band intensities of HA in H_2O. Viscosity measurements indicate that a constant inter-chain interaction of HA in H_2O in the concentration range 0.125-2 mg/ml. Figure 9.8.b shows band intensities for HA in salt solution, and variable inter-chain interaction was considered in addition to outward convective flow and substrate-HA attraction.

Discussion

Viscosity measurements

Viscosity of high MW and low MW HA was measured using capillary viscometry. Specific viscosity of low MW scaled linearly with HA concentration from 0.125-4 mg/ml, as shown in Figure 9.3. Low MW HA was not examined using the drop deposition/SERS method because viscometry measurements indicated no significant inter-chain attraction (η_{sp}~$c^{0.98}$). Thus, we focused on high MW HA. High MW HA was examined using the drop deposition/SERS method because viscosity measurements indicated significant inter-chain attraction in water and a variable attraction in salt. Specific viscosity of HA in H_2O scaled with concentration to a power of 1.6 ($\eta_{sp}=50.5c^{1.6}$) as seen in Figure 9.4. This power relationship was constant from 0.125-1.5 mg/ml and indicated that HA chains strongly interact in water, even at low concentrations. We observed a large increase in specific viscosity with concentration of HA in H_2O, which is reflected in a large value of the slope (50.5).

As shown in Figure 9.4, there are three distinct specific viscosity regions for the high MW HA salt solutions. These regions have a different scaling of specific viscosity with concentration, and correspond to dilute, semidilute unentangled and semidilute entangled regimes. At low HA concentrations specific viscosity scaled approximately linearly (η_{sp}~$c^{1.1}$), indicating the dilute regime where HA chains did not interact and were not overlapped. The overlap concentration (c*) marked the end of the dilute regime and was where HA chains began to interact. As shown in Table 9.1, the overlap concentration was 0.74-0.76 mg/ml for high MW HA in 0.2 M and 0.1 M NaCl. At higher HA concentrations specific viscosity scaled to a higher power (η_{sp}~$c^{2.2}$), indicating overlapping HA chains. The entanglement concentration (c_e) marked the onset of the semidilute entangled regime and was found to be 1.9-2.8 mg/ml in 0.1 M and 0.2 M NaCl. Specific viscosity scaled with concentration to a higher extent (η_{sp}~$c^{3.6}$) above chain entanglement, indicating significant inter-chain HA attraction.

Modeling HA drop formation

Previous models of drop formation of suspended particles on a solid flat surface assume four main forces on a particle during solvent evaporation.[5] Briefly, a uniform deposition is expected when the substrate-HA attraction (I_S in Figure 9.2) is greater than the outward capillary flow (F_C in Figure 9.2) toward the contact point of the droplet and a ring-shaped deposition is expected when the F_C>I_S. However, this model assumed negligible intermolecular attraction (I_{IM} in Figure 9.2). Our model of drop formation included the effect of intermolecular attraction because viscosity measurements indicated significant intermolecular attraction for high MW HA in H_2O and in salt solution.

We considered only I_S and F_C in the model of HA in H_2O drops. Scaling of specific viscosity of HA in H_2O (η_{sp}~$50.5c^{1.6}$) indicated constant intermolecular interactions, and we assumed a constant I_{IM}. Specific viscosity increased significantly with HA concentration, as indicated by the large constant (η_{sp}~$50.5c^{1.6}$). We also assumed constant I_S. From 0.125-0.5 mg/ml we observed ring deposition, indicating F_C>I_S. At these concentrations HA dried as a ring-shaped deposition, as shown in Figure 9.5.a. At concentrations above 1 mg/ml, specific viscosity increased to the point where outward convective flow became weaker than substrate-HA attraction. At these higher concentrations HA drops dried with uniform deposition, shown in Figure 9.5.b.

Dark lines found in dried drops were examined using principles of destructive interference by thin films. Relative drop thickness and drop profiles were estimated using this technique. Figure 9.6 shows the profiles and relative thickness of HA in water at 0.25 mg/ml, 1 mg/ml and 5 mg/ml. Relative thickness of the drop is ~150 nm at 0.25 and 1 mg/ml, and ~1.4 μm at 5 mg/ml. Estimation of relative drop thickness provided a basis to compare the collection efficiency and efficiency of surface plasmon interaction with HA. SERS spectra of polymer thin films are affected by film thickness and polymer conformation. [13, 14, 16] SERS bands are more intense at thinner films, owing to a greater interaction of surface plasmons with the film. We propose that, in polymer drops, SERS band intensities are also subject to the effects of drop thickness and polymer conformation.

In addition to increased collection efficiency at low HA concentrations (because of a thinner deposition) there was a preconcentration effect with ring deposition versus uniform deposition. There was also a greater apparent concentration in the ring versus a uniform deposition. We used our estimates of ring profiles from interference patterns to calculate a concentration density (mg/ml/μm^2) and identified a 4-fold increase in concentration density in the 0.25 mg/ml ring compared to the 1 mg/ml uniform deposition. There was, as expected, a 5-fold increase in concentration density of the 5 mg/ml uniform deposition compared to the 1 mg/ml uniform deposition. Effects of ring versus uniform deposition and preconcentration were observed in SERS spectra from aqueous HA dried drops, especially in the band intensity at 945 cm^{-1}.

Viscosity measurements of HA in salt solutions indicated variable intermolecular attraction. Intermolecular attraction (F_4), outward convective flow (F_2), and substrate-HA attraction (F_1) were considered in the model of HA in salt drops. Ring formations and concentric ring formations were observed in dried drops of HA in salt solution. However, sodium chloride crystals precipitated throughout the dried drops and prohibited estimation of drop properties using interference patterns. We expect that future studies to verify our method of estimating drop properties using interference patterns, such as the use of atomic force microscopy, will account for the presence of salt crystals and allow drop profiles to be obtained.[38]

SERS of HA dried drops

Since most synovial fluid proteins have at least one phenylalanine ring, the ring breathing mode at ~1001 cm^{-1} was used as a marker for protein content. There was no detectable protein signal, as indicated by no band at ~1001 cm^{-1}. We focused our analyses on the "fingerprint" region (400-1800 cm^{-1}) because it is a more direct measurement of HA conformation. In this spectral range, HA is weakly scattering in solution and previous vibrational spectroscopy studies of HA in thin films or solutions have been limited to high (>10 mg/ml or 1% w/v) HA concentrations.[31, 33, 39-41] SERS spectra of aqueous HA (Figure 9.8.a) and HA in salt solution (Figure 9.8.b) dried onto the SERS surface showed little variation. The C_1-H deformation band occurs at ~ 899 cm^{-1} when the C_1 hydrogen is axial and at ~ 845 cm^{-1} when the C_1 hydrogen is equatorial. Symmetric C-O-C linkage vibration occurs at ~945 cm^{-1} for GAG's with β-type or α-type linkages. The 899 cm^{-1} and 945 cm^{-1} SERS bands were examined because they are the most insightful to HA conformation and were the best resolved bands in SERS spectra of HA. SERS band intensities at 899 cm^{-1} and 945 cm^{-1} were affected by efficiency of the SERS enhancement processes, HA concentration and HA conformation. Drop profiles from microscope images were used to estimate the relative concentration density of HA in a drop or uniform deposition. Viscosity measurements were used to verify HA conformation and model the effect of intermolecular attraction on drop formation. SERS intensities of the 899 cm^{-1} and 945 cm^{-1} bands were examined in the context of drop properties and HA conformation. The 945 cm^{-1} SERS band appeared to be more sensitive to these effects than the 899 cm^{-1} SERS band. As seen in Figure 9.8, there are differences in SERS band intensities when aqueous HA (Figure 9.8.a) or HA in salt solution (Figure 9.8.b) is deposited onto a SERS substrate.

Dried drops of aqueous HA solutions formed a ring at low HA concentrations and a uniform deposition at higher HA concentrations. Localization of HA into a ring had a preconcentration effect, and resulted in more intense SERS bands (Figure 9.8.a). At higher HA concentrations (>0.5 mg/ml, uniform deposition), the 945 cm^{-1} SERS intensity slightly increased, indicating contributions from unenhanced Raman as the relative thickness increases.

SERS band intensities at 899 cm^{-1} and 945 cm^{-1} varied with HA concentration when HA salt solutions were deposited onto the SERS substrate. Changes in the 945 cm^{-1} SERS band intensity, shown in Figure 9.8.b, roughly correlated to transitions from a dilute to semidilute unentangled solution at 0.76 mg/ml and from a semidilute unentangled to a semidilute entangled solution at 1.9-2.8 mg/ml. The SERS 945 cm^{-1} intensity increased with HA concentration in the dilute regime (0.125-0.5 mg/ml). After 0.5 mg/ml, the SERS 945 cm^{-1} intensity decreased until ~ 2 mg/ml. At HA concentrations greater than 2 mg/ml, the SERS 945 cm^{-1} intensity remained relatively constant. SERS data indicate that, in salt solutions, the HA C-O-C backbone is stretched on the SERS surface at dilute concentrations, as reflected by a higher intensity of the SERS 945 cm^{-1} band. We observed a "dilution effect" in the SERS 945 cm^{-1} band intensity, where the band intensity decreased at concentrations above the overlap concentration. [13, 14] The transition observed in the SERS 945 cm^{-1} band intensity correlated to the transition from an elongated chain at dilute concentrations to collapsed chains that are overlapping. A "dilution effect" was not observed for the SERS 899 cm^{-1} band intensity. As seen in Figure 9.8.b, the SERS 899 cm^{-1} intensity decreased from 0.125-1 mg/ml and remained constant thereafter. SERS data indicate that the 899 cm^{-1} band is sensitive to conformation changes when the HA chain is elongated at dilute concentrations while at concentrations higher than the overlap concentration there were no changes observed in the 899 cm^{-1} SERS intensity.

Conclusions

Biopolymers are ubiquitous in biofluids and in order to develop a more accurate model of biofluid drop formation, we needed to understand the effect of biopolymers in the context of drop formation and subsequent collection of SERS spectra from dried drops. We examined the effect of biopolymers on drop formation using hyaluronic acid (HA) as a model biopolymer. Surface-enhanced Raman spectroscopy (SERS) was used to examine chemical structure of HA solutions dried onto a SERS-active substrate as a ring deposition or as a uniform deposition. Viscosity measurements were used in previously established models of drop formation to account for intermolecular interaction of HA chains. Microscope images were used to estimate relative drop thickness and drop profile.

We found that the complex viscoelastic properties of HA affected drop formation and SERS spectra collected from drops. Two models of drop formation were developed for HA. In the first model, where aqueous HA is dried onto the SERS substrate, we found that solution viscosity was the dominant force in the type of deposition which was reflected in the SERS band intensity at 945 cm^{-1}. In the second model, where HA in salt solutions were deposited onto the SERS substrate, we found that the viscoelastic properties of HA was the dominant force in the SERS band intensity at 945 cm^{-1}.

Combined data from viscosity measurements with microscope images provided a more accurate description of HA solution properties during drop formation. Future studies include using SERS combined with drop deposition of biofluids which will incorporate the effects of biopolymer entanglement and substrate-polymer interactions.

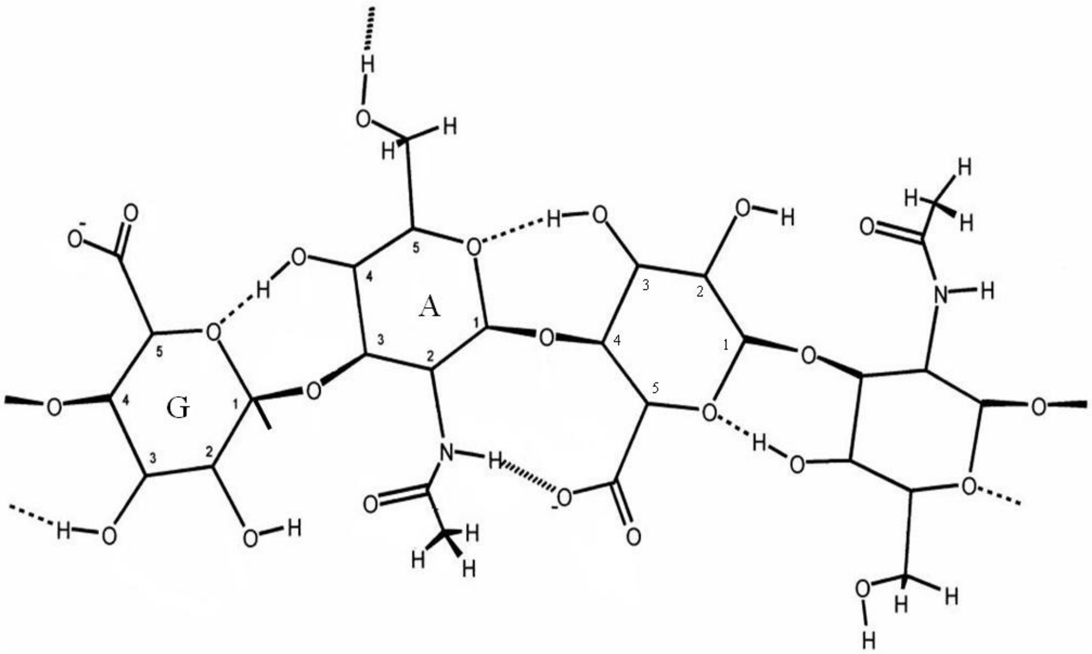

Figure 9.1: The chemical structure of hyaluronic acid. Hyaluronic acid is a polysaccharide composed of two monosaccharides: D-glucuronic acid (Monomer G) and N-acetyl-D-glucosamine (Monomer A).

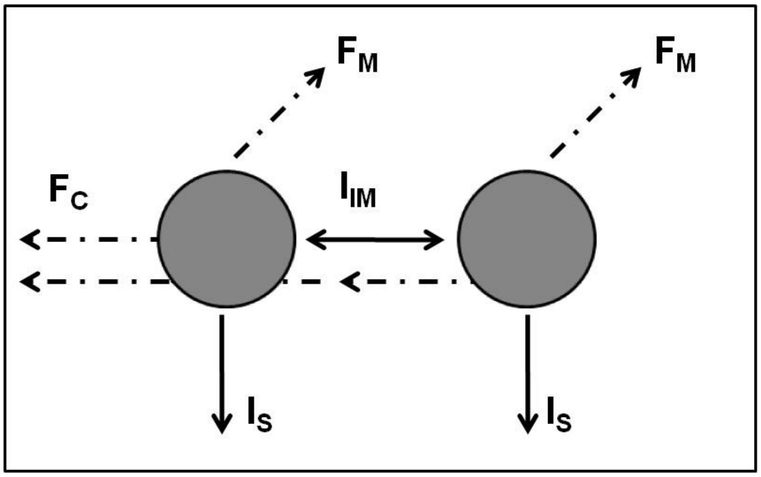

Figure 9.2: There are four primary flows or interactions that influence biofluid drop formation. Capillary flow, F_C, is responsible for fluid motion toward the pinned contact lines at the drop edge, upward Marangoni flow, F_M, arises from a temperature gradient within the drying drop. Substrate and fluid interactions, I_S, and intermolecular interactions, I_{IM}, also influence drop deposition.

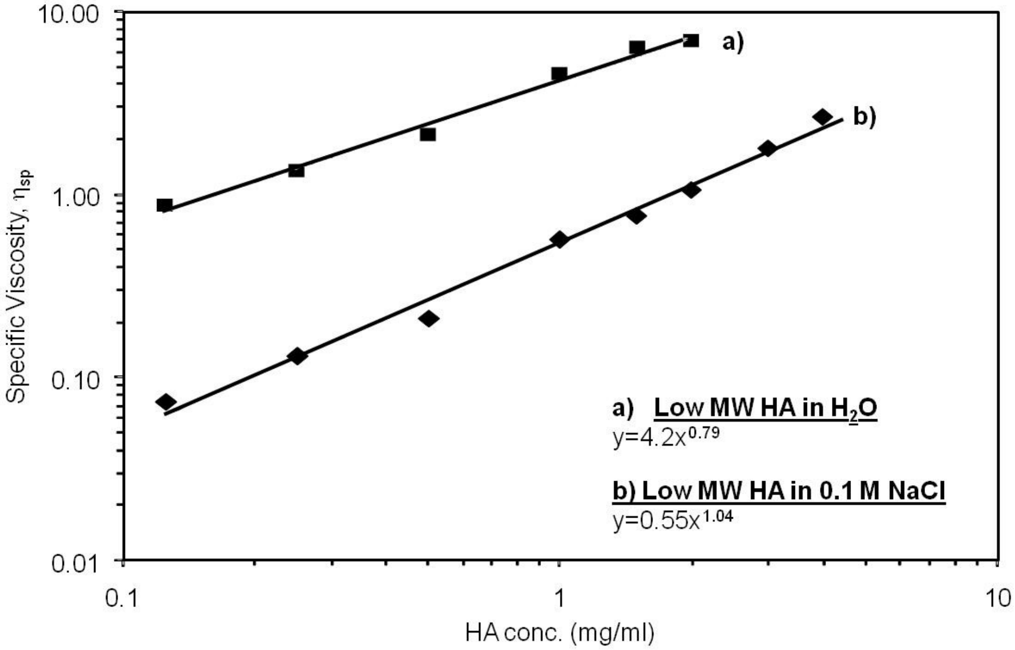

Figure 9.3: Specific viscosity of low molecular weight (MW=2.3x10^5 Da) hyaluronic acid (LMW-HA) in water (Trendline a) and 0.1 M NaCl (Trendline b).

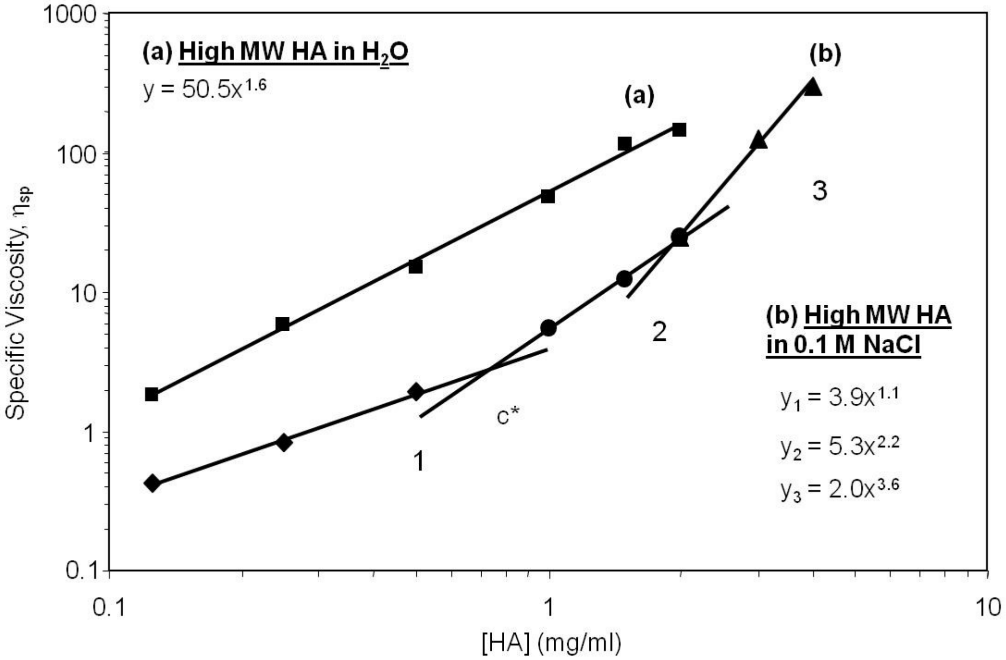

Figure 9.4: Specific viscosity of high molecular weight (MW=1.4x10^6 Da) hyaluronic acid (HMW-HA) in water (Trendline a) and 0.1 M NaCl (Trendline b).

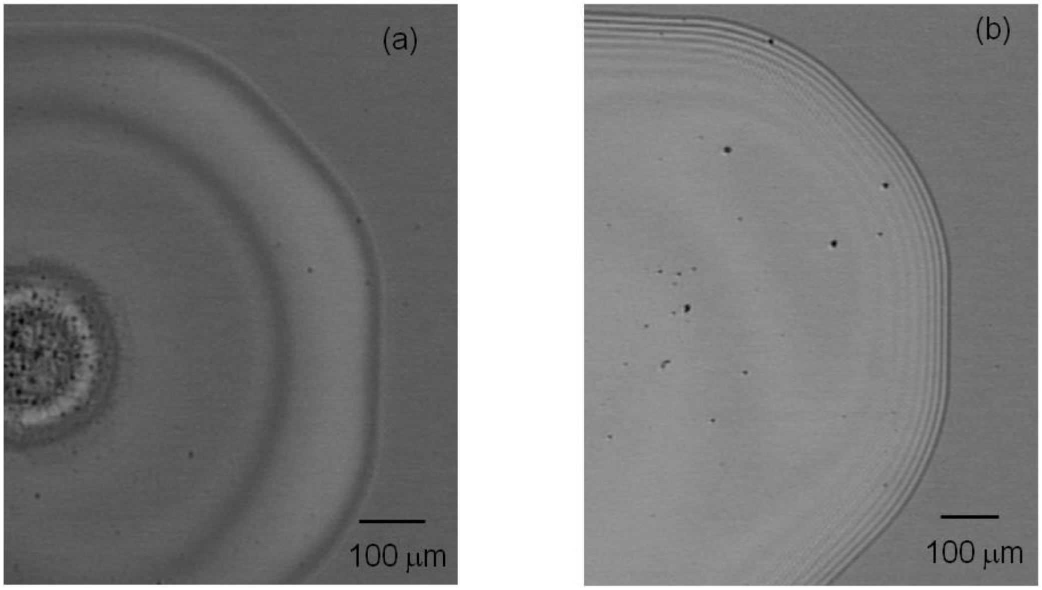

Figure 9.5: Microscope images of aqueous HA dried drops at (a) high and (b) low HA concentrations. At high concentrations, concentric rings formed on the outer edge of the drop and the HA dried as a uniform deposition. At low concentrations, HA dried as a ring deposit and no concentric rings were observed. Destructive interference of light resulted in dark bands in microscope images.

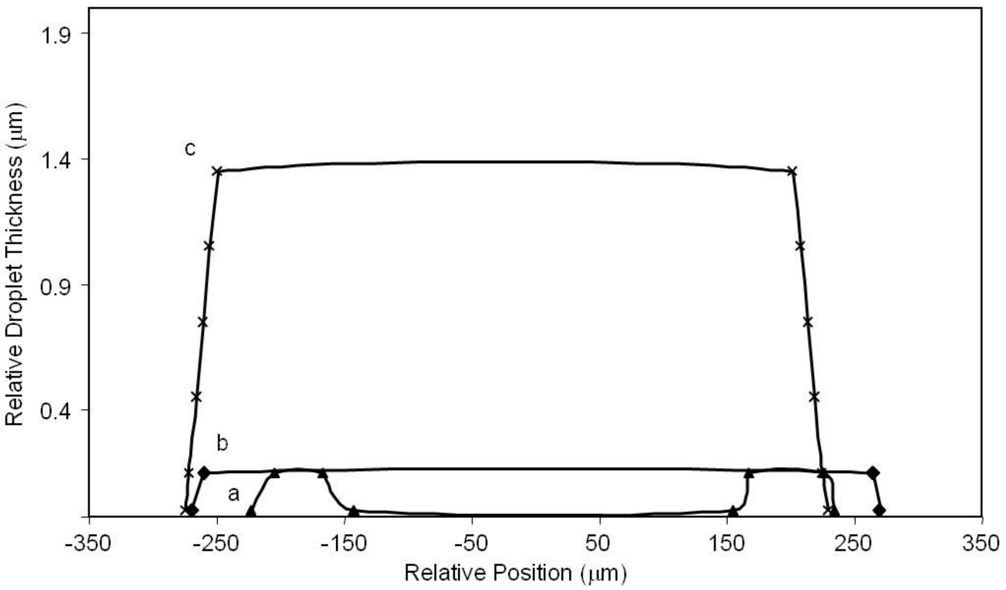

Figure 9.6: Relative drop thickness and drop profiles were calculated from the interference patterns. At low aqueous HA drops, a ring-shaped drop is formed (a). At ~ 1mg/ml, the drop dried as a uniform deposition (b). Highly concentrated HA solutions also dried as a uniform deposition, but the relative drop thickness increased (c).

.

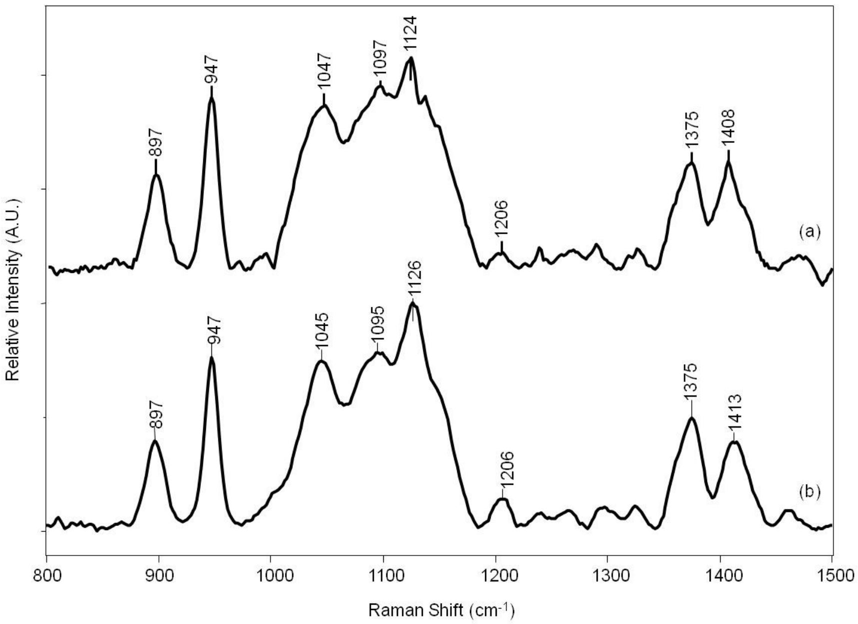

Figure 9.7: SERS spectrum of dried drops of high MW HA in solutions of: a) 5 mg/ml in H_2O and b) 4 mg/ml in 0.1 M NaCl

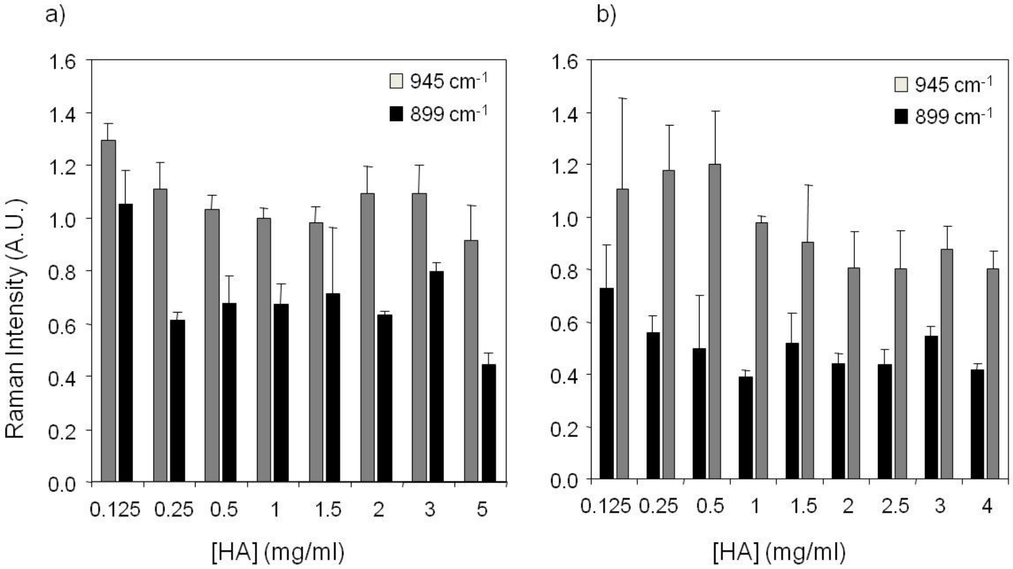

Figure 9.8: SERS band intensities at 899 cm^{-1} and 945 cm^{-1} are dependent on HA concentration, HA conformation and relative drop thickness.

	High MW HA (1.387 x10^6 Da)		Low MW HA (2.344 x10^5 Da)	
Parameter	0.1 M NaCl	0.2 M NaCl	0.1 M NaCl	0.2 M NaCl
[η] (ml/mg)	2.5	2.03	0.39	0.35
c* (mg/ml)	0.76	0.74	N/A	N/A
c*[η]	1.9	1.5	N/A	N/A
k’	0.44	0.59	0.44	0.62
c_e (mg/ml)	1.9	2.8	N/A	N/A

Table 9.1: Intrinsic viscosity [η], overlap concentration (c*), entanglement concentration (c_e), and the Huggins constant (k’) were calculated from viscosity measurements of high and low MW HA in a salt solution.

Raman Shift (cm^{-1})	Band Assignment
899	C_1-H deformation, β-linkage
945	Skeletal C-O-C linkage stretch
~1045	C-O,C-C
~1090	C-OH bend, acetyl group
~1130	C_4-OH bend and C_4-H bend
~1150	C-O, C-C, Oxygen bridge
~1210	CH_2 twist
1330	CH bend, Amide III
1370	COO^- symmetric stretch CH_3 deformation
~1410	COO^- symmetric stretch CH_3 bend
~1460	CH_2 bend

Table 9.2: Raman bands for hyaluronic acid observed for solid HA, assignments are based on previous Raman studies of HA.

References

1. Deegan RD, Bakajin O, Dupont TF, Huber G, Nagel SR, Witten TA: **Capillary flow as the cause of ring stains from dried liquid drops**. *Nature* 1997, **389**(6653):827-829.
2. Deegan RD: **Pattern formation in drying drops**. *Physical Review E* 2000, **61**(1):475-485.
3. Deegan RD, Bakajin O, Dupont TF, Huber G, Nagel SR, Witten TA: **Contact line deposits in an evaporating drop**. *Physical Review E* 2000, **62**(1):756.
4. Sommer AP: **Microtornadoes under a Nanocrystalline Igloo: Results Predicting a Worldwide Intensification of Tornadoes**. *Crystal Growth & Design* 2007, **7**(6):1031-1034.
5. Sommer AP, Rozlosnik N: **Formation of Crystalline Ring Patterns on Extremely Hydrophobic Supersmooth Substrates: Extension of Ring Formation Paradigms**. *Crystal Growth & Design* 2005, **5**(2):551-557.
6. Tadashi K, Eisuke N, Tatsuya Y, Masao D: **Piling-to-buckling transition in the drying process of polymer solution drop on substrate having a large contact angle**. *Physical Review E (Statistical, Nonlinear, and Soft Matter Physics)* 2006, **73**(1):011601.
7. Yakhno TA, Yakhno VG, Sanin AG, Sanina OA, Pelyushenko AS, Egorova NA, Terentiev IG, Smetanina SV, Korochkina OV, Yashukova EV: **The informative-capacity phenomenon of drying drops**. *Engineering in Medicine and Biology Magazine, IEEE* 2005, **24**(2):96-104.
8. Zhang D, Mrozek MF, Xie Y, Ben-Amotz D: **Chemical Segregation and Reduction of Raman Background Interference Using Drop Coating Deposition**. *Applied Spectroscopy* 2004, **58**(8):929-933.
9. Filik J, Stone N: **Drop coating deposition Raman spectroscopy of protein mixtures**. *The Analyst* 2007, **132**:544-550.
10. Andreas O: **The 'chemical' (electronic) contribution to surface-enhanced Raman scattering**. *Journal of Raman Spectroscopy* 2005, **36**(6-7):497-509.
11. Haynes CL, McFarland AD, Van Duyne RP: **Surface-enhanced Raman Spectroscopy**. *Anal Chem* 2005, **77**:338A-346A.
12. Netti C, Lincoln JR: **Probing molecules with photonic crystal surface-enhanced Raman spectroscopy**. *Microscopy and Analysis* 2005, **19**(6):9-11.
13. Xue G: **SERS evidence for existence of a critical concentration for polymer coil shrinking in poly(4-vinyl pyridine) solution**. *Polymer Bulletin* 1994, **33**:229-235.
14. Xue G, Lu Y, Gao J: **Surface enhanced Raman scattering evidence for the existence of a critical concentration for coil shrinkage in polystyrene solutions**. *Polymer* 1994, **35**(14):3127-3130.
15. Tadmor R, Chen N, Israelachvili JN: **Thin film rheology and lubricity of hyaluronic acid solutions at a normal physiological concentration**. *Journal of Biomedical Materials Research* 2002, **61**(4):514-523.
16. Baibarac M, Cochet M, Lapkowski M, Mihut L, Lefrant S, Baltog I: **SERS spectra of polyaniline thin films deposited on rough Ag, Au and Cu. Polymer**

film thickness and roughness parameter dependence of SERS spectra. *Synthetic Metals* 1998, **96**(1):63-70.

17. Kogan G, Šoltés L, Stern R, Gemeiner P: **Hyaluronic acid: a natural biopolymer with a broad range of biomedical and industrial applications**. *Biotechnology Letters* 2007, **V29**(1):17-25.
18. Goldberg VM, Buckwalter JA: **Hyaluronans in the treatment of osteoarthritis of the knee: evidence for disease-modifying activity**. *Osteoarthritis and Cartilage* 2005, **13**(3):216-224.
19. Pavelka K, Forejtova S, Olejarova M, Gatterova J, Senolt L, Spacek P, Braun M, Hulejova M, Stovickova J, Pavelkova A: **Hyaluronic acid levels may have predictive value for the progression of knee osteoarthritis**. *Osteoarthritis and Cartilage* 2004, **12**(4):277-283.
20. Praest BM, Greiling H, Kock R: **Assay of synovial fluid parameters: hyaluronan concentration as a potential marker for joint diseases**. *Clinica Chimica Acta* 2003, **266**:117-128.
21. Weindl G, Schaller M, Schafer-Korting M, Korting HC: **Hyaluronic Acid in the Treatment and Prevention of Skin Diseases: Molecular, Biological, Pharmaceutical and Clinical Aspects**. *Skin Pharmacology and Physiology* 2004, **17**:207-213.
22. Gutowska A, Jeong B, Jasionowski M: **Injectable gels for tissue engineering**. *The Anatomical Record* 2001, **263**(4):342-349.
23. Mori M, Yamaguchi M, Sumitomo S, Takai Y: **Hyaluronan-based Biomaterials in Tissue Engineering**. *Acta Histochemica et Cytochemica* 2004, **37**(1):1-5.
24. Fouissac E, Milas M, Rinaudo M: **Shear-Rate, Concentration, Molecular Weight, and Temperature Viscosity Dependences of Hyaluronate, a Wormlike Polyelectrolyte**. *Macromolecules* 1993, **26**:6945-6951.
25. Kobayashi Y, Okamoto A, Nishinari K: **Viscoelasticity of Hyaluronic Acid with Different Molecular Weights**. *Biorheology* 1994, **31**(3):235-244.
26. Mo Y, Takaya T, Nishinari K, Kubota K, Okamoto A: **Effects of sodium chloride, guanidine hydrochloride, and sucrose on the viscoelastic properties of sodium hyaluronate solutions**. *Biopolymers* 1999, **50**(1):23-34.
27. Krause WE, Bellomo EG, Colby RH: **Rheology of Sodium Hyaluronate under Physiological Conditions**. *Biomacromolecules* 2001, **2**(1):65-69.
28. Cowman MK, Matsuoka S: **Experimental approaches to hyaluronan structure**. *Carbohydrate Research* 2005, **340**(5):791-809.
29. Dobrynin AV, Colby RH, Rubinstein M: **Scaling Theory of Polyelectrolyte Solutions**. *Macromolecules* 1995, **28**(6):1859-1871.
30. Doi M, Edwards SF: **The Theory of Polymer Dynamics**. Oxford: Oxford University Press; 1986.
31. Bansil R, Yannas IV, Stanley HE: **Raman Spectroscopy: A Structural Review of Glycosaminoglycans**. *Biochimica et Biophysica Acta* 1978, **541**:535-542.
32. Barrett TW, Harrington RE: **Low velocity gradient flow birefringence and viscosity changes in hyaluronate solutions as a function of pH**. *Biopolymers* 1977, **16**(10):2167-2188.

33. Barrett TW, Peticolas WL: **Laser Raman Inelastic Light Scattering Investigations of Hyaluronic Acid Primary and Secondary Structure**. *Journal Of Raman Spectroscopy* 1979, **8**(1):35-38.
34. Dehring KA, Mandair GS, Roessler BJ, Morris MD: **SERS Detection of Hyaluronic Acid: A Potential Biomarker for Osteoarthritis**. In: *New Approaches in Biomedical Spectroscopy.* Edited by Kneipp K, Aroca R, Kneipp H, Wentrup-Byrne E, vol. 693. Washington D.C.: American Chemical Society; 2006: 123-138.
35. Mandair GS, Dehring KA, Roessler BJ, Morris MD: **Detection of potential osteoarthritis biomarkers using surface enhanced Raman spectroscopy in the near-infrared**. In: *Biomedical Vibrational Spectroscopy III: Advances in Research and Industry: 2006; San Jose, CA, USA*: SPIE; 2006: 60930H-60937.
36. Cael JJ, Isaac DH, Blackwell J, Koenig JL, Atkins EDT, Sheehan JK: **Polarized infrared spectra of crystalline glycosaminoglycans**. *Carbohydrate Research* 1976, **50**:169-179.
37. Quinn FR, Bettelheim FA: **Infrared dichroism of sodium hyaluronate**. *Biochimica et Biophysica Acta* 1963, **69**:544-551.
38. Ortiz C, Zhang D, Xie Y, Ribbe AE, Ben-Amotz D: **Validation of the drop coating deposition Raman method for protein analysis**. *Analytical Biochemistry* 2006, **353**(2):157-166.
39. She CY, Dinh ND, Tu AT: **Laser raman scattering of glucosamine N-acetylglucosamine, and glucuronic acid**. *Biochimica et Biophysica Acta (BBA) - General Subjects* 1974, **372**(2):345-357.
40. Longas MO, Breitweiser KO: **Sulfate Composition of Glycosaminoglycans Determined by Infrared Spectroscopy**. *Analytical Biochemistry* 1991, **192**:193-196.
41. Gilli R, Kacurakova M, Mathlouthi M, Navarini L, Paoletti S: **FTIR studies of sodium hyaluronate and its oligomers in the amorphous solid phase and in aqueous solution**. *Carbohydrate Research* 1994, **263**(2):315-326.

Chapter 10

Conclusions

Osteoarthritis is a musculoskeletal disease that affects joints, leading to pain and loss of joint function. The asymptomatic nature of osteoarthritis is an obstacle to diagnosis, and the lack of an early-stage diagnostic tool prevents treatment. Current diagnostics rely on morphological changes to the joint, but these changes are typically found only when the disease is in the later stages. Joint health inherently relies upon a proper molecular composition of articular joint tissues and synovial fluid. The molecular composition determines not only the joint's chemical environment, but also influences biological function and viscoelasticity. Morphological changes are apparent in standard osteoarthritis tests. Chemical, biological and mechanical properties of joints may be altered before morphological changes occur, allowing a window for earlier diagnosis of disease.

Through a more complete understanding of the molecular composition of joint tissue, molecular targets for early diagnostics and treatment monitoring can be developed. In this dissertation we have examined the molecular properties of both healthy and diseased joints. In early-stage osteoarthritis, cartilage extracellular matrix molecules degenerate. Degeneration of extracellular matrix occurs either through depolymerization or alterations in hydrogen bonding that maintain secondary structure integrity. Components of extracellular matrix subject to degeneration include: type II collagen, aggregan, hyaluronic acid and chondroitin sulfate. Other changes in early-stage osteoarthritis include reduced mineral content in subchondral bone, increased synovial fluid volume, and a release of inflammatory cytokines from the synovium. These subtle chemical changes have been examined using a variety of chromatographic, histopathologic and mass spectrometric techniques. Such subtle chemical changes cannot be detected with standard clinical imaging techniques. An alternative technique for measuring the subtle chemical changes in joint tissues is through vibrational spectroscopy.

Raman spectroscopy of cartilage, subchondral bone and synovial fluid was the focus of the research presented in this dissertation. Direct examination of joint tissues using Raman spectroscopy was presented in Chapters 3 and 5. Chemical structure is measured through Raman spectroscopy, and was used in conjunction with micro-computed tomography and histopathology. The Raman measurements indicated that bone mineralization was altered in a mouse model of early-onset osteoarthritis. Such alterations in subchondral bone are not feasible for clinical measurements because all other methods for measuring bone chemistry involve destructive testing. Vibrational spectroscopic methods are minimally invasive, and are appropriate for use in clinical contexts. To demonstrate the feasibility of measuring the molecular properties of joint tissue with clinically-relevant tools, a fiber-optic Raman probe for arthroscopic measurements was developed. With further work, this method may provide molecular contrast between normal and healthy cartilage for improving the outcome of surgical interventions.

In addition to the cartilage and subchondral bone, the composition of synovial fluid is a key factor in maintaining healthy joint function. The composition of synovial fluid from normal and diseased joints was examined in Chapters 6-9. A novel method called drop deposition/Raman spectroscopy was developed to measure the Raman spectra of synovial fluid. Using the principles of drop deposition allowed optimization of the synovial fluid and plasma deposition patterns. After drops were allowed to form dried deposits, the enriched deposits were examined using Raman microscopy. Drop deposition/Raman spectroscopy was used to examine synovial fluid from human patients exhibiting clinical signs of osteoarthritis. Synovial fluid is commonly drawn from patients with osteoarthritis during lavage procedures, and so this provided an opportunity to investigate the relationship between molecular composition and joint disease. We found that Raman spectroscopic markers of protein secondary structure were correlated with radiographic evidence of osteoarthritis. We also found that hyaluronic acid content plays an important role in the drop deposition process. Hyaluronic acid is also a potential osteoarthritis biomarker, and was examined using drop deposition coupled to surface-enhanced Raman spectroscopy. Because of the common clinical practice of extracting synovial fluid and the utility for drop deposition/Raman spectroscopy analysis of synovial fluid composition, this method has potential as a screening tool for osteoarthritis. In particular, the drop deposition/Raman spectroscopy method would be amenable for high-throughput screening.

Methods were developed in this dissertation for evaluating joint damage and disease. These methods provide a foundation for the analysis of joint tissue with Raman spectroscopy. The studies presented in this thesis examined known populations and we expect to apply the technologies developed toward examination of unknown or blinded populations. Improvements to instrumentation, data processing and standards should enable clinical applications of arthroscopic joint measurements. This might include the development of compact fiber-optic probes for better control over optical sampling volumes to optimize measurement of cartilage. Furthermore, current standards for in vitro modeling of cartilage are composed of mixtures of collagen and proteoglycan. These are not ideal models because interactions are not accounted for. Because current data processing and interpretation is based on these imperfect models, quantification of proteoglycan content and interpretation of the amide I envelope are also imperfect. To better understand the interactions between macromolecular cartilage components, healthy cartilage is the ideal model. Furthermore, spectral contributions from noncollageneous proteins and matrix vesicles can only be discovered through direct measurements of cartilage.

One difficulty in using cartilage for studies of joint composition is that chondrocytes rapidly lose their phenotype in culturing conditions, so it is currently impossible to use cartilage for intervals longer than 4 weeks. The extracellular matrix is critical to maintaining chondrocytes phenotype, but interactions between chondrocytes and the extracellular matrix are not yet adequately understood. Drop deposition of prepared extracellular matrix may be useful for such investigations.

In summary, the techniques demonstrated in this dissertation have the potential to provide quantitative information about joint health, with particular emphasis on early-stage osteoarthritis detection. Results show promise toward minimally invasive measurements in joint tissue and extracted synovial fluid. Drop-deposition for preparing Raman samples pre-dates this research. However, the research presented here allows a more detailed understanding of how complex fluid properties and fluid-substrate interactions influence the final deposit, with a particular emphasis on commercially available substrates suitable for Raman spectroscopy. Through this enhanced understanding, optimization of drop deposition methodology for biofluid preparation has been simplified. Potential further applications of this research span from basic science research in understanding joint chemistry, to the development of new treatments through detailed molecular feedback, as a clinical early-stage screening tool, and for enhancing contrast in image-guided therapy for treating osteoarthritis.

Appendix

List of Publications

1. Esmonde-White KA, Mandair GS, Esmonde-White FWL, Raaii F, Roessler BJ, Morris MD, "Osteoarthritis Screening using Raman Spectroscopy of Dried Human Synovial Fluid Drops", In: *Optics in Bone Biology and Diagnostics*: *2009; San Jose, CA, USA:* SPIE; 2009, in press

2. Esmonde-White FWL, Schulmerich MV, Esmonde-White KA, Morris MD, "Automated Raman spectral preprocessing of bone and other musculoskeletal tissues", In: *Optics in Bone Biology and Diagnostics*: *2009; San Jose, CA, USA:* SPIE; 2009, in press

3. Esmonde-White KA, Mandair GS, Raaii F, Jacobson JA, Miller BS, Urquhart AG, Roessler BJ, Morris MD, "Raman Spectroscopy of Synovial Fluid as a Tool for Diagnosing Osteoarthritis", 2009, J. Biomed. Opt., 14(3), 034013 (Chapter 7)

4. Morris MD, Esmonde-White KA, Raghavan, M."Raman Scattering: Speciation and Analysis", in "Encyclopedia of Raman Spectroscopy", Andrews (ed.), 2008, in press

5. Morris MD, Schulmerich MV, Dooley KA, Esmonde-White KA, "Vibrational Spectroscopic Imaging of Hard Tissue", in "Infrared and Raman Spectroscopic Imaging", Salzer, Siesler (Eds.), 2008, in press

6. Esmonde-White KA, Le Clair SV, Roessler BJ, Morris MD, "Effect of Conformation and Drop Properties on Surface-Enhanced Raman Spectroscopy of Dried Biopolymer Drops". *Appl Spectrosc* 2008, 62(5):503-511. (Chapter 9)

7. Esmonde-White KA, Mandair GS, Raaii F, Roessler BJ, Morris MD, "Raman spectroscopy of dried synovial fluid droplets as a rapid diagnostic for knee joint damage". In: *Biomedical Optical Spectroscopy: 2008; San Jose, CA, USA*: SPIE; 2008: 68530Y.

8. Karen A. Dehring, Blake J. Roessler, Michael D. Morris, "Correlating Chemical Changes in Subchondral Bone Mineral due to Aging or Defective Type II Collagen by Raman Spectroscopy", in *Advanced Biomedical and Clinical Diagnostic Systems V*: 2007; San Jose, CA, USA: SPIE; 2007, 64301B

9. Karen A. Dehring, Gurjit S. Mandair, Blake J. Roessler, Michael D. Morris, “SERS Detection of Hyaluronic Acid: A Potential Biomarker for Osteoarthritis” in “New Approaches in Biomedical Spectroscopy”, ACS Symposium Book, 2006 (Chapter 8)

10. Karen A. Dehring, Nicole J. Crane, Abigail R. Smukler et al. “Identifying Chemical Changes to Subchondral Bone taken from Murine Knee Joints using Raman Spectroscopy”, Appl. Spectrosc., 2006, 60(10), 1134-1141 (Chapter 3)

11. Gurjit S. Mandair, Karen A. Dehring, Blake J. Roessler, Michael D. Morris, “Detection of Potential Osteoarthritis Biomarkers using Surface-Enhanced Raman Spectroscopy in the Near-Infrared”, in “Biomedical Vibrational Spectroscopy III: Advances in Research and Industry”, Proc SPIE 6093, 2006, 60930H-7

12. Karen A. Dehring, Abigail R. Smukler, Blake J. Roessler, Michael D. Morris, “Correlating Changes in Collagen Secondary Structure with Ageing and Defective Type II Collagen by Raman Spectroscopy”, Appl.Spectrosc., 2006, 60(4), 366-372 (Chapter 4)